1
Fundamentals

1.1
Superconductivity

1.1.1
Basic Properties and Parameters of Superconductors[1)]
Reinhold Kleiner

1.1.1.1 Superconducting Transition and Loss of DC Resistance

In the year 1908, Kamerlingh-Onnes [3], director of the Low-Temperature Laboratory at the University of Leiden, had achieved the liquefaction of helium as the last of the noble gases. At atmospheric pressure, the boiling point of helium is 4.2 K. It can be reduced further by pumping. The liquefaction of helium extended the available temperature range near the absolute zero point and Kamerlingh-Onnes was able to perform experiments at these low temperatures.

At first, he started an investigation of the electric resistance of metals. At that time, the ideas about the mechanism of the electric conduction were only poorly developed. It was known that it must be electrons being responsible for charge transport. Also one had measured the temperature dependence of the electric resistance of many metals, and it had been found that near room temperature the resistance decreases linearly with decreasing temperature. However, at low temperatures, this decrease was found to become weaker and weaker. In principle, there were three possibilities to be discussed:

1) The resistance could approach zero value with decreasing temperature (James Dewar, 1904).
2) It could approach a finite limiting value (Heinrich Friedrich Ludwig Matthiesen, 1864).
3) It could pass through a minimum and approach infinity at very low temperatures (William Lord Kelvin, 1902).

In particular, the third possibility was favored by the idea that at sufficiently low temperatures the electrons are likely to be bound to their respective atoms. Hence, their free mobility was expected to vanish. The first possibility, according to which

1) Text and figures of this chapter are a short excerpt from monographs [1, 2].

Applied Superconductivity: Handbook on Devices and Applications, First Edition.
Edited by Paul Seidel.

the resistance would approach zero value at very low temperatures, was suggested by the strong decrease with decreasing temperature. Initially, Kamerlingh-Onnes studied platinum and gold samples, since at that time he could obtain these metals already with high purity. He found that during the approach of zero temperature the electric resistance of his samples reached a finite limiting value, the so-called residual resistance, a behavior corresponding to the second possibility discussed above. The value of this residual resistance depended upon the purity of the samples. The purer the samples, the smaller the residual resistance. After these results, Kamerlingh-Onnes expected that in the temperature range of liquid helium, ideally, pure platinum or gold should have a vanishingly small resistance. In a lecture at the Third International Congress of Refrigeration 1913 in Chicago, he reported on these experiments and arguments. There he said: "*Allowing a correction for the additive resistance I came to the conclusion that probably the resistance of absolutely pure platinum would have vanished at the boiling point of helium*" [4]. These ideas were supported further by the quantum physics rapidly developing at that time. Albert Einstein had proposed a model of crystals, according to which the vibrational energy of the crystal atoms should decrease exponentially at very low temperatures. Since the resistance of highly pure samples, according to the view of Kamerlingh-Onnes (which turned out to be perfectly correct, as we know today), is only due to this motion of the atoms, his hypothesis mentioned above appeared obvious.

In order to test these ideas, Kamerlingh-Onnes decided to study mercury, the only metal for which he hoped at that time that it can be extremely purified by means of a multiple distillation process. He estimated that at the boiling point of helium he could barely just detect the resistance of the mercury with his equipment, and that at still lower temperatures it should rapidly approach zero value. The initial experiments carried out by Kamerlingh-Onnes together with his coworkers, Gerrit Flim, Gilles Holst, and Gerrit Dorsman, appeared to confirm these concepts. At temperatures below 4.2 K, the resistance of mercury, indeed, became immeasurably small. During his further experiments, he soon recognized that the observed effect could not be identical to the expected decrease of resistance. The resistance change took place within a temperature interval of only a few hundredths of a degree and, hence, it resembled more a resistance jump than a continuous decrease.

Figure 1.1.1.1 shows the curve published by Kamerlingh-Onnes [5]. He commented himself: "*At this point* (slightly below 4.2 K) *within some hundredths of a degree came a sudden fall not foreseen by the vibrator theory of resistance, that had framed, bringing the resistance at once less than a millionth of its original value at the melting point. … Mercury had passed into a new state, which on account of its extraordinary electrical properties may be called the* superconductive state" [4].

In this way also the name for this new phenomenon had been found. The discovery came unexpectedly during experiments, which were meant to test some well-founded ideas. Soon it became clear that the purity of the samples was unimportant for the vanishing of the resistance. The carefully performed experiment had uncovered a new state of matter.

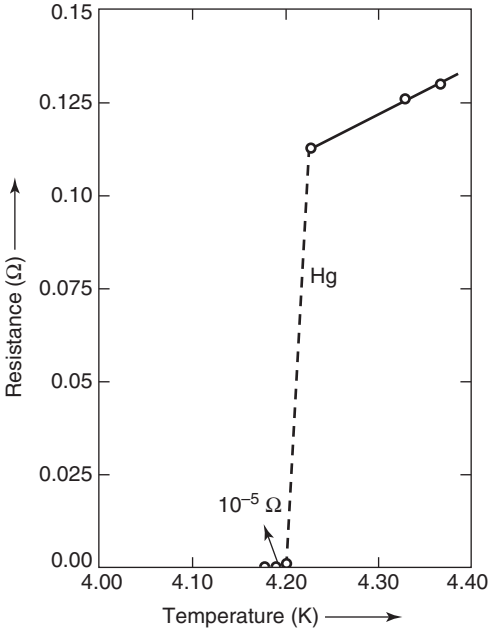

Figure 1.1.1.1 Superconductivity of mercury. (From [1], after Ref. [5].)

Today we know that superconductivity represents a widespread phenomenon. In the periodic system of the elements superconductivity occurs in many elements. Here, at atmospheric pressure, niobium is the element with the highest "transition temperature" or "critical temperature" T_c of about 9 K. Eventually, thousands of superconducting compounds have been found, and this development is by no means closed.

The vanishing of the DC electric resistance below T_c is not the only unusual property of superconductors. An externally applied magnetic field can be expelled from the interior of superconductors except for a thin outer layer ("ideal diamagnetism" or "Meissner–Ochsenfeld effect"). This happens for type-I superconductors for field below the so-called critical field B_c, and for type-II superconductors below the lower critical field B_{c1}. For higher fields, type-II superconductors can concentrate the magnetic field in the form of "flux tubes." Here the magnetic flux[2)] is quantized in units of the "magnetic flux quantum" $\Phi_0 = 2.07 \cdot 10^{-15}$ Wb. The ideal diamagnetism of superconductors was discovered by Meissner and Ochsenfeld in 1933. It was a big surprise, since based on the induction law one would

2) The magnetic flux Φ through a loop of area F, carrying a perpendicular and spatially homogeneous flux density B is given by $\Phi = B \cdot F$. In the following, we denote B simply by "magnetic field." In the general case of an arbitrarily oriented and spatially inhomogeneous magnetic field $\boldsymbol{B}$, one must integrate over the area of the loop, $\Phi = \int_F \boldsymbol{B}\, d\boldsymbol{f}$. The unit of magnetic flux is weber (Wb), the unit of the magnetic field is tesla (T). We have 1 Wb = 1 T m^2. If a loop is placed at a large distance around the axis of an isolated flux tube, we have $\Phi = \Phi_0$.

have only expected that an ideal conductor conserves its interior magnetic field and does not expel it.

The breakthrough of the theoretical understanding of superconductivity was achieved in 1957 by the theory of Bardeen, Cooper, and Schrieffer ("BCS theory") [6]. They recognized that at the transition to the superconducting state, the electrons pairwise condense into a new state, in which they form a coherent matter wave with a well-defined phase, following the rules of quantum mechanics. Here the interaction of the electrons is mediated by the "phonons," the quantized vibrations of the crystal lattice. The pairs are called *Cooper pairs*. In most cases, the spins of the two electrons are aligned antiparallelly, that is, they form spin-singlets. Also, at least in most cases, the angular momentum of the pair is zero (s-wave). The theory also shows that at nonzero temperatures, a part of the electrons remain unpaired. There is, however, an energy gap Δ which separates these unpaired "quasiparticles" from the Cooper pairs. It requires the energy 2Δ to break a pair.

For more than 75 years, superconductivity represented specifically a low-temperature phenomenon. This changed in 1986, when Bednorz and Müller [7] discovered superconductors based on copper oxide.

This result was highly surprising for the scientific community, also because already in the middle 1960s, Matthias and coworkers had started a systematic study of the metallic oxides. They searched among the substances based on the transition metal oxides, such as W, Ti, Mo, and Bi [8]. They found extremely interesting superconductors, for example, in the Ba – Pb – Bi – O system, however, no particularly high transition temperatures.

During the turn of the year 1986 – 1987, the "gold rush" set in, when it became known that the group of Shigeho Tanaka in Japan could exactly reproduce the results of Bednorz and Müller. Only a few weeks later, transition temperatures above 80 K were observed in the Y – Ba – Cu – O system [9]. During this phase, new results more often were reported in press conferences than in scientific journals. The media anxiously followed this development. With superconductivity at temperatures above the boiling point of liquid nitrogen ($T = 77$ K), one could envision many important technical applications of this phenomenon.

Today we know a large series of cuprate "high-temperature superconductors." Here the mostly studied compounds are $YBa_2Cu_3O_7$ (also "YBCO" or "Y123") and $Bi_2Sr_2CaCu_2O_8$ (also "BSCCO" or "Bi2212"), which display maximum transition temperatures around 90 K. Some compounds have transition temperatures even above 100 K. The record value is carried by $HgBa_2Ca_2Cu_3O_8$, having at atmospheric pressure a T_c value of 135 K and at a pressure of 30 GPa, a value as high as $T_c = 164$ K. Figure 1.1.1.2 shows the evolution of the transition temperatures since the discovery by Kamerlingh-Onnes. The jump-like increase due to the discovery of the copper-oxides is particularly impressive.

In Figure 1.1.1.2, we have also included the metallic compound MgB_2, as well as the iron pnictides.

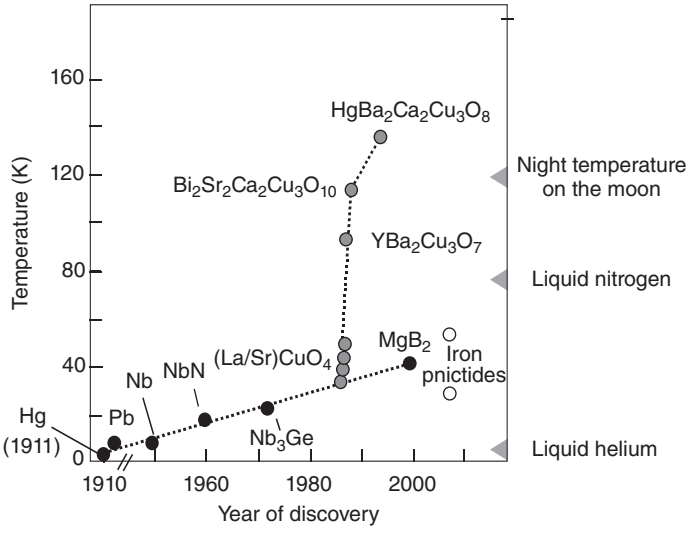

Figure 1.1.1.2 Evolution of the superconducting transition temperature since the discovery of superconductivity. (From [2], after Ref. [10].)

For MgB_2, surprisingly, superconductivity with a transition temperature of 39 K was detected only in 2000, even though this material has been commercially available for a long time [11]. Also, this discovery had a great impact in physics, and many essential properties of this material have been clarified in the subsequent years. It turned out that MgB_2 behaves similarly as the "classical" metallic superconductors, however with two energy gaps. The discovery of the iron pnictides in 2008 [12] had a similar impact. These are compounds like $LaFeAsO_{0.89}F_{0.11}$ or $Ba_{0.6}KFe_2As_2$, with transition temperatures of up to 55 K. The iron pnictides contain layers made of FeAs as the basic building block, in analogy to the copper oxide layers in the cuprates.

Many properties of the high-temperature superconductors (in addition also to other superconducting compounds) are highly unusual. For example, the Cooper pairs in the cuprates have an angular momentum of $2\hbar$ (d-wave) and the coherent matter wave has $d_{x^2-y^2}$ symmetry. For the d-wave symmetry, the energy gap Δ disappears for some directions in momentum space. More than 25 years after their discovery, it is still unclear how the Cooper pairing is accomplished in these materials. However, it seems likely that magnetic interactions play an important role.

Another important issue is the maximum current which a superconducting wire or tape can carry without resistance, the so-called critical current. We will see that the property "zero resistance" is not always fulfilled. When alternating currents are applied, the resistance can become finite. Also for DC currents, the critical current is limited. It depends on the temperature and the magnetic field, and also on the type of superconductor used and the geometry of the wire. It is a big challenge to fabricate conductors in a way that hundreds or even thousands of amperes can be carried without or at least with very low resistance.

1.1.1.2 Ideal Diamagnetism, Flux Quantization, and Critical Fields

It has been known for a long time that the characteristic property of the superconducting state is that it shows no measurable resistance for direct current. If a magnetic field is applied to such an *ideal conductor*, permanent currents are generated by induction, which screen the magnetic field from the interior of the sample. For that reason, a permanent magnet can levitate when placed on top of an ideal conductor. This effect is demonstrated in Figure 1.1.1.3.

What happens if a magnetic field $\boldsymbol{B}_a$ is applied to a *normal conductor* and if subsequently by cooling below the transition temperature T_c ideal conductivity is reached? At first, in the normal state at the application of the magnetic field, eddy currents are flowing because of induction. However, as soon as the magnetic field has reached its final value and does not change anymore with time, these currents decay, and finally the magnetic fields within and outside the superconductor become equal. If now the ideal conductor is cooled below T_c, this magnetic state simply remains, since further induction currents are generated only during *changes* of the field. Exactly this is expected, if the magnetic field is turned off below T_c. In the interior of the ideal conductor, the magnetic field remains conserved. Hence, depending upon the way in which the final state, namely a temperature below T_c and an applied magnetic field $\boldsymbol{B}_a$, has been reached, within the interior of the ideal conductor we have completely different magnetic fields.

Accordingly, a material with the only property $R = 0$, for the same external variables T and $\boldsymbol{B}_a$, could be transferred into completely different states, depending upon the previous history. Therefore, for the same given thermodynamic variables, we would not have just one well-defined superconducting phase, but, instead, a continuous manifold of superconducting phases with arbitrary shielding currents, depending upon the previous history. However, the existence of a manifold of superconducting phases appeared so unlikely, that also before 1933 one referred to only a single superconducting phase even without an experimental verification.

As a matter of fact, a superconductor behaves quite different than an ideal electric conductor. Again we imagine that a sample is cooled below T_c in the presence of an applied magnetic field. If this magnetic field is very small, one finds that

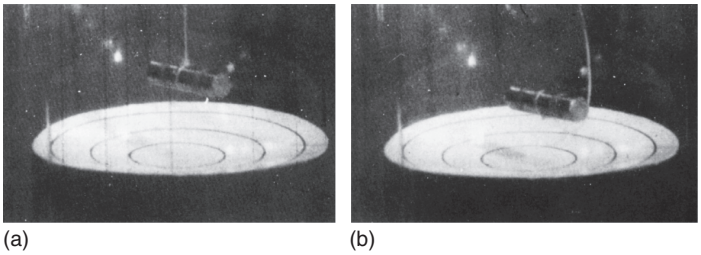

(a) (b)

Figure 1.1.1.3 The "levitated magnet" for demonstrating the permanent currents, which are generated in superconducting lead by induction during the lowering of the magnet. (a) Starting position and (b) equilibrium position.

the field is completely expelled from the interior of the superconductor except for a very thin layer at the sample surface. In this way, one obtains an ideal diamagnetic state, independent of the temporal sequence in which the magnetic field was applied and the sample was cooled.

This ideal diamagnetism has been discovered in 1933 by Meissner and Ochsenfeld [13] for rods made of lead or tin. This expulsion effect, similar as the property $R = 0$, can be nicely demonstrated using the "levitated magnet." In order to show the property $R = 0$, in Figure 1.1.1.3 we have lowered the permanent magnet toward the superconducting lead bowl, generating in this way by induction the permanent currents. For demonstrating the Meissner–Ochsenfeld effect, we place the permanent magnet into the lead bowl at $T > T_c$ (Figure 1.1.1.4a) and then cool further down. The field expulsion appears at the superconducting transition, the magnet is repelled from the diamagnetic superconductor, and it is raised up to the equilibrium height (Figure 1.1.1.4b). In the limit of ideal magnetic field expulsion, the same levitation height is reached as in Figure 1.1.1.3.

Above, we had assumed that the magnetic field applied to the superconductor would be "small." Indeed, one finds that the ideal diamagnetism only exists within a finite range of magnetic fields and temperatures, which, furthermore, also depends upon the sample geometry.

Next we consider a long, rod-shaped sample where the magnetic field is applied parallel to the axis. For other shapes, the magnetic field often can be distorted. One finds that there exist two different types of superconductors:

- The first type, referred to as *type-I superconductors* or *superconductors of the first kind*, expels the magnetic field up to a maximum value B_c, the critical field. For larger fields, superconductivity breaks down, and the sample assumes the normal-conducting state. B_c depends on the temperature and reaches zero at T_c. Pure mercury or lead are examples of a type-I superconductor.
- The second type, referred to as *type-II superconductors* or *superconductors of the second kind*, shows ideal diamagnetism for magnetic fields smaller than the

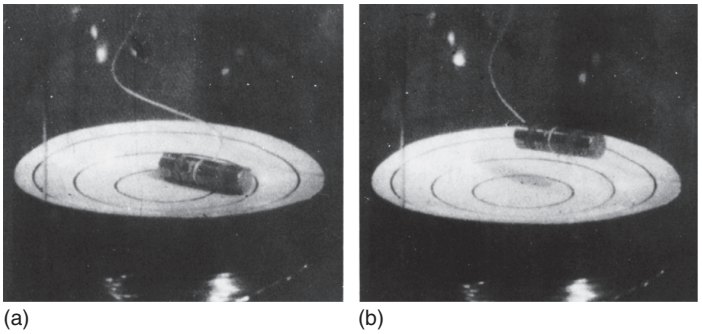

(a) (b)

Figure 1.1.1.4 "Levitated magnet" for demonstrating the Meissner–Ochsenfeld effect in the presence of an applied magnetic field. (a) Starting position at $T > T_c$ and (b) equilibrium position at $T < T_c$.

"lower critical magnetic field" B_{c1}. Superconductivity completely vanishes for magnetic fields larger than the "upper critical magnetic field" B_{c2}, which often is much larger than B_{c1}. Both critical fields reach zero at T_c. This behavior is found in many alloys, but also in the high-temperature superconductors. In the latter, B_{c2} can reach even values larger than 100 T, depending on the direction the field is applied relative to the CuO layers.

What happens in type-II superconductors in the "Shubnikov phase" between B_{c1} and B_{c2}? In this regime, the magnetic field only partly penetrates into the sample. Now shielding currents flow within the superconductor and concentrate the magnetic field lines, such that a system of flux lines, also referred to as *Abrikosov vortices*, is generated. In an ideal homogeneous superconductor, in general, these vortices arrange themselves in form of a triangular lattice. In Figure 1.1.1.5, we show schematically this structure of the Shubnikov phase. The superconductor is penetrated by magnetic flux lines, each of which carries a magnetic flux quantum and is located at the corners of equilateral triangles. Each flux line consists of a system of circular currents, which in Figure 1.1.1.5 are indicated for two flux lines. These currents together with the external magnetic field generate the magnetic flux within the flux line and reduce the magnetic field between the flux lines. Hence, one also talks about flux vortices. With increasing external field $\boldsymbol{B}_a$, the distance between the flux lines becomes smaller.

The first experimental proof of a periodic structure of the magnetic field in the Shubnikov phase was given in 1964 by a group at the Nuclear Research Center in Saclay using neutron diffraction [14]. However, they could only observe a basic period of the structure. Real images of the Shubnikov phase were generated by Essmann and Träuble [15] using an ingenious decoration technique. In

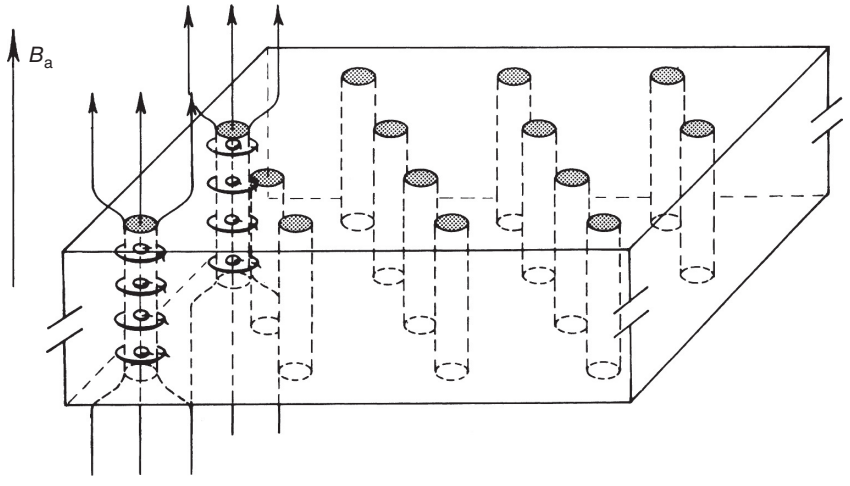

Figure 1.1.1.5 Schematics of the Shubnikov phase. The magnetic field and the supercurrents are shown only for two flux lines.

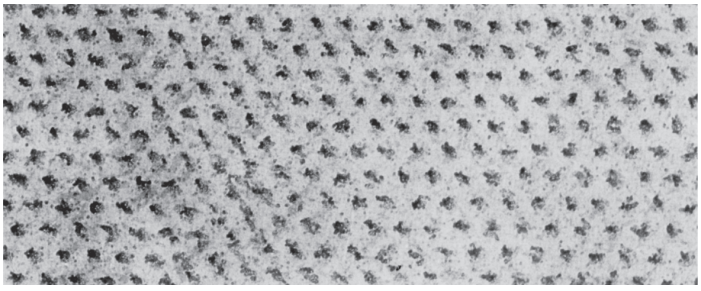

Figure 1.1.1.6 Image of the vortex lattice obtained with an electron microscope following the decoration with iron colloid. Frozen-in flux after the magnetic field has been reduced to zero. Material: Pb + 6.3 at.% In; temperature: 1.2 K; sample shape: cylinder 60 mm long, 4 mm diameter; magnetic field B_a parallel to the axis. Magnification: 8300× (Reproduced by courtesy of Dr. Essmann.)

Figure 1.1.1.6, we show a lead–indium alloy as an example. These images of the magnetic flux structure were obtained as follows: above the superconducting sample iron atoms are evaporated from a hot wire. During their diffusion through the helium gas in the cryostat, the iron atoms coagulate forming iron colloids. These colloids have a diameter of <50 nm, and they slowly approach the surface of the superconductor. At this surface, the flux lines of the Shubnikov phase exit from the superconductor. In Figure 1.1.1.6, this is shown for two flux lines. The ferromagnetic iron colloid is collected at the locations, where the flux lines exit from the surface, since here they find the largest magnetic-field gradients. In this way, the flux lines can be decorated. Subsequently, the structure can be observed in an electron microscope. The image shown in Figure 1.1.1.6 was obtained in this way. Such experiments convincingly confirmed the vortex structure predicted theoretically by Abrikosov.

The question remains if the decorated locations at the surface indeed correspond to the ends of the flux lines carrying only a single flux quantum. In order to answer this question, we just have to count the number of flux lines and also have to determine the total flux, say, by means of an induction experiment. Then we find the value of the magnetic flux of a flux line by dividing the total flux Φ_{tot} through the sample by the number of flux lines. Such evaluations exactly confirmed that in highly homogeneous type-II superconductors each flux line contains a single flux quantum $\Phi_0 = 2.07 \cdot 10^{-15}$ T m^2.

Today, apart from neutron diffraction and decoration, there are a number of different methods for imaging magnetic flux lines. We will not go into detail but mention that the methods often supplement each other and provide valuable information about superconductivity.

Flux quantization, in integer multiples of Φ_0, also occurs in a superconducting ring. This has been demonstrated very nicely in pioneering experiments by Doll and Näbauer [16] in Munich and by Deaver and Fairbank [17] in Stanford.

1.1.1.3 The Origin of Flux Quantization, London Penetration Depth and Ginzburg–Landau Coherence Length

Next we will deal with the conclusions to be drawn from the quantization of the magnetic flux in units of the flux quantum Φ_0.

For atoms we are well used to the appearance of discrete states. For example, the stationary atomic states are distinguished due to a quantum condition for the angular momentum appearing in multiples of $\hbar = h/2\pi$. This quantization of the angular momentum is a result of the condition that the quantum mechanical wave function, indicating the probability for finding the electron, be single-valued. If we move around the atomic nucleus starting from a specific point, the wave function must reproduce itself exactly if we return to this starting point. Here, the phase of the wave function can change by an integer multiple of 2π, since this does not affect the wave function. We can have the same situation also on a macroscopic scale. Imagine that we have an arbitrary wave propagating without damping in a ring with radius R. The wave can become stationary, if an integer number n of wavelengths λ exactly fits into the ring. Then we have the condition $n\lambda = 2\pi R$ or $kR = n$, using the wave vector $k = 2\pi/\lambda$. If this condition is violated, after a few revolutions the wave disappears due to interference.

Applying these ideas to the Cooper pair matter wave propagating around the ring[3] one obtains [1, 2]:

$$n \cdot \frac{h}{q} = \mu_0 \lambda_L^2 \oint \boldsymbol{j}_s d\boldsymbol{r} + \Phi \tag{1.1.1.1}$$

Equation (1.1.1.1) represents the so-called fluxoid quantization. The integral has to be taken along some closed contour inside the superconductor and Φ is magnetic flux penetrating this contour. The expression on the right-hand side denotes the "fluxoid." The quantity

$$\lambda_L = \sqrt{\frac{m}{\mu_0 q^2 n_s}} \tag{1.1.1.2}$$

is the London penetration depth (q: charge; m: particle mass; n_s: particle density; μ_0: permeability) and $\boldsymbol{j}_s$ is the super-current density.

In many cases, the super-current density and, hence, the path integral on the right-hand side of Eq. (1.1.1.1) is negligibly small. This happens in particular if we deal with a thick-walled superconducting cylinder or with a ring made of a type-I superconductor. Because of the Meissner–Ochsenfeld effect, the magnetic field is expelled from the superconductor. The shielding super-currents only flow near the surface of the superconductor and decay exponentially toward the interior, as we will discuss further below. We can place the integration path, along which Eq. (1.1.1.1) must be evaluated, deep into the interior of the ring. In this case, the integral over the current density is exponentially small, and we obtain in good

3) The moving wave is connected with the motion of the center of mass of the pairs, which is identical for all pairs.

approximation

$$\Phi \approx n \cdot \frac{h}{q} \tag{1.1.1.3}$$

This is exactly the condition for the quantization of the magnetic flux, and the experimental observation $\Phi = n \cdot (h/2|e|) = n \cdot \Phi_0$ clearly shows that the superconducting charge carriers have the charge $|q| = 2e$. The sign of the charge carriers cannot be found from the observation of the flux quantization, since the direction of the *particle* current is not determined in this experiment. In many superconductors, the Cooper pairs are formed by electrons, that is, $q = -2e$. On the other hand, in many high-temperature superconductors, we have hole conduction, similar to that found in p-doped semiconductors. Here we have $q = +2e$.

From Eq. (1.1.1.1), one can also show [1, 2] that for a solid material which is superconducting everywhere in its interior only $n = 0$ is possible. Then one arrives at

$$\mu_0 \lambda_L^2 \oint \boldsymbol{j}_s d\boldsymbol{r} = -\Phi = -\int_F \boldsymbol{B} d\boldsymbol{f} \tag{1.1.1.4}$$

Using Stokes's theorem, this condition can also be written as

$$\boldsymbol{B} = -\mu_0 \lambda_L^2 \operatorname{curl} \boldsymbol{j}_s \tag{1.1.1.5}$$

Equation (1.1.1.5) is the second London equation. It is one of two fundamental equations with which the two brothers F. London and H. London in 1935 [18] constructed a successful theoretical model of superconductivity. From Eq. (1.1.1.5), after some math one finds

$$\Delta \boldsymbol{B} = \frac{1}{\lambda_L^2} \boldsymbol{B} \tag{1.1.1.6}$$

Δ is the Laplace operator, $\Delta f = (\partial^2 f/\partial x^2) + (\partial^2 f/\partial y^2) + (\partial^2 f/\partial z^2)$, which in Eq. (1.1.1.6) must be applied to the three components of $\boldsymbol{B}$.

Equation (1.1.1.6) produces the Meissner – Ochsenfeld effect, as we can see from a simple example. For this purpose, we consider the surface of a very large superconductor, located at the coordinate $x = 0$ and extended infinitely along the (x,y)-plane. The superconductor occupies the half-space $x > 0$ (see Figure 1.1.1.7). An external magnetic field $\boldsymbol{B}_a = (0, 0, B_a)$ is applied to the superconductor. Owing to the symmetry of our problem, we can assume that within the superconductor only the z-component of the magnetic field is different from zero and is only a function of the x-coordinate. Equation (1.1.1.6) then yields for $B_z(x)$ within the superconductor, that is, for $x > 0$:

$$\frac{d^2 B_z(x)}{dx^2} = \frac{1}{\lambda_L^2} B_z(x) \tag{1.1.1.7}$$

This equation has the solution

$$B_z(x) = B_z(0) \cdot \exp\left(-\frac{x}{\lambda_L}\right) \tag{1.1.1.8}$$

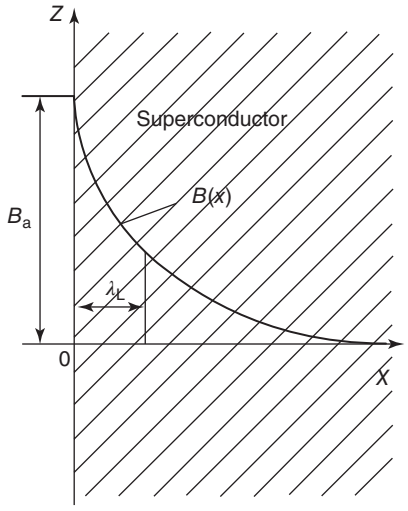

Figure 1.1.1.7 Decrease of the magnetic field within the superconductor near the planar surface.

which is shown in Figure 1.1.1.7. Within the length λ_L the magnetic field is reduced by the factor $1/e$, and the field vanishes deep inside the superconductor.

We note that Eq. (1.1.1.7) also yields a solution increasing with x: $B_z(x) = B_z(0) \cdot \exp(+x/\lambda_L)$. However, this solution leads to an arbitrarily large magnetic field in the superconductor and, hence, is not meaningful.

From Eq. (1.1.1.2), we can obtain a rough estimate of the London penetration depth with the simplifying assumption that one electron per atom with the free-electron mass m_e contributes to the super-current. For tin, for example, such an estimate yields $\lambda_L = 26$ nm. This value deviates only little from the measured value, which at low temperatures falls in the range 25 – 36 nm. More values for λ_L are listed in Table 1.1.1.1 together with a number of other parameters that will be introduced in this chapter. All numbers should be taken just as rough guidelines since they depend strongly on the sample purity. For some materials, λ_L, as well as the other quantities, depend strongly on the crystal orientation. These materials are often layered structures. The London penetration depth can be very large when the magnetic field is applied parallel to the layers.

Only a few nanometer away from its surface the superconducting half-space is practically free of the magnetic field and displays the ideal diamagnetic state. The same can be found for samples with a more realistic geometry, for example, for a superconducting rod, as long as the radii of curvature of the surfaces are much larger than λ_L and the superconductor is also much thicker than λ_L. Then on a length scale of λ_L, the superconductor closely resembles a superconducting half-space. Of course, for an exact solution Eq. (1.1.1.6) must be solved.

The London penetration depth depends upon temperature. From Eq. (1.1.1.2) we see that λ_L is proportional to $1/n_s^{1/2}$. We can assume that the number of electrons combined to Cooper pairs decreases with increasing temperature and

Table 1.1.1.1 Critical temperature and zero temperature values of the energy gap, the coherence length, and the upper critical field. Numbers vary strongly in the literature and thus should be taken as a rough guide only. For Pb and Nb, the critical field rather than B_{c2} is quoted. (*ab*) and (*c*), respectively refer to in-plane and out-of-plane properties; "*max*." indicates the maximum energy gap.

Material	T_c (K)	Δ (meV)	ξ_{GL} (nm)	λ_L (nm)	B_c, B_{c2} (T)
Pb	7.2	1.38	51–83	32–39	0.08 (B_c)
Nb	9.2	1.45	40	32–44	0.2 (B_c)
NbN	13–16	2.4–3.2	4	250	16
Nb_3Sn	18	3.3	4	80	24
Nb_3Ge	23.2	3.9–4.2	3–4	80	38
NbTi	9.6	1.1–1.4	4	60	16
$YBa_2Cu_3O_7$	92	15–25 (*max.*, *ab*)	1.6 (*ab*) 0.3 (*c*)	150 (*ab*) 800 (*c*)	240 (*ab*) 110 (*c*)
$Bi_2Sr_2CaCu_2O_8$	94	15–25 (*max.*, *ab*)	2 (*ab*) 0.1 (*c*)	200–300 (*ab*) >15 000 (*c*)	>60 (*ab*) >250 (*c*)
$Bi_2Sr_2Ca_2Cu_3O_{10}$	110	25–35 (*max.*, *ab*)	2.9 (*ab*) 0.1 (*c*)	150 (*ab*) >1000 (*c*)	40 (*ab*) >250 (*c*)
MgB_2	40	1.8–7.5	10 (*ab*) 2 (*c*)	110 (ab) 280 (*c*)	15–20 (*ab*) 3 (*c*)
$Ba_{0.6}K_{0.4}Fe_2As_3$	38	4–12	1.5 (*ab*) $c > 5$ (*c*)	190 (*ab*) 0.9 (*c*)	70–235 (*ab*) 100–140 (*c*)
$NdO_{0.82}F_{0.18}FeAs$	50	37	3.7 (*ab*) 0.9 (*c*)	190 (*ab*)*c* >6000 (*c*)	62–70 (*ab*) 300 (*c*)

vanishes at T_c. Above the transition temperature, no stable Cooper pairs should exist anymore.[4] Hence, we expect that λ_L increases with increasing temperature and diverges at T_c. Correspondingly, the magnetic field penetrates further and further into the superconductor until it homogeneously fills the sample above the transition temperature.

How can one measure the London penetration depth? In principle, one must determine the influence of the thin shielding layer upon the diamagnetic behavior. This has been done using several different methods. For example, one can measure the magnetization of plates which are thinner and thinner [19]. As long as the thickness of the plate is much larger than the penetration depth, one will observe nearly ideal diamagnetic behavior. However, this behavior becomes weaker, if the plate thickness approaches the range of λ_L. Another method uses spin-polarized muons, which, by varying their kinetic energy, are implanted in different depths from the surface. The spin of the muon precesses in the local magnetic field and, by measuring the electron that are emitted upon its decay, it is possible to determine the precession frequency and thus the local magnetic field [20]. For determining the temperature dependence of λ_L, only relative

4) Here we neglect thermal fluctuations by which Cooper pairs can be generated momentarily also above T_c.

measurements are needed. One can determine the resonance frequency of a cavity fabricated from a superconducting material. The resonance frequency sensitively depends on the geometry. If the penetration depth varies with the temperature, this is equivalent to a variation of the geometry of the cavity and, hence, of the resonance frequency, yielding the change of λ_L [21].

A strong interest in the exact measurement of the penetration depth, say, as a function of temperature, magnetic field, or the frequency of the microwaves for excitation, arises because of its dependence upon the density of the superconducting charge carriers. It yields important information on the superconducting state and can serve as a sensor for studying superconductors.

What causes the difference between type-I and type-II superconductivity and the generation of vortices? From the assumption of a continuous superconductor, we have obtained the second London equation and the ideal diamagnetism. In type-I superconductors, this state is established, as long as the applied magnetic field does not exceed a critical value. At higher fields, superconductivity breaks down. For a discussion of the critical magnetic field, we must treat the energy of a superconductor more accurately. This is done in the framework of the Ginzburg–Landau theory. Here, one can see that it is the competition between two energies, the energy gain from the condensation of the Cooper pairs and the energy loss due to the magnetic field expulsion, which causes the transition between the superconducting and the normal-conducting state.

At small magnetic fields, the Meissner phase is also established in type-II superconductors. However, at the lower critical field, vortices appear within the material. Turning again to Eq. (1.1.1.1), we see that the separation of the magnetic flux into units[5] of $\pm 1\Phi_0$ corresponds to states with the quantum number $n = \pm 1$. Here, the superconductor cannot display continuous superconductivity anymore, for which case $n = 0$ was the only possibility. Instead, we must assume that the vortex axis is not superconducting, similar to the ring geometry.

A more accurate treatment of the vortex structure based on the Ginzburg–Landau theory shows that the magnetic field decreases nearly exponentially with the distance from the vortex axis on the length scale λ_L. Hence, we can say that the flux line has a magnetic radius of λ_L.

Second, on a length scale ξ_{GL}, the Ginzburg–Landau coherence length, the density n_s of the Cooper pairs vanishes as one approaches the vortex axis. Depending on the superconducting material, this length ranges between 0.1 nm and a few hundred nanometers; see also Table 1.1.1.1. Similar to the London penetration depth, it is temperature dependent, in particular close to T_c. We also mention here that there is also a coherence length associated with the distance over which the two electrons forming the Copper pairs are correlated. This is the BCS coherence length $\xi_0 = \hbar v_F / k_B T_c$, where v_F is the Fermi velocity.

Why does each vortex carry exactly one flux quantum Φ_0? Again we must look at the energy of a superconductor. Essentially, we find that in a type-II superconductor it is energetically favorable if it generates an interface superconductor/normal

5) The sign must be chosen according to the direction of the magnetic field.

conductor above the lower critical magnetic field. Therefore, as many of these interfaces as possible are generated. This is achieved by choosing the smallest quantum state with $n = \pm 1$, since in this case the maximum number of vortices and the largest interface area near the vortex axis is established.

Now we can estimate the lower critical field B_{c1}. Each flux line carries a flux quantum Φ_0, and at least one needs a magnetic field $B_{c1} \approx \Phi_0/(\text{cross-sectional area of the flux line}) \approx \Phi_0/(\pi\lambda_L^2)$ for generating this amount of flux. With a value of $\lambda_L = 100\,\text{nm}$ one finds $B_{c1} \approx 65\,\text{mT}$. From the Ginzburg–Landau theory, one obtains an expression which differs from our simple estimate by a factor of $(\ln\kappa + 0.08)/4$, with $\kappa = \lambda_L/\xi_{GL}$. This factor is on the order of unity for not too small values of κ.

For increasing magnetic field, the flux lines are packed closer and closer to each other, until near B_{c2} their distance is about equal to the Ginzburg–Landau coherence length ξ_{GL}. For a simple estimate of B_{c2}, we assume a cylindrical normal-conducting vortex core. Then superconductivity is expected to vanish, if the distance between the flux quanta becomes equal to the core diameter, that is, at $B_{c2} \approx \Phi_0/(\pi\xi_{GL}^2)$. An exact theory yields a value smaller by a factor of 2. In fact, often one uses the corresponding relation for determining ξ_{GL}. We further note that, depending on the value of ξ_{GL}, B_{c2} can become very large. With the value $\xi_{GL} = 2\,\text{nm}$, one obtains a field larger than 80 T. Such high values of the upper critical magnetic field are reached or even exceeded in the high-temperature superconductors.

Table 1.1.1.1 lists B_{c2} for several superconductors. In the table, we have also listed the critical field of Nb and Pb. Pure single crystals of these materials are type-I superconductors. It should be noted, however, that in most practical cases, due to a reduced mean free path, the electrons can travel without scattering, the coherence length is smaller, and λ_L is larger, making these materials type-II.

At the end of this section, we wish to ask how the permanent current and zero resistance, the key phenomena of superconductivity, can be explained in terms of the macroscopic wave function. From the second London equation (1.1.1.5), with the use Maxwell's equations one obtains

$$\boldsymbol{E} = \mu_0 \lambda_L^2 \dot{\boldsymbol{j}}_s \tag{1.1.1.9}$$

This is the first London equation. For a temporally constant super-current, the right-hand side of Eq. (1.1.1.9) is zero. Hence, we obtain current flow without an electric field and zero resistance.

Note that the relation $\boldsymbol{E} \propto \dot{\boldsymbol{j}}_s$ is similar to that of an inductor, $U_L \propto \dot{I}_L$. We can thus understand one of the reasons why an alternating current will produce a finite resistance. At nonzero temperatures, a part of the electrons in the superconductor is unpaired (quasiparticles). In the presence of an alternating electric field, both quasiparticles and Cooper pairs are accelerated and a nonzero resistance appears which grows with increasing frequency.

Equation (1.1.1.9) also indicates that in the presence of a DC electric field, the super-current density continues to increase with time. For a superconductor this seems reasonable, since the superconducting charge carriers are accelerated more

and more due to the electric field. On the other hand, the super-current density cannot increase up to infinity. Therefore, additional energy arguments are needed for finding the maximum super-current density which can be reached. This can be treated in the framework of the Ginzburg–Landau theory and yields the so-called pair-breaking critical current density.

We could have derived the first London equation also from classical arguments, if we note that for current flow without resistance the superconducting charge carriers cannot experience (inelastic) collision processes. Then, in the presence of an electric field, we have the force equation $m\dot{\boldsymbol{v}} = q\boldsymbol{E}$. We use $\boldsymbol{j}_s = qn_s\boldsymbol{v}$ and find $\boldsymbol{E} = (m/q^2 n_s)\dot{\boldsymbol{j}}_s$. The latter equation can be turned into Eq. (1.1.1.9) using the definition (1.1.1.2) of the London penetration depth.

Finally, we briefly mention here that the well-defined phase of the superconducting matter wave is responsible for interference effects as they appear in Josephson junctions and in superconducting quantum interference devices (SQUIDs). It turns out that, in a Josephson junction, a sandwich consisting of two superconducting electrodes separated by a very thin barrier, there is a super-current across the barrier which varies sinusoidally with the difference δ of the phases of the matter wave of the two electrodes. If there is a voltage drop U across the barrier this phase differences increases in time, with the time derivative of δ given by $\dot{\delta} = 2\pi U/\Phi_0$. In SQUIDs two Josephson junctions are integrated in a superconducting loop. Here, the maximum super-current that can be sent across the two junctions varies sinusoidally with the magnetic flux threading the loop. The modulation period is given by the flux quantum. Details will be given in the corresponding chapters.

1.1.1.4 **Critical Currents**

We have already mentioned that a superconductor can carry only a limited electric current without resistance. The existence of a critical current is highly important for technical applications of superconductivity. In type-II superconductors, we have materials which can remain still superconducting also for technically interesting magnetic fields. However, for applications it is also important that these superconductors still can transport sufficiently high electric currents without resistance also in high magnetic fields. As we will see, here we are confronted with a problem, which has been solved only with the so-called hard superconductors.

Before we turn to the special features in type-I and type-II superconductors, we want to briefly look at the magnitude of the critical super-current density in the ideal case of a thin and homogeneous superconducting wire. This pair-breaking critical current density j_{cp}, which can be reached under most favorable conditions, can be treated within the Ginzburg–Landau theory. We consider a homogeneous superconducting wire having a diameter which is smaller than the London penetration depth λ_L and the Ginzburg–Landau coherence length ξ_{GL}. We find

$$j_{cp} = \frac{2}{3}\sqrt{\frac{2}{3}}B_{cth} \cdot \frac{1}{\mu_0 \lambda_L} \tag{1.1.1.10}$$

B_{cth} is the so-called thermodynamical critical field which for a type-I superconductor under certain conditions equals the critical field B_c. For a type-II superconductor, it can be related to the upper critical field via $B_{cth} = B_{c2}/\sqrt{2}\kappa$, with the Ginzburg–Landau parameter $\kappa = \lambda_L/\xi_{GL}$.

If for B_{cth} we take a value of 1 T and for λ_L a value of 100 nm, we obtain for j_{cp} a value of about $4.3{\cdot}10^8$ A cm^{-2}.

With respect to type-I superconductors, we consider a wire with circular cross-section carrying a current *I.* The wire is assumed much thicker than the London penetration depth. At sufficiently small currents, the superconducting wire resides in the Meissner phase. In this phase, the interior of the superconductor must remain free of magnetic flux. However, this also means that the interior cannot carry an electric current, since otherwise the magnetic field of the current would exist. From this, we conclude that also the current passing through a superconductor is restricted to the thin surface layer, into which the magnetic field can penetrate in the Meissner phase. The external currents applied to a superconductor are referred to as *transport currents*, in contrast to the shielding currents appearing in the superconductor as circulating currents. The total current is given by the integral of the current density over the cross-sectional area.

Already in 1916, Silsbee [22] proposed the hypothesis, that in the case of "thick" superconductors, that is, for superconductors with a fully developed shielding layer, the critical current is reached exactly, when the magnetic field of the current at the surface attains the value B_{cth}. This hypothesis has been confirmed perfectly. In other words, it means that the magnetic field and the current density at a surface with a well-developed shielding layer are strongly correlated. The critical value of the current density is associated with a certain critical field, namely B_{cth}, where it is completely irrelevant, if the current density is due to shielding currents or to a transport current.

Because of the validity of the Silsbee hypothesis, it is very simple to calculate the critical currents of wires with circular cross-section from the critical fields. The magnetic field at the surface of such a wire carrying the current I is given by

$$B_0 = \mu_0 \frac{I}{2\pi R} \tag{1.1.1.11}$$

where B_0 is the field at the surface, I is the transport current, R is the wire radius, and $\mu_0 = 4\pi{\cdot}10^{-7}$ V s (A m)$^{-1}$.

The only requirement is cylinder symmetry of the current distribution. The radial dependence of the current density is arbitrary. According to Eq. (1.1.1.11), the critical field of about 30 mT at 0 K – the value for the critical field of tin – corresponds to a critical current $I_{c0} = 75$ A. This critical current increases only proportionally to the wire radius, since the total current only flows within the thin shielding layer.

We can also find an average critical *current density* at the surface. In this case, we replace the exponentially decaying current density by a distribution, in which the full current density at the surface remains constant to a depth λ_L, the penetration

depth, and then abruptly drops to zero.[6] Based on this argument, for the tin wire at 0 K, we obtain a critical current density

$$j_{c0} = \frac{I_{c0}}{2\pi R \lambda_L(0)} = 7.9 \cdot 10^7 \,\mathrm{A\,cm^{-2}} \tag{1.1.1.12}$$

where $R = 0.5$ mm, $\lambda_L(0) = 3 \cdot 10^{-6}$ cm, $I_{c0} = 75$ A.

This critical current density is similar to the critical pair-breaking current density of a thin wire of Sn. It would allow very high transport currents, if the shielding effect, leading to the restriction of the current to a thin surface layer, can be avoided. Such substances have been developed in form of the hard superconductors.

Using Silsbee's hypothesis, we can also calculate the critical currents of a superconductor in an external magnetic field. One only has to add the vectors of the external field and of the field of the transport current at the surface. The critical current density is reached, when this resulting field attains the critical value.

Next we turn to the type-II superconductors which differ in an important fundamental point from the type-I superconductors. For small magnetic fields and, hence, also for small transport currents, the type-II superconductors reside in the Meissner phase. In this phase, they behave like type-I superconductors, that is, they expel the magnetic field and the current into a thin surface layer. A difference to the type-I superconductors first appears when the magnetic field at the surface exceeds the value B_{c1}. Then the type-II superconductor must enter the Shubnikov phase, that is, flux lines must penetrate into the superconductor.

One finds that in the Shubnikov phase, an "ideal," that is, perfectly homogeneous, type-II superconductor has a finite electric resistance already at very small transport currents. On the other hand, in type-II superconductors containing a large amount of defects, we can observe very large super-currents. These are the "hard superconductors."

With respect to an ideal type-II superconductor, we consider a rectangular plate, carrying a current parallel to the plane of the plate and kept in the Shubnikov phase due to a magnetic field $B_a > B_{c1}$ oriented perpendicular to the plate (Figure 1.1.1.8).

As the first important result of such an experiment, one finds that under these conditions the transport current I is distributed over the total cross-section of the plate, that is, it is not completely restricted anymore to a thin surface layer. After the penetration of the magnetic flux into the superconducting sample, the transport current can flow also within the interior of the superconductor. The transport current, say, along the x-direction, also passes through the vortices, that is, through regions, where a magnetic field is present. This causes a Lorentz force between the vortices and the current. In the case of a current along a wire of length L in a perpendicular magnetic field B_a, the absolute magnitude of this force is $F = I \cdot L \cdot B$. It is oriented perpendicular to B and to the current (here given by the wire axis). Since the transport current is spatially fixed by the boundaries of the

6) Since the penetration depth is only a few 10^{-6} cm, for macroscopic wires we always have $R \gg \lambda_L$. Therefore, for our considerations, the surface of the wire can be treated as a plane.

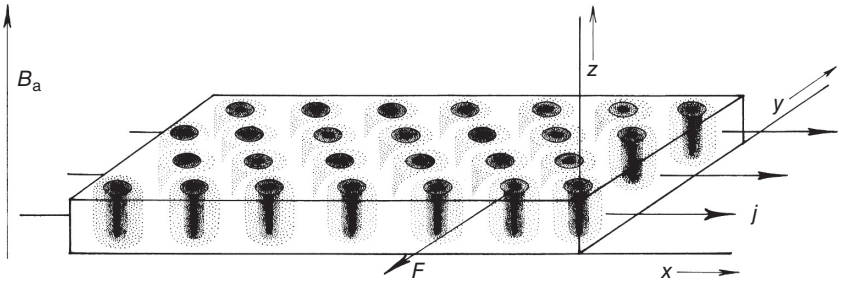

Figure 1.1.1.8 Shubnikov phase in the presence of a transport-current density *j*. The flux lines experience a force *F* driving them along the *y*-direction. The magnetic-field distribution around the flux lines is indicated by the hatching.

plate, under the influence of the Lorentz force the vortices must move perpendicular to the current direction and to the magnetic field, that is, perpendicular to their own axis [23]. For ideal type-II superconductors, in which the free motion of the vortices is possible, this vortex motion should appear already at arbitrarily small forces and, hence, at arbitrarily small transport currents. However, the vortex motion across the superconductor causes dissipation, that is, electric energy is changed into heat. This energy can only be taken from the transport current by means of an electric voltage appearing along the sample. Hence, the sample shows electric resistance.

Therefore, ideal type-II superconductors are useless for technical applications, say, for building magnets, in spite of their high critical field B_{c2}. Finite critical currents in the Shubnikov phase can only be obtained if the vortices in some way are bound to their locations.

Such pinning of the vortices can indeed be achieved by incorporating suitable "pinning centers" into the material. In the simplest way, we can understand the effect of pinning centers by means of an energy consideration. The formation of a vortex requires a certain amount of energy. This energy is contained, say, in the circulating currents flowing around the vortex core. We see that, for the given conditions, a vortex is associated with a certain amount of energy per unit length, that is, the longer the flux line the larger is also the energy needed for its generation. We denote this energy by ε^*. It can be estimated from the lower critical field B_{c1}, above which magnetic flux starts to penetrate into a type-II superconductor. The resulting gain in expulsion energy suffices for generating the vortices in the interior. For simplicity, we consider again a long cylinder in a magnetic field parallel to its axis, that is, a geometry with zero demagnetization coefficient. At B_{c1}, the penetration of the magnetic flux results in n flux lines per unit area. Each flux line carries just one flux quantum Φ_0. This requires the energy

$$\Delta E_F = n \cdot \varepsilon^* \cdot L \cdot F \tag{1.1.1.13}$$

where n is the number of flux lines per unit area, ε^* is the energy per unit length of vortex, L is the sample length, and F is the sample cross-section.

The gain in magnetic expulsion energy is

$$\Delta E_{\mathrm{M}} = B_{\mathrm{c1}} \cdot \Delta M \cdot V \tag{1.1.1.14}$$

where ΔM is the change of the magnetization of the sample and $V = L{\cdot}F$, is the sample volume.

ΔM can be expressed in terms of the penetrated flux quanta. We have

$$\Delta M = \frac{n \cdot \Phi_0}{\mu_0} \tag{1.1.1.15}$$

This yields for the gain in expulsion energy

$$\Delta E_M = \frac{1}{\mu_0} B_{c1} \cdot n \cdot \Phi_0 L \cdot F \tag{1.1.1.16}$$

If both energy changes are being set equal ($\Delta E_{\mathrm{F}} = \Delta E_{\mathrm{M}}$), from the definition of B_{c1} we obtain

$$n \cdot \varepsilon^* \cdot L \cdot F = \frac{1}{\mu_0} \cdot B_{\mathrm{c1}} \cdot n \cdot \Phi_0 \cdot L \cdot F \tag{1.1.1.17}$$

and hence

$$\varepsilon^* = \frac{1}{\mu_0} \cdot B_{\mathrm{c1}} \cdot \Phi_0 \tag{1.1.1.18}$$

From our knowledge of the vortex energy ε^*, we can easily understand the pinning effect of normal precipitates. If a vortex can pass through a normal-conducting inclusion, its length within the superconducting phase and thereby its energy are

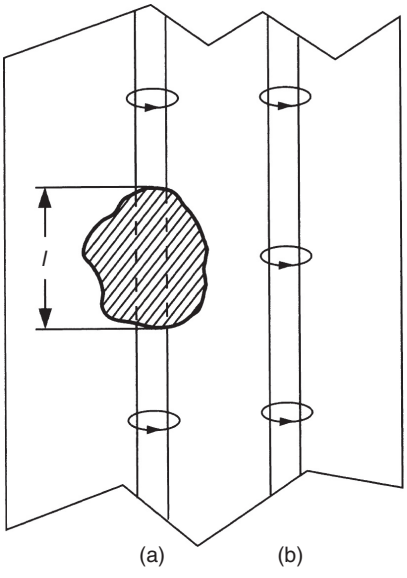

Figure 1.1.1.9 Pinning effect of normal-conducting precipitates. In location (a), the effective length of the vortex is shorter compared to location (b), since in the normal-conducting region there are no circulating currents.

reduced. In Figure 1.1.1.9, this is schematically indicated. The hatched region indicates the normal inclusion. A vortex in location (a) has an energy smaller by the amount $\varepsilon^* \cdot l$ compared to one in location (b). This means that we must supply the energy $\varepsilon^* \cdot l$ to the vortex, in order to move it from (a) to (b). Hence, a force is needed to effect this change in location.

If there are many pinning centers, the vortices will attempt to occupy the energetically most favorable locations. As shown in Figure 1.1.1.10, they will also bend in order to reach the minimum value of the total energy. The length increment caused by the bending must be overcompensated by the effective shortening within the normal-conducting regions. In a vortex lattice, as it is generated in the Shubnikov phase, in the total energy balance we must take into account also the repulsive forces acting between the flux lines.

In principle, also other pinning centers, say, lattice defects, can be understood in the same way. Every inhomogeneity of the material, which is less favorable for superconductivity, acts as a pinning center, with the completely normal state representing the limiting case. For example, superconducting precipitates, however, with a lower transition temperature in general act as pinning centers. We will not

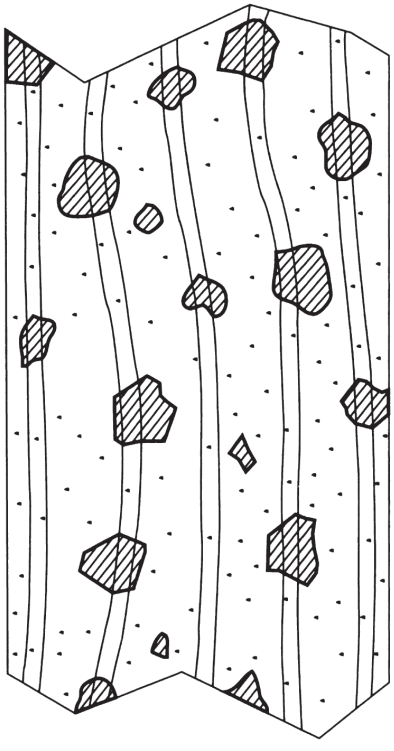

Figure 1.1.1.10 Vortex configuration in a hard superconductor. The hatched regions represent pinning centers. The dots indicate atomic defects.

go into details but mention details can be very complicated. It is still a high art to obtain superconductors which sustain a large transport current.

The effect of the pinning centers can also be described in terms of an energy landscape. Now the pinning center represents a potential well of depth E_p. The vortex is located at its most favorable position, similar to a ball at the lowest point of a bowl. If the ball is to be displaced from this location, one needs a force in order to supply the increase of the potential energy. For removing the ball from its most favorable location, we must supply the energy needed to lift the ball out of the bowl. Usually, in a material there exist many pinning centers, which are irregularly distributed and which have different energy depths E_p. If the superconductor is cooled below T_c in a magnetic field, the vortices will quickly occupy the potential wells, instead of generating a regular triangular lattice. At best, we have a distorted lattice, or in the extreme case even a glassy state [24].

The deviation of an individual vortex from its ideal location within the triangular vortex lattice depends not only on the depth of the potential wells but also on the configuration of all other vortices, because of the repulsive interaction between them. An energetically highly unfavorable arrangement of the vortices will be changed quickly because of the thermal fluctuations. These fluctuations can provide the energy difference ΔE, needed for leaving the potential well, with a probability $w = \exp(-\Delta E/k_B T)$. In this case, the thermodynamic fluctuations can reduce the depth of the potential well, or they can supply the missing energy to the vortex. At low temperatures and for large values of ΔE, this probability can become very small, such that the state with the lowest energy cannot be occupied anymore. Furthermore, because of the interaction between the vortices, ΔE can approach infinity. In this case, we deal with the state of the vortex glass, which experiences no changes anymore within finite times.

Next, we want to discuss the effect of the pinning centers during the current transport in superconducting wires or thin films. We have seen that an ideal type-II superconductor in the Shubnikov phase cannot carry a current perpendicular to the direction of the magnetic field without dissipation. However, in a *real* superconductor, the vortices are never completely freely mobile. There is always a perhaps very small force necessary in order to tear the vortices off the pinning centers which are practically always present. The strength of the pinning forces acting on the individual vortices will have a certain distribution about an average value F_H. Also, the whole vortex lattice will affect the pinning forces due to collective effects. However, for simplicity, we will only speak of a single pinning force F_H.

As long as the Lorentz force F_L is smaller than the pinning force F_H, the vortices cannot move. Therefore, also in every real type-II superconductor in the Shubnikov phase, we will be able to observe current flow without dissipation. If the transport current exceeds its critical value at which $F_L = F_H$, the vortex motion sets in, and electric resistance appears.[7] We see that the critical current

7) If the pinning forces acting on the individual vortices are different, initially the most weakly pinned vortices will start moving, resulting in only a relatively small resistance. With increasing current, their number and, hence, the sample resistance will approach a certain limiting value.

is a measure of the force F_H, with which the vortices are pinned at energetically favored locations.

By means of a systematic study of the hard superconductors, one has been able to develop empirically quite useful materials.

To return to the effect of levitation – applications of this effect are discussed in Sections 4.1 and 4.2 – let us now consider a hard superconductor which is cooled in the field of a permanent magnet. We assume that this field is well above B_{c1}.

Quite in contrast to a standard permanent magnet, but also in contrast to an ideal type-I or type-II superconductor, the hard superconductor will try to keep the field in its interior at the value, at which it was cooled down. After they are pinned, the flux lines do not move anymore as long as the maximum pinning force of the pinning centers is not exceeded. If a hard superconductor is cooled down within a certain distance above a permanent magnet, an *attractive* force is active, if the superconductor is moved away from the magnet. In the same way, a *repulsive* force is active, if the superconductor is moved closer to the permanent magnet. The same applies in the case of any arbitrary directions of the movement. As soon as the external field changes, the hard superconductor generates shielding currents in such a way, that the field (or the vortex lattice) remains unchanged in its interior. Therefore, a hard superconductor, including a loading weight, can not only float above a magnet but also hang freely below a magnet, or placed at an arbitrary angle. This effect is demonstrated in Figure 1.1.1.11 [25]. In this case, properly prepared little blocks of $YBa_2Cu_3O_7$ were mounted within a toy train, and the blocks were cooled down within a certain working distance from the magnets, forming the "train tracks." The train can move along the track practically without friction, since the magnetic field keeps its value along this direction.

When, say in a magnet, the magnetic field is swept between two large values $\pm B_{max}$, vortices are forced to enter and leave the superconductor once the

Figure 1.1.1.11 Hanging toy train [25]. (Institut für Festkörper- und Werkstoffforschung, Dresden. From [1].)

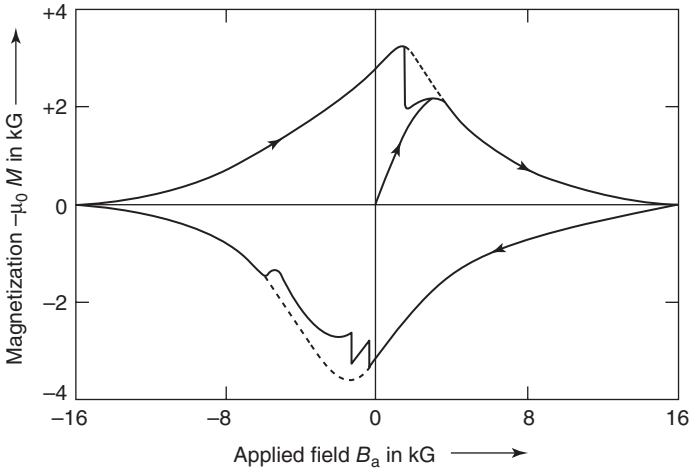

Figure 1.1.1.12 Complete magnetization cycle of a Pb–Bi alloy [26]. The jumps on the solid curve are due to jumps of magnetic flux lines. The dashed curve is expected if there were no such jumps (1 kG = 0.1 T). (From [1].)

pinning force is surpassed. This leads to a hysteresis in the magnetization of the superconductor, see Figure 1.1.1.12. Accompanied with this are, for example, hysteresis losses for alternating magnetic fields.

We want to conclude our discussion of the critical currents in superconductors with a few general remarks. We have seen that the mechanism of pair-breaking results in an intrinsic maximum super-current density. However, in the cases which are technically relevant, the critical current of a superconductor is determined by *extrinsic* properties. On the one hand, the latter properties in the form of pinning centers in the Shubnikov phase only allow a finite super-current, and on the other hand, for example, in the form of grain boundaries in high-temperature superconductors, represent weak regions in the material strongly reducing the maximum super-current. The question, if a new material, say, the iron pnictides, finds interesting technical applications depends on the concrete problems and often can be answered only after a long development period.

In summary, in this chapter, we have seen that the main ingredient of the superconducting state is that electron pairs (Cooper pairs) form a macroscopic matter wave. For conventional superconductors, as described by the BCS theory, the electrons interact via phonons. There are also unconventional superconductors like the cuprates where the pairing mechanism is not yet clear. The well-defined phase of the matter wave leads us to the ideal diamagnetism at not too large fields and to the vortex state in type-II superconductors. Interference effects of coupled matter waves are the basis of the physics of Josephson junctions and of SQUIDs. We have further introduced important length scales like the London penetration depth λ_L (the scale over which magnetic fields decay inside the superconductor), the Ginzburg–Landau coherence length ξ_{GL} (the scale over which the amplitude of the matter wave and thus the Cooper pair density varies), and the BCS coherence

length ξ_0 (the scale over which the two partners of a Cooper pair are correlated). We also mentioned that unpaired electrons are separated by an energy gap Δ from a Cooper pair and we have seen that there is a maximum field, as well as a maximum current a superconductor can carry.

References

1. Buckel, W. and Kleiner, R. (2004) *Superconductivity, Fundamentals and Applications*, 2nd edn, Wiley-VCH Verlag GmbH.
2. Buckel, W. and Kleiner, R. (2012) *Supraleitung, Grundlagen und Anwendungen*, 7th German edn, Wiley-VCH Verlag GmbH.
3. Kamerlingh-Onnes, H. (1908) *Proc. R. Acad. Amsterdam*, **11**, 168.
4. Kamerlingh-Onnes, H. (1913) *Commun. Leiden*, Suppl. Nr. **34**.
5. Kamerlingh-Onnes, H. (1911) *Commun. Leiden*, **120b**.
6. Bardeen, J., Cooper, L.N., and Schrieffer, J.R. (1957) *Phys. Rev.*, **108**, 1175.
7. Bednorz, J.G. and Müller, K.A. (1986) *Z. Phys. B*, **64**, 189.
8. Raub, C.J. (1988) *J. Less-Common Met.*, **137**, 287.
9. (a) Wu, M.K., Ashburn, J.R., Torng, C.J., Hor, P.H., Meng, R.L., Gao, L., Huang, Z.J., and Chu, C.W. (1987) *Phys. Rev. Lett.*, **58**, 908; (b) Zhao, Z.X. (1987) *Int. J. Mod. Phys. B*, **1**, 179.
10. Kirtley, J.R. and Tsuei, C.C. (1996) *Spektrum der Wissenschaften*, German edition of Scientific American, p. 58, Oktober 1996.
11. Nagamatsu, J., Nakagawa, N., Muranaka, T., Zenitani, Y., and Akimitsu, J. (2001) *Nature*, **410**, 63.
12. Takahashi, H., Igawa, K., Arii, K., Kamihara, Y., Hirano, M., and Hosono, H. (2008) *Nature*, **453**, 376.
13. Meissner, W. and Ochsenfeld, R. (1933) *Naturwissenschaften*, **21**, 787.
14. (a) Cribier, D., Jacrot, B., Madhav Rao, L., and Farnoux, B. (1964) *Phys. Lett.*, **9**, 106; (b) see also:Gorter, C.J. (ed.) (1967) *Progress Low Temperature Physics*, vol. **5**, North Holland Publishing Comp, Amsterdam, p. 161 ff.
15. Essmann, U. and Träuble, H. (1967) *Phys. Lett.*, **24 A**, 526 and *J. Sci. Instrum.* (1966) **43**, 344.
16. Doll, R. and Näbauer, M. (1961) *Phys. Rev. Lett.*, **7**, 51.
17. Deaver, B.S. Jr., and Fairbank, W.M. (1961) *Phys. Rev. Lett.*, **7**, 43.
18. (a) London, F. and London, H. (1935) *Z. Phys.*, **96**, 359; (b) London, F. (1937) *Une conception nouvelle de la supraconductivite*, Hermann and Cie, Paris.
19. Lock, J.M. (1951) *Proc. R. Soc. London, Ser. A*, **208**, 391.
20. Jackson, T.J., Riseman, T.M., Forgan, E.M., Glückler, H., Prokscha, T., Morenzoni, E., Pleines, M., Niedermayer, C., Schatz, G., Luetkens, H., and Litterst, J. (2000) *Phys. Rev. Lett.*, **84**, 4958.
21. Pippard, A.B. (1950) *Proc. R. Soc. London, Ser. A*, **203**, 210.
22. Silsbee, F.B. (1916) *J. Wash. Acad. Sci.*, **6**, 597.
23. Gorter, C.J. (1962) *Phys. Lett.*, **1**, 69.
24. Blatter, G., Feigel'man, M.V., Geshkenbein, V.B., Larkin, A.I., and Vinokur, V.M. (1994) *Rev. Mod. Phys.*, **66**, 1125.
25. Schultz, L., Krabbes, G., Fuchs, G., Pfeiffer, W., and Müller, K.-H. (2002) *Z. Metallkd.*, **93**, 1057.
26. (a) Campbell, A.M., Evetts, J.E., and Dew Hughes, D. (1964) *Philos. Mag.*, **10**, 333; (b) Evetts, J.E., Campbell, A.M., and Dew Hughes, D. (1964) *Philos. Mag.*, **10**, 339.

1.1.2

Review on Superconducting Materials

Roland Hott, Reinhold Kleiner, Thomas Wolf, and Gertrud Zwicknagl

1.1.2.1 Introduction

The discovery of superconductivity was the result of straightforward research to see how low one can go concerning the electrical resistance of metals: studies on alloys and temperature-dependent measurements had evidenced that it could be decreased by reducing the density of impure atoms as well as by lowering temperature. Mercury offered the best low-impurity perspectives – Kamerlingh Onnes had built up in Leiden a unique cryogenic facility: the jump to apparently zero resistivity that he observed here in 1911 below 4 K came nevertheless as a big surprise [1]. He soon extended the list of superconducting (SC) materials by tin (3.7 K) and lead (7.2 K), and his Leiden successors found thallium (2.4 K) and indium (3.4 K) [2]. Meißner successfully continued the search through the periodic table until 1930 with tantalum (4.2 K), thorium (1.4 K), titanium (0.4 K), vanadium (5.3 K), and niobium, the element with the highest critical temperature, $T_c = 9.2$ K [3] (Figure 1.1.2.1). The extension to binary alloys and compounds in 1928 by de Haas and Voogd was fruitful with SbSn, Sb_2Sn, Cu_3Sn, and Bi_5Tl_3 [4]. Bi_5Tl_3 and, shortly afterwards, a Pb–Bi eutectic alloy established first examples of critical magnetic field values B_{c2} in the tesla range, which revived hope for high-field persistent current SC electromagnets as already envisioned by Kamerlingh Onnes.

After 1930, SC materials research fell more or less asleep until Matthias and Hulm started in the early 1950s a huge systematic search which delivered a number of new compounds with $T_c > 10$ K as well as technically attractive $B_{c2} > 10$ T: NbTi ($T_c = 9.2$ K) and the A15 materials were the most prominent examples. Matthias

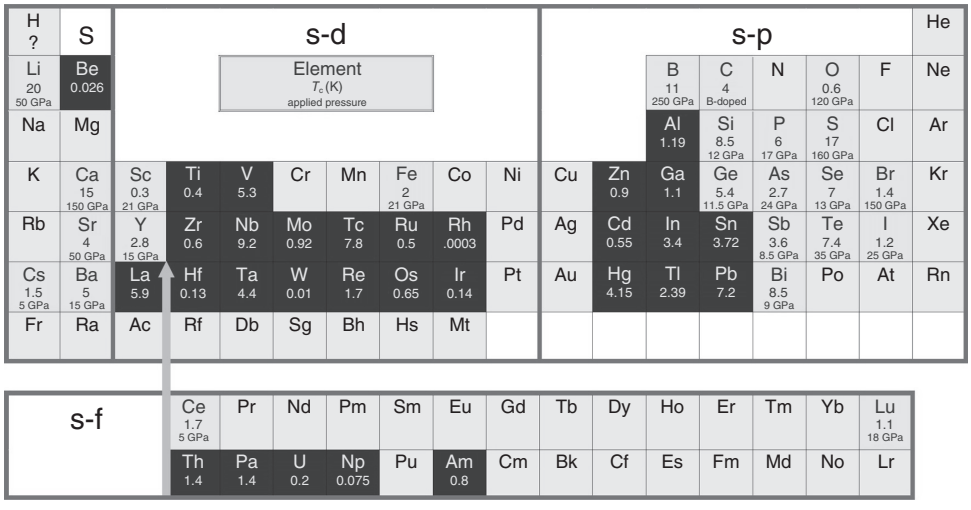

Figure 1.1.2.1 Periodic table with the distribution and T_c [K] of the chemical elements for which superconductivity has been observed with or without application of pressure [1, 5, 6].

condensed his huge practical knowledge from his heroic preparation of some 3000 different alloys into "rules" on how to prepare "good" superconductors: high crystal symmetry, high density of electronic states at the Fermi level, no oxygen, no magnetism, no insulators! [7].

In spite of his inofficial sixth rule "Stay away from theorists!" in 1957 the *Bardeen–Cooper–Schrieffer* (*BCS*) *theory* [8] brought the desperately awaited breakthrough of theoretical solid state physics to a microscopic explanation of superconductivity. The key idea of BCS theory is that in metals even a tiny attractive interaction between the conduction electrons results in the formation of bound electron pair states ("Cooper pairs") which are no longer obliged to obey the Fermi–Dirac statistics which enforced the electrons to occupy high kinetic energy single particle states due to the Pauli principle. The energy gain of the SC state with respect to the normal state does not result from the small binding energy of the pairs, but it is the condensation energy of the pairs merging into a macroscopic quantum state which can be measured as an energy gap for electron excitations into single particle states. Although the BCS theory was derived from the physical idea of attractive electron–phonon coupling, the model-based weak pair coupling theory as its mathematical kernel is well applicable to other pairing mechanisms. BCS theory had an impact not only on solid-state physics but also on elementary particle physics where it was further developed to the Higgs mechanism of mass generation [9].

In 1979, in violation of another Matthias rule, superconductivity was discovered in the magnetic material $CeCu_2Si_2$ as the first representative of *heavy-fermion* (*HF*) *superconductors* [10] where magnetism is suspected as mechanism responsible for the Cooper pairing: in these intermetallic compounds, the electronic degrees of freedom which are responsible for superconductivity are directly linked with magnetic moments of partially filled f-shells of lanthanide or actinide atoms. The superconductivity below a typical $T_c \sim 1$ K seems to arise here from the delicate balance between the localized magnetic moments which try to imprint their magnetic signature on the shielding conduction electrons, and the conduction electrons which try to neutralize these magnetic moments by spin flipping, for example, via Kondo effect [11].

The search for *organic superconductors* had been boosted in the 1960s by the idea that conductive polymer chains with polarizable molecular groups may provide for electrons running along the polymer chains a highly effective Cooper pair coupling by means of an energy exchange via localized excitons [12]. Since the first discovery of an organic superconductor in 1980 [13] $T_c > 10$ K has been achieved [14]. However, the origin of superconductivity has turned out to be far from the suggested excitonic mechanism. Electric conduction stems here from π-electrons in stacked aromatic rings forming one-dimensional or two-dimensional (2D) delocalized electron systems. This restriction of the effective dimensionality and strong Coulomb repulsion effects push the systems toward metal-insulator, magnetic, and SC transitions [15].

The Mermin–Wagner theorem [16] that long-range order cannot exist in two dimensions at finite temperature due to strong fluctuations seemed to restrict

superconductivity to the physical dimension $d = 3$. The *cuprate high-temperature superconductors* (*HTS*) [17] proved in 1986 that the limiting case $d = 2 + \varepsilon$ ($\varepsilon \to 0$), that is, basically 2D CuO layer-oriented superconductivity with slight SC coupling to neighboring CuO layers, can even be enormously beneficial for SC long-range order [18]. The problem for a theoretical description of cuprate HTS within BCS theory and its extensions [19] is not the high T_c of up to 138 K under normal pressure [20], far above the pre-HTS record of 23 K [21]. There is no theoretical argument why a textbook phonon BCS superconductor should not achieve such a high T_c: in the McMillan–Rowell formula [22], the commonly used theoretical T_c approximation, T_c, depends in a very sensitive way on the involved material parameters. The HTS T_c range is readily accessible with a still reasonable parameter choice [23]. The real problem is that, in contrast to the "deep" Fermi sea of quasi-free electrons in classical metals where the Cooper-pair condensed electrons amount only to a small part of the valence electron system ($k_B T_c \ll E_{Fermi}$), in these layered cuprate compounds there is only a "shallow" reservoir of charge carriers ($k_B T_c \sim E_{Fermi}$) which first have to be introduced in the insulating antiferromagnetic (AF) stoichiometric parent compound by appropriate doping. The thus generated normal-conducting state corresponds to a "bad metal" in which Coulomb correlations strongly link the charge and spin degrees of freedom. The BCS recipe to express the SC wavefunction in terms of the normal-metal single particle states does not work here anymore since the macroscopic many-particle wavefunction is thoroughly changing in the superconductive transition: additional electronic degrees of freedom come into play which had not been accessible before in the normal-conducting state. This transition process still lacks a satisfactory theoretical description [24, 25]. Nevertheless, the SC instability in cuprate HTS, as well as in the structurally and chemically related layered cobaltate and ruthenate compounds, is believed to stem predominantly from a magnetic and not from a phononic interaction as in the case of the classical metallic superconductors where magnetism plays only the role of an alternative, intrinsically antagonistic long-range order instability.

Fullerides (C_{60}, C_{70}, …) discovered in 1985 are a third modification of elementary carbon. The superconductivity in C_{60} induced by doping and intercalation of alkali-metal atoms, with T_c values up to 33 K at normal pressure [26], followed soon as another surprise. In spite of the high T_c, superconductivity can be explained by BCS theory based on intramolecular phonons [27]. *Borides* were investigated with respect to high-T_c superconductivity already in the 1950s: the rationale was the BCS T_c-formula [22] where a high characteristic phonon frequency, as provided by the light boron atoms, was predicted to be particularly helpful. In the 1990s, the borocarbide superconductors RE Ni_2B_2C with T_c up to 16.5 K [28] fulfilled this promise at least halfway. However, phonons are here apparently only one of the contributing superconductivity mechanisms: additional magnetism due to localized RE^{3+} 4f-electrons is here weakly interacting with the SC 3d-electrons of the Ni_2B_2 layers. The huge surprise came in 2001 with the discovery of superconductivity up to $T_c = 40$ K in MgB_2, a compound which was well known since the 1950s and which was in 2001 already commercially

available in quantities up to metric tons [29]. In spite of the high T_c, a phononic mechanism is here highly plausible. As a new feature, multiband superconductivity, that is, the coherent coupling of the Cooper-pair instabilities of several Fermi surfaces [30], is essential for the theoretical description of the SC properties [31]. This multiband mechanism plays an even more dominant role in *iron-based superconductors* [32] where the scattering between the Fermi surfaces of up to five Fe-derived electronic bands is apparently the origin of a complicated magnetic superconductive coupling mechanism [33]. $T_c = 26$ K observed for LaFeAsO in 2008 [34] started a "gold rush" where T_c was immediately pushed up to 55 K [35].

The Matthias rules paradigm has thus changed completely: layered materials with strong electronic correlations – that is where you can expect new high-T_c superconductors!

1.1.2.2 Cuprate High-Temperature Superconductors

Cuprate HTS have played an outstanding role in the scientific and technological development of superconductors due to the enormous efforts made to cope with the challenges due to the plethora of preparational degrees of freedom and the inherent tendency toward inhomogeneities and defects in combination with the very short SC coherence lengths of the order of the dimensions of the crystallographic unit cell.

The structural element of HTS compounds related to the location of mobile charge carriers are stacks of a certain number $n = 1, 2, 3, \ldots$ of CuO_2 layers "glued" on top of each other by means of intermediate Ca layers (see Figure 1.1.2.2) [36]. Counterpart of these *active blocks* of $(CuO_2/Ca/)_{n-1}CuO_2$ stacks are *charge reservoir blocks* $EO/(AO_x)_m/EO$ with $m = 1, 2$ monolayers of a quite arbitrary oxide AO_x "wrapped" on each side by a monolayer of alkaline earth oxide EO with E = Ba, Sr (see Figure 1.1.2.2b). The HTS structure results from alternating stacking of these two block units. The general chemical formula

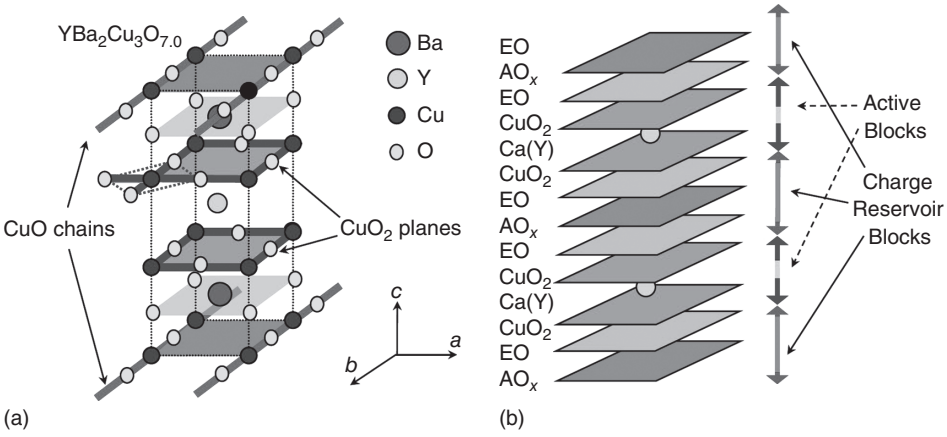

Figure 1.1.2.2 (a) Crystal structure of $YBa_2Cu_3O_7$ ("YBCO") [39]. (b) General structure of a cuprate HTS A-$m2(n-1)n$ ($A_mE_2Ca_{n-1}Cu_nO_{2n+m+2+y}$) for $m = 1$.

$\mathbf{A}_{\boldsymbol{m}}\mathrm{E}_{\mathbf{2}}\mathrm{Ca}_{\boldsymbol{n-1}}\mathrm{Cu}_{\boldsymbol{n}}\mathrm{O}_{2n+m+2+y}$ (see Figure 1.1.2.2b) is conveniently abbreviated as **A-*m*2(*n* − 1)*n*** [37] (e.g., $\mathrm{Bi_2Sr_2Ca_2Cu_3O_{10}}$: Bi-2223) neglecting the indication of the alkaline earth element (see Figure 1.1.2.1). The family of all $n = 1, 2, 3, \ldots$ representatives with common AO_x are referred to as *A-HTS*, for example, Bi-HTS. The most prominent compound $\mathbf{YBa_2Cu_3O_7}$ (see Figure 1.1.2.2a), the first HTS discovered with a critical temperature T_c above the boiling point of liquid nitrogen [38], traditionally abbreviated as "**YBCO**" or "**Y-123**" ($\mathbf{Y_1Ba_2Cu_3}\mathrm{O}_{7-\delta}$), fits into this classification scheme as a modification of Cu-1212 where Ca is completely substituted by Y.

The following scenario (see Figure 1.1.2.3) applies to *hole-doping* [40] as well as to *electron-doping* of all HTS [41]: the undoped compounds are AF insulators up to a critical temperature T_N well above 300 K, with alternating spin orientations of the hole states that are localized around the Cu atoms in the $\mathrm{CuO_2}$ layers. Adding charge carriers by doping relaxes the restrictions of spin alignment: T_N decreases and the insulator turns into a "bad metal." At low temperature, the electric transport shows a dramatic change within a small doping range from an insulating to a SC behavior [42]. For $\mathrm{La_{2-x}Sr_xCuO_4}$, this happens at a critical hole concentration $x = 0.05$ in the $\mathrm{CuO_2}$ planes (see Figure 1.1.2.2). On stronger doping, superconductivity can be observed up to an increasingly higher critical temperature T_c until the maximum T_c is achieved for "optimal doping" ($x \approx 0.16$ for $\mathrm{La_{2-x}Sr_xCuO_4}$). On further doping, T_c decreases again until finally ($x \geq 0.27$ for $\mathrm{La_{2-x}Sr_xCuO_4}$) only normal conducting behavior is observed.

The rationale that the phenomenon of superconductivity in HTS can be conceptually reduced to the physics of the $\mathrm{CuO_2}$ layers [44] has evolved to a more and more 2D view in terms of $\mathrm{CuO_2}$ *planes.* The superconductive coupling

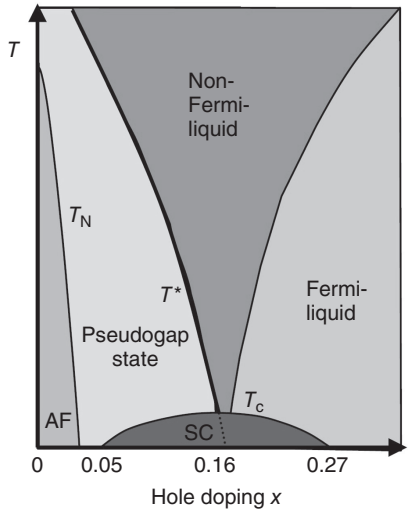

Figure 1.1.2.3 HTS temperature-doping phase diagram with the interplay of antiferromagnetism (AF) and superconductivity (SC) [40, 43].

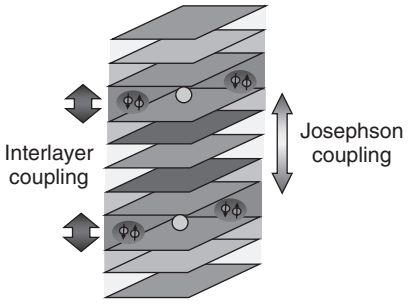

Figure 1.1.2.4 Hierarchy of the superconductive coupling in cuprate HTS.

between these planes within a given $(CuO_2/Ca/)_{n-1}CuO_2$ stack ("interplane coupling") is much weaker than the intraplane coupling, but still much stronger than the superconductive coupling between the $(CuO_2/Ca/)_{n-1}CuO_2$ stacks which can be described as Josephson coupling (see Figure 1.1.2.4).

HTS are extreme type-II superconductors [45] with $\lambda > 100$ nm and $\xi \sim 1$ nm. The quasi-2D nature of superconductivity in HTS leads to a pronounced anisotropy of the SC properties with much higher super-currents along the CuO_2 planes than in the perpendicular direction [46] and a corresponding anisotropy of the magnetic penetration depth λ, for example, $\lambda_{ab} = 750$ nm and $\lambda_c = 150$ nm in optimally doped YBCO [47] (the indices refer to the respective orientation of the magnetic field). Material imperfections of the dimension of the coherence length which are required as pinning centers preventing the flux flow of magnetic vortices are easily encountered in HTS due to their small coherence lengths, for example, for optimally doped YBCO $\xi_{ab} = 1.6$ nm, $\xi_c = 0.3$ nm for $T \to 0$ K [48] which are already comparable to the lattice parameters (YBCO: $a = 0.382$ nm, $b = 0.389$ nm, $c = 1.167$ nm [39]). The high T_c in combination with the small value of coherence volume $(\xi_{ab})^2 \xi_c \sim 1\,\text{nm}^3$ allows large thermally induced magnetic fluctuations in the SC phase at temperature close to T_c, an effect which could be completely neglected in classical superconductors [4]. Moreover, since technical superconductor materials consist of a network of connected grains, already small imperfections at the grain boundaries with spatial extensions of the order of the coherence length lead to a substantial weakening of the SC connection of the grains and thus to "weak-link behavior" of the transport properties which has to be avoided in technical conductor materials [49]. On the other hand, this has been widely exploited for the fabrication of HTS Josephson junctions [50].

The low ξ_c, that is, the weak superconductive coupling between the $(CuO_2/Ca/)_{n-1}CuO_2$ stacks, may lead for *c*-axis transport to an intrinsic Josephson effect within the unit cell even for perfectly single-crystalline materials [51]. If the thickness of the charge reservoir blocks $EO/(AO_x)_m/EO$ in-between these stacks is larger than ξ_c, vortices are here no longer well defined due to the low Cooper pair density (see Figure 1.1.2.5). This leads to a quasi-disintegration of the vortices into stacks of *pancake vortices* which are much more flexible entities

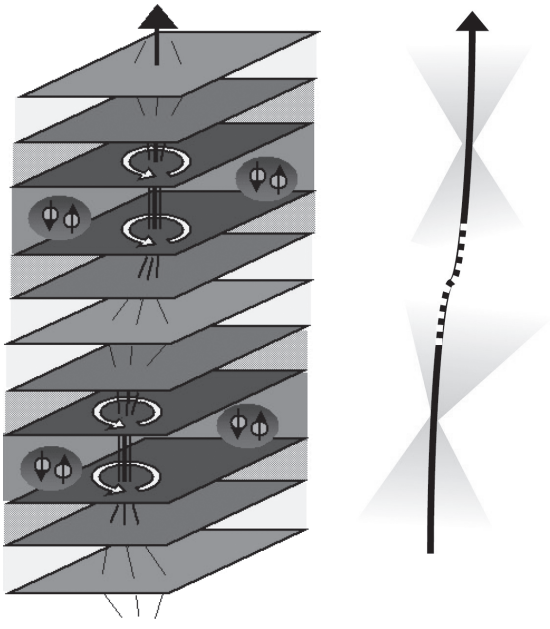

Figure 1.1.2.5 Quasi-disintegration of magnetic vortex lines into "pancake" vortices [52].

than the continuous quasi-rigid vortex lines in conventional superconductors. The effects described in the preceding two paragraphs combine to reduce the *irreversibility field* $B_{\mathrm{irr}}[T]$, the tolerable limit for magnetic fields with respect to SC transport, in cuprate HTS substantially below the thermodynamical critical field $B_{c2}[T]$, a distinction which was more or less only of academic interest in the case of classical superconductor.

Besides these intrinsic obstacles for the transport of super-current in single-crystalline HTS materials, there are additional hurdles since HTS materials are not a homogeneous continuum but rather a network of linked grains (see Figure 1.1.2.6). The mechanism of crystal growth is such that material that cannot be fitted into the lattice structure of the growing grains is pushed forward into the growth front with the consequence that in the end all remnants of secondary phases and impurities are concentrated at the boundaries in-between the grains. Such barriers impede the current transport even if they consist of only a few atomic layers and have to be avoided by careful control of the growth process, in particular of the composition of the offered material. Another obstacle for super-currents in HTS (which is not only detrimental for transport currents but also enables the fabrication of HTS Josephson junctions) is misalignment of the grains: exponential degradation of the super-current transport is observed as a function of the misalignment angle due to the *d*-symmetry of the SC order parameter [53] and even more due the build-up of charge inhomogeneities [54].

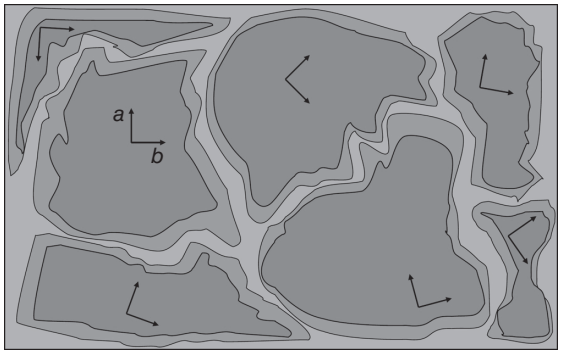

Figure 1.1.2.6 Schematic HTS microstructure with differently oriented single crystal grains separated by secondary phase regions. Oxygen depletion and thus T_c reduction may occur at grain boundaries.

1.1.2.3 Other Oxide Superconductors

The discovery of superconductivity in the *bismuthate* $BaPb_{1-x}Bi_xO_3$ in 1975 with a rather high $T_c \sim 13$ K in those days for $x \sim 0.25$ [55] raised great interest in the mechanism of superconductivity in this at that time quite exotic oxide compound with a low density of states at the Fermi level. The cuprate HTS soon chased away that exotic touch in spite of the rise of T_c to >30 K in $Ba_{1-x}K_xBiO_3$ (BKBO; $x \sim 0.35$) in the middle of the HTS bonanza days [56]: tunneling showed clean gap structures consistent with weak-to-moderate coupling BCS theory [57]. In the parent compound $BaBiO_3$, a three-dimensional (3D) charge-density wave (CDW) arrangement of $Bi^{(4-\delta)+}O_6$ and $Bi^{(4+\delta)+}O_6$ octahedra ($| \delta | \ll 1$) creates a gap at the Fermi level and leads to an insulating electric behavior. K or Pb doping suppresses this CDW by means of the random occupation of the A position with Ba and K or Pb ions in a simple pseudo-cubic ABO_3 solid solution structure [58]. Furthermore, this doping introduces hole carriers and finally results in a metal-insulator transition at a critical doping level $x_c \sim 0.35$. The maximum T_c occurs for slightly higher doping. On further doping, T_c rapidly decreases and finally disappears at the K solubility limit $x \sim 0.65$. The SC pairing mechanism is apparently related to the structural and concomitant electronic 3D CDW instability.

The extensive search for other SC transition metal oxides following the discovery of the cuprate HTS came in 1994 across strontium *ruthenate* (Sr_2RuO_4), a layered perovskite with an almost identical crystal structure as the cuprate HTS $La_{2-x}Sr_xCuO_4$ ("LSCO"), albeit only with a $T_c \sim 1.5$ K [59]. In both materials, the conduction electrons stem from partially filled d-bands (of the Ru or Cu ions, respectively) that are strongly hybridized with oxygen p-orbitals. In contrast to the nearly filled Cu 3d-shell in cuprate HTS with only one hole state, in Sr_2RuO_4, in the formal oxidation state of the ruthenium ion Ru^{4+} four electrons are left in the 4d-shell. The closely related ferromagnetic material $SrRuO_3$ shows the inherent tendency of Ru^{4+} toward ferromagnetism. Hence, in analogy with the cuprate HTS, where on doping the AF ground state of the parent compounds seems to "dissolve" in spin-singlet Cooper pairs in a d-wave orbital channel, it was suggested

that the superconductivity in Sr_2RuO_4 is brought about by spin-triplet pairing where the Ru ions "release" parallel-spin, that is, triplet Cooper pairs in p-wave or even higher odd order angular orbital channels.

$RuSr_2GdCu_2O_8$ (Ru-1212) is a *ruthenate-cuprate hybrid* containing both CuO_2 and RuO_2 layers. It fits into the elucidated cuprate HTS layer structure scheme (see Figure 1.1.2.2b) substituting the Ca of the canonical 1212-HTS structure (or the Y in YBCO, or the RE in RE-123, respectively) by Gd to render $CuO_2/Gd/CuO_2$ stacks, separated by a SrO "wrapping layer" from the RuO_2 layers as "charge reservoir layers." Like rare earth borocarbides (see Chapter 7), Ru-1212 and some other closely related rutheno-cuprate compounds display ferromagnetism and superconductivity coexisting on a microscopic scale [60], with $T_{Curie} \sim 135$ K and T_c up to 72 K for Ru-1212. The $CuO_2/Gd/CuO_2$ stacks are believed to be responsible for the superconductivity, whereas the (ferro)magnetic ordering arises from the RuO_2 layers. A clear intrinsic Josephson effect shows that the material acts as a natural superconductor – insulator – ferromagnet – insulator – superconductor superlattice [61].

Cobaltates made in 2003 their entry into the SC zoo. $T_c = 4.5$ K has been achieved in hydrated sodium cobaltate $Na_{0.3}CoO_2 \cdot 1.4\ H_2O$ [62]. Na provides here the doping. The intercalation of water increases the separation between the CoO_2 layers and seems to be essential for the onset of superconductivity: $Na_{0.3}CoO_2 \cdot 0.6\ H_2O$, with the same formal Co oxidation state but substantially less separation between the CoO_2 layers is not SC [63]. A major difference compared to cuprate HTS is the triangular lattice geometry of the CoO_2 layers which introduces magnetic frustration into the Co spin lattice, in contrast to the square lattice geometry of Cu ions in cuprate HTS which favors unfrustrated AF spin orientation.

β-Pyrochlore oxide superconductors AOs_2O_6 with A = K, Rb, Cs, and respective $T_c = 9.6$, 6.3, 3.3 K [64] have a triangle-based crystal structure, which is in principle even more subject to magnetic frustration [65]. The A ion sits here in a cage formed by the surrounding OsO_6 tetrahedra (see Figure 1.1.2.7) [66]. Anomalous phonons are observed as an anharmonic oscillation ("rattling" motion) of the A ion cage [67]. Intriguingly, the rattling motion participates in the SC properties

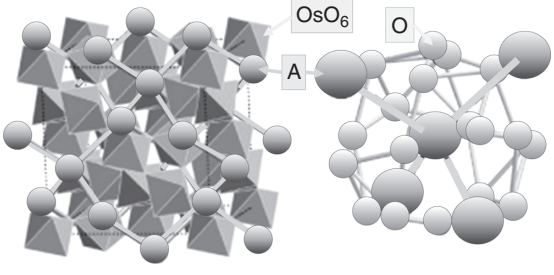

Figure 1.1.2.7 Crystal structure of the β-pyrochlore oxides AOs_2O_6. The A atom is located in an oversized atomic cage made of OsO_6 octahedra and can move with a large excursion along the four [72] directions pointing to the neighboring A atoms in adjacent cages [68].

[68, 69]. Comparing the three compounds, T_c rises with increasing magnitude of the rattling motion and electron–phonon coupling [70], while the density of state decreases [71], opposite to what is expected from BCS theory.

1.1.2.4 Iron-Based Superconductors

The 2D layer structure of iron-based superconductor families ("Fe–Sc") [32, 73] bears close resemblance to the cuprate HTS structure: the transition element atoms (Fe/Cu) are arranged in a quadratic lattice (Figure 1.1.2.8b) and apparently provide the SC mechanism. Instead of the Cu–Cu bonding via O atoms sitting halfway in-between next-nearest Cu atoms in the cuprate HTS, in Fe–Sc the Fe–Fe bonding happens via tetrahedrally arranged P, As, Se, or Te atoms above and underneath the Fe plane and affects the second-nearest Fe neighboring atoms as well (see Figure 1.1.2.8a). The Fe atoms form thus with the (P/As/Se/Te) atoms a network of regular pyramids with alternating upward/downward orientation. For both SC families, optimum T_c is observed for the most symmetric arrangement of these layer geometries, that is, for flat CuO_2 layers [74] and for regular $Fe(P/As/Se/Te)_4$ tetrahedra [75].

A huge difference is the replacibility of the transition metal atoms: in cuprate HTS, 10% substitution of Cu atoms by Zn, the rightward neighboring atom in the periodic table, suppresses superconductivity completely. In $BaFe_{2-x}Co_xAs_2$, the introduction of Co into the Fe layers even introduces superconductivity by the concomitant electron doping, for example, up to $T_c = 24$ K for Co concentration $x = 0.06$ [76]: Fe–Sc apparently tolerate considerable disorder in the Fe planes. Another huge difference: the undoped, "parent" compounds of cuprate HTS are AF insulators whereas Fe–Sc derive from magnetic metal compounds [7]. Electronic correlations in Fe–Sc are certainly weaker than in cuprate HTS, but electron–orbital selective correlation mechanisms in the Fe atoms introduce here novel basic physics [77].

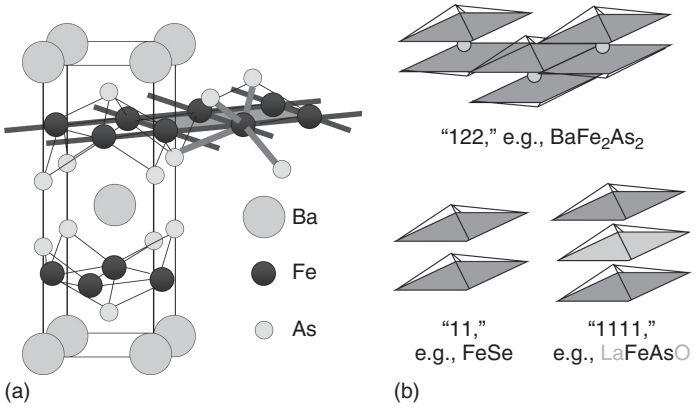

Figure 1.1.2.8 (a) Crystal structure of $BaFe_2As_2$. (b) Schematic structure of the 122, 11, and 1111 Fe–Sc indicating the up/down-orientation of the Fe(P/As/Se/Te) pyramids.

Just like HTS, Fe–Sc are extreme type-II superconductors with $\lambda > 100$ nm [78] and $\xi \sim 1$ nm [79]. For cuprate HTS, the discrepancy between the distance $d \sim 1$ nm in between the SC $(CuO_2/Ca/)_{n-1}CuO_2$ stacks [47] and the coherence length $\xi_c = 0.3$ nm perpendicular to the planes leads to the discussed weak-link behavior. For Fe–Sc, the situation is a bit more benign with the reported $d = 0.86\,\text{nm}/\xi_c = 0.6\,\text{nm}$ for Nd-1111, $d = 0.65\,\text{nm}/\xi_c = 1.5$ nm for Ba-122, and $d = 0.6\,\text{nm}/\xi_c = 0.6\,\text{nm}$ for FeSe [79]. The almost isotropic magnetic field behavior, for example, for Ba-122 with B_{c2} $[T = 0\,\text{K}]$ estimates of ~50 T and 40 T for magnetic fields parallel and perpendicular to the planes, respectively [79], is not related to the supposed isotropic $s_{+/-}$ SC order parameter but stems from the fact that the Fe–Sc are apparently Pauli-limited: the Zeeman splitting of the electronic single-particle states makes it energetically favorable that the Cooper-pairs split into the constituent up- and down-spin states at fields below the "orbital limit" $B_{c2} = \Phi_0/(2\pi\xi^2)$ given by the magnetic flux quantum Φ_0 and the product "ξ^2" of the SC coherence lengths perpendicular to the field.

The restrictions with respect to the crystalline alignment of neighboring grains appear to be much less severe for Fe–Sc than for Cu-HTS: in both cases, for small misalignment angles α, the critical current density J_c is observed to remain more or less constant up to a critical angle α_c, followed by an exponential decrease $J_c \sim e^{-\alpha/\alpha_0}$ for larger α. However, for Fe–Sc the recently reported values $\alpha_c \approx 10°$ and $\alpha_0 \approx 15°$ [80] indicate a much less stringent texture requirement than for cuprate HTS ($\alpha_c \approx 3° - 5°$, $\alpha_0 \approx 3°/5°$). Moreover, it is not clear if this granularity is already an intrinsic limit: the progress achieved in 2011 [80] compared to 2009 [81] gives rise to hope for further substantial improvement.

1.1.2.5 Heavy Fermion Superconductors

HF systems are stoichiometric lanthanide or actinide compounds whose qualitative low-temperature behavior in the normal state closely parallels the one well known from simple metals. The key features are the specific heat which varies approximately linearly $C \sim \gamma T$, the magnetic susceptibility which approaches a temperature independent constant $\chi(0)$, and the electrical resistivity which increases quadratically with temperature $\rho(T) = \rho_0 + AT^2$. However, the coefficient $\gamma \sim 1\,\text{J mol}^{-1}\,\text{K}^{-2}$ as well as $\chi(0)$ are enhanced by a factor of 100–1000 as compared to the values encountered in ordinary metals while the Sommerfeld–Wilson ratio $[\pi(k_B)^2\ \chi(0)]/[3(\mu_B)^2\gamma]$ is of order unity. The large enhancement of the specific heat is also reflected in the quadratic temperature coefficient A of the resistivity $A \sim \gamma^2$. These features indicate that the normal state can be described in terms of a Fermi liquid [82]. The excitations determining the low-temperature behavior correspond to heavy quasiparticles whose effective mass m^* is strongly enhanced over the free electron mass m. The characteristic temperature T^* which can be considered as a fictitious Fermi temperature or, alternatively, as an effective band width for the quasiparticles is of the order 10–100 K. Residual interactions among the heavy quasiparticles lead to instabilities of the normal Fermi liquid state. A hallmark of these systems is the competition or coexistence of various different cooperative phenomena

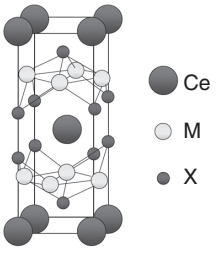

Figure 1.1.2.9 Conventional unit cell of CeM_2X_2 (M = Cu, Ni, Ru, Rh, Pd, Au, …; X = Si, Ge) and URu_2Si_2.

which results in highly complex phase diagrams. Of particular interest are the SC phases which typically form at a critical temperature $T_c \leq 2$ K [83]. $PuCoGa_5$ with $T_c \sim 18.5$ K is up to now the only "high-T_c" HF representative [84].

The discovery of superconductivity in $CeCu_2Si_2$ ($T_c = 1.5$ K; see Figure 1.1.2.9) [10] forced condensed-matter physicists to revise the generally accepted picture of the electrons occupying the inner shells of the atoms. Traditionally, the corresponding states were viewed as localized atomic-like orbitals which are populated according to Hund's rules in order to minimize the mutual Coulomb repulsion. This leads to the formation of local magnetic moments which tend to align and which are weakly coupled to the delocalized conduction electrons. The latter were viewed as "free" fermions which occupy coherent Bloch states formed by the valence orbitals of the atoms. Usually, Cooper pairs which characterize a SC phase are broken by magnetic centers. The damaging effect of 4f- and 5f-ions was well established by systematic studies of dilute alloys. In stark contrast, in $CeCu_2Si_2$ [10] the magnetic degrees of freedom of the partially filled f-shells must generate superconductivity since the non-f reference compound $LaCu_2Si_2$ remains normal.

During the past decade, it became clear that there are different routes to heavy fermion behavior [85] where the magnetic degrees of freedom of the partially filled f-shells form a strongly correlated paramagnetic Fermi liquid with an effective Fermi energy of the order of 1 – 10 meV [86]. In Ce- and Yb-based compounds, the heavy quasiparticles with predominantly 4f-character arise through the Kondo effect in the periodic lattice [87]. For the actinide compounds, increasing experimental evidence points toward a dual character of the 5f-electrons with some of them being delocalized forming coherent bands while others stay localized reducing the Coulomb repulsion by forming multiplets [85, 88]. In Pr skutterudites, on the other hand, the quasiparticles are derived from the conduction states whose effective masses are strongly renormalized by low-energy excitations of the Pr 4f-shells [89]. It is generally agreed that the pairing interaction in HF superconductors is of electronic origin.

In the past decade, superconductivity at ambient pressure was found in the Ce-based HF superconductors CeM_mIn_{3+2m} (M = Ir or Co; $m = 0$, 1) [90]. The most prominent member of this family is $CeCoIn_5$, which has a relatively high $T_c = 2.3$ K (see Figure 1.1.2.10) [91]. Of fundamental interest is the discovery of HF superconductivity in $CePt_3Si$ ($T_c = 0.75$ K; see Figure 1.1.2.11) [92] which crystallizes in a lattice without inversion symmetry [93]. Highly promising systems with tailored violation of local inversion symmetry are artificial superlattices consisting of the

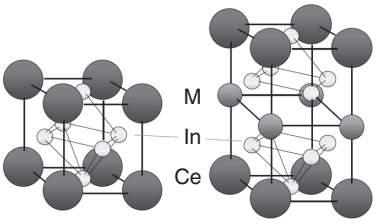

Figure 1.1.2.10 Unit cell of $CeIn_3$ and $CeMIn_5$ (M = Co, Ir).

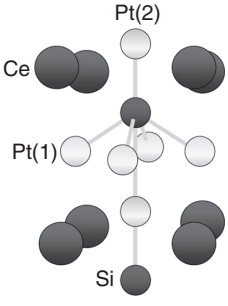

Figure 1.1.2.11 Crystal structure of $CePt_3Si$.

HF superconductor $CeCoIn_5$ and its conventional metallic counterpart $YbCoIn_5$ [94]. It remains a major challenge to give reasons for the apparent asymmetry between Ce- and Yb-based HF systems, that is, to explain why there is a great variety of Ce-based HF superconductors but only one weak Yb-based HF superconductor β-$YbAl_4B$ [95]. HF superconductivity is found more frequently in intermetallic actinide-compounds than in lanthanide-compounds. This may be related to the different nature of heavy quasiparticles in actinide-compounds where the 5f-electrons have a considerable, though orbitally dependent, degree of delocalization. The genuine Kondo mechanism is not appropriate for heavy quasiparticle formation as in lanthanide-compounds. This may lead to more pronounced delocalized spin fluctuations in U-compounds which mediate unconventional Cooper pair formation. AF order, mostly with small moments of the order 10^{-2} μ_B is frequently found to envelop and coexist with the SC phase.

UPt_3 (see Figure 1.1.2.12) [96] exhibits triplet pairing. It sticks out as the most interesting case of unconventional superconductivity with a multicomponent order parameter whose degeneracy is lifted by a symmetry-breaking field due to a small moment AF order. In contrast, in UPd_2Al_3 (see Figure 1.1.2.13) [97] superconductivity coexists with large moment antiferromagnetism. Probably spin singlet pairing is realized. There is experimental evidence for a new kind of magnetic pairing mechanism mediated by propagating magnetic exciton modes. The sister compound UNi_2Al_3 [98] is an example of coexistence of large moment antiferromagnetism with a SC triplet order parameter. In URu_2Si_2 [99], the SC order parameter symmetry is still undetermined. The interest in this compound is focused more on the enveloping phase with a "hidden" order parameter presumably of quadrupolar type or an "unconventional" spin density wave (SDW)

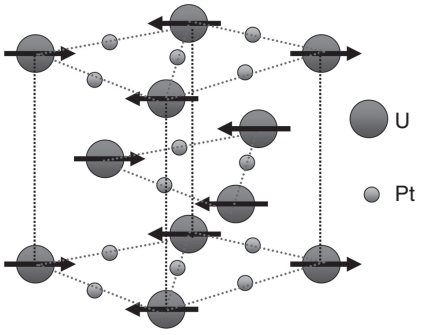

Figure 1.1.2.12 Crystal structure of UPt_3 and AF magnetic structure ($T < T_N = 5.8$ K).

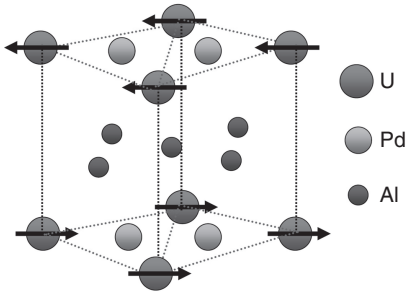

Figure 1.1.2.13 Conventional unit cell of UPd_2Al_3 and simple AF magnetic structure.

[100]. The oldest cubic U-HF superconductor UBe_{13} [101] and its thorium alloy $U_{1-x}Th_xBe_{13}$ is also the most mysterious one. While for the pure system there is a single SC phase of yet unknown symmetry, in the small Th concentration range two distinct phases exist which either may correspond to two different SC order parameters or may be related to a coexistence of superconductivity with a SDW phase. In UGe_2 [102], ferromagnetism and superconductivity coexist. Due to the ferromagnetic polarization the triplet gap function contains only equal spin pairing.

The possibility of coexisting ferromagnetism and superconductivity was first considered by Ginzburg [103] who noted that this is only possible when the internal ferromagnetic field is smaller than the thermodynamic critical field of the superconductor. Such a condition is hardly ever fulfilled except immediately below the Curie temperature T_C where coexistence has been found in a few superconductors with local moment ferromagnetism and $T_C < T_c$ such as $ErRh_4B_4$ and $HoMo_6S_8$. If the temperature drops further below T_C, the internal ferromagnetism molecular field rapidly becomes larger than H_{c2} and superconductivity is destroyed. The reentrance of the normal state below T_C has indeed been observed in the above compounds.

The transuranium-based superconductors $PuCoGa_5$ ($T_c = 18.5$ K) [84], $PuRhGa_5$ ($T_c = 8.7$ K) [104], and $NpPd_5Al_2$ ($T_c = 4.9$ K) [105] are all unconventional superconductors at ambient pressure with the highest transition

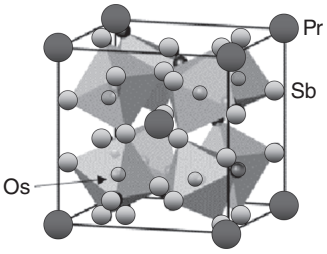

Figure 1.1.2.14 Cubic crystal structure of the filled skutterudite RT_4X_{12}. The T atoms are located in the center of the X octahedra.

temperatures T_c among all the HF superconductors. The HF superconductor $PrOs_4Sb_{12}$ [106] is potentially of similar interest as UPt_3 because it represents the second example of multiphase superconductivity [107] with a critical temperature $T_c = 1.85$ K. The skutterudites RT_4X_{12} (R = alkaline earth, rare earth or actinide; T = Fe, Ru, or Os and X = P, As, or Sb) show a cage structure where large voids formed by tilted T_4X_{12} octahedrons can be filled with R atoms (see Figure 1.1.2.14). They are, however, rather loosely bound and are therefore subject to large anharmonic oscillations ("rattling") in the cage.

1.1.2.6 Organic and Other Carbon-Based Superconductors

Carbides, for example, NbC ($T_c = 12$ K) [108, 109] and MoC ($T_c = 14.3$ K) [109, 110], were among the first discovered compound superconductors and contended in these early days of superconductivity with nitrides and borides for the highest T_c.

Theoretical speculations of superconductivity in organic compounds [12] were met for a long time with total disbelief from the experimental side, for example, from B. Matthias. Things changed when immediately after Matthias's death in 1980 superconductivity was discovered below 0.9 K in the compound $(TMTSF)PF_6$ under a hydrostatic pressure of 12 kbar, with the organic molecule TMTSF (tetra-methyl-tetra-selenium-fulvalene; see Figure 1.1.2.15) [13]. Meanwhile, a number of TMTSF-based superconductors with $T_c \sim 1$ K have been found, for example, $(TMTSF)_2ClO_4$ which becomes SC at 1 K already under normal pressure conditions [111]. The organic molecules are stacked here on top of each other (see Figure 1.1.2.15). The general chemical formula is $(TMTSF)_2X$ where X denotes an electron acceptor such as PF_6, ClO_4, AsF_6, or TaF_6. In the normal state, the TMTSF compounds have a relatively large electric conductivity along the stacks, but only a small conductivity perpendicular to the stacks, thus forming nearly one-dimensional (normal) conductors. The TMTSF compounds are type-II superconductors with highly anisotropic properties. For example, in $(TMTSF)_2ClO_4$ along the stacks the Ginzburg – Landau coherence length is about 80 nm, whereas along the two perpendicular directions of the crystal axes it is about 35 and 2 nm, respectively. The latter value is of the same order of magnitude as the lattice constant along the *c*-axis. Hence, the compound represents a nearly 2D superconductor [72].

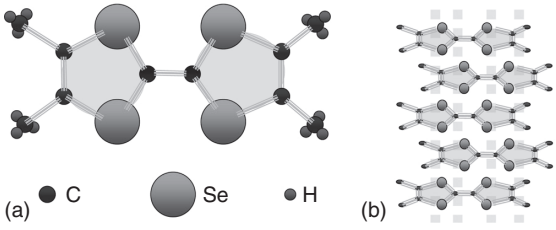

Figure 1.1.2.15 (a) Structure of the organic molecule tetra-methyl-tetra-selenium-fulvalene (TMTSF). (b) Stack arrangement of the molecules forming one-dimensional conduction channels.

Another important class of organic superconductors, often exhibiting T_c well above 1 K, is based on the bis-ethylene-dithia-tetra-thiafulvalene molecule, abbreviated as "BEDT-TTF" or "ET." $(BEDT\text{-}TTF)_2Cu[N(CN)_2]Br$ becomes SC at 11.2 K [14], $(BEDT\text{-}TTF)_2Cu(NCS)_2$ at 10.4 K. The ET-compounds are also highly anisotropic. However, in contrast to the TMTSF-compounds, in the normal state they form 2D layered structures with a large electric conductivity in two dimensions. Like the TMTSF-based materials, the ET-compounds are type-II superconductors, with very short out-of-plane coherence lengths. These compounds thus also represent SC layered structures making them in many respects similar to HTS. The pairing mechanism of the organic superconductors is at present still unclear as well. At least some compounds appear to be d-wave superconductors, in the compound $(TMTSF)_2PF_6$ one may even deal with a spin-triplet superconductor [112].

The quasi-2D organic superconductors are prime candidates for exhibiting the long-sought Fulde–Ferrell–Larkin–Ovchinnikov ("FFLO/LOFF") phases [113]. When the magnetic field is applied parallel to the conducting planes, the orbital critical field is strongly enhanced and superconductivity is Pauli limited. First thermodynamic evidence for the formation of a FFLO/LOFF state was found in κ-$(BEDT\text{-}TTF)_2Cu(NCS)_2$ [114]. The angle-dependence of the formation of the FFLO/LOFF state was demonstrated in [115].

In 1994 superconductivity was found in *boron carbides* [116] (see the Chapter 7), in 2004 in *diamond* with T_c up to 4 K when doped with boron [6] and up to 11.4 K in thin films [117]. For yttrium and rare earth carbide compounds T_c as high as 18 K [118] was reported. Superconductivity in a graphite intercalation compound was first observed in 1965 [119] on KC_8 which exhibits very low critical temperature $T_c = 0.14$ K [120]. Later, several ternary graphite intercalation compounds revealed higher T_c of 1.4 K for $KHgC_8$ [121] and 2.7 K for $KTl_{1.5}C_4$ [122]. Recently, the discovery of high critical temperatures in graphite intercalation compounds YbC_6 ($T_c = 6.5$ K) [123], CaC_6 ($T_c = 11.5$ K) [124], and $Li_3Ca_2C_6$ ($T_c = 11.15$ K) [125] has renewed the interest in this family of materials [123].

Fullerides are compounds of the form A_3C_{60} which may become SC on the admixture of alkali atoms or of alkaline earth atoms [126]: Rb_3C_{60} has a value of T_c of 29.5 K, the present record under pressure is held by Cs_3C_{60} with $T_c = 40$ K [27, 127]. The crystal structure of the fullerides is face-centered cubic, with

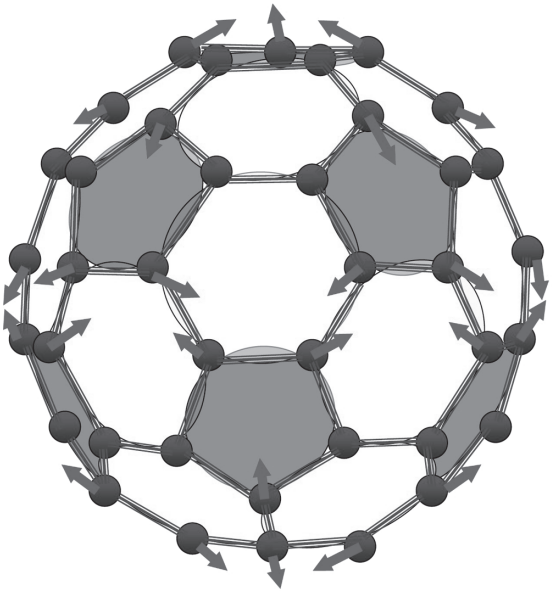

Figure 1.1.2.16 Structure of the C_{60} molecule. The arrows indicate one of the intramolecular phonon modes which are believed to be mainly responsible for the SC pairing [27].

the alkali atoms occupying interstitial sites between the large C_{60} molecules. Fullerides are BCS-like s-wave superconductors. Intramolecular C_{60} phonons (see Figure 1.1.2.16) seem to contribute the most important part of the pairing interactions [27]. However, for body-centered cubic A15-structured Cs_3C_{60} (which is not SC at ambient pressure), an apparently purely electronic transition to a SC state with T_c up to 38 K can be induced by pressure, where the T_c dependence on pressure cannot be described by BCS theory in terms of the induced changes of anion packing density [128].

Recent experiments on alkali-doped *picene* and *dibenzopentacen,* hydrocarbon molecules made up of an assembly of five and seven fused benzene rings, respectively, reported superconductivity up to T_c of 18 [129] and 33 K [130], respectively. A linear increase of T_c with the number of constituent benzene rings is suspected. However, the fabrication process cannot be controlled yet sufficiently to achieve single-phase preparation. This holds true even more for *carbon nanotubes* where long-standing speculations on superconductivity [131] have now been confirmed experimentally for the case of double-wall carbon nanotubes (DWNTs) with resistively measured $T_c = 6.8$ K [132].

1.1.2.7 Borides and Borocarbides

Rare earth borocarbide superconductors have provided the first example of a homogeneous coexistence of superconductivity and ferromagnetism for all temperatures below T_c*:* the two antagonistic long-range orders are carried by different species of electrons that interact only weakly through contact exchange

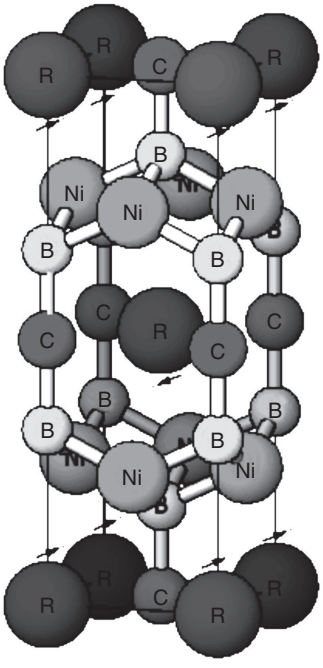

Figure 1.1.2.17 Structure of the layered transition metal borocarbides RNi_2B_2C.

interaction leading to a small effect of the local moment molecular field on the SC conduction electrons. The nonmagnetic rare earth borocarbides have extremely large gap anisotropy ratios $\Delta_{max}/\Delta_{min} \geq 100$ [133]. Surely, the standard electron–phonon mechanism has to be supplemented by something else, perhaps anisotropic Coulomb interactions to achieve this "quasi-unconventional" behavior in borocarbides.

The SC class of layered transition metal borocarbides RNi_2B_2C (nonmagnetic R = Y, Lu, Sc; magnetic R = lanthanide elements in a R^{3+} state; see Figure 1.1.2.17) was discovered in 1994 [116, 134–136]. The crystal structure consists of R C rock-salt-type planes separated by Ni_2B_2 layers built from NiB_4 tetrahedra and stacked along the *c*-axis. More general structures with more than one R C layer are possible [135]. The nonmagnetic borocarbides have relatively high T_c values of around 15 K. There is evidence that the SC mechanism is primarily of the electron–phonon type, although this cannot explain the large anisotropy of the SC gap. At first sight, the layered structure is similar to the HTS cuprates. However, unlike the copper oxide planes the NiB_2 planes show buckling. As a consequence, the electronic states at the Fermi level in the borocarbides do not have quasi-2D $d_{x^2-y^2}$ character and, therefore, have much weaker correlations excluding the possibility of AF spin-fluctuation-mediated superconductivity.

The discovery of superconductivity in MgB_2 (see Figure 1.1.2.18) in early 2001 with $T_c \sim 40$ K, came as a huge surprise since this simple material was

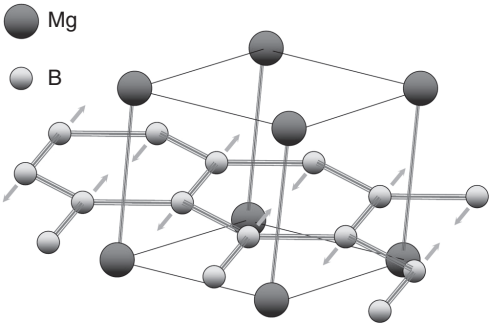

Figure 1.1.2.18 Hexagonal crystal structure of MgB_2. The arrows indicate the B-phonon mode which presumably introduces the strongest SC coupling.

known since the early 1950s and had simply been missed in the systematic research for superconductivity [137]. Since no atomic d- or f-shells are involved in the conduction electron system of this binary compound of light elements Coulomb correlation do not play a role. The simple crystal structure consisting of graphite-like B-layers with intercalated Mg favors conduction along these layers and a respective superconductive and normal state anisotropy, but it does not introduce a reduction of the effective dimensionality, as in the case of organic superconductors due to the stacking of isolated aromatic rings. The coupling of the conduction electrons to a particular boron phonon mode (see Figure 1.1.2.18) was identified right from the start as basic origin of superconductivity in MgB_2 [138]. The observation of two energy gaps (at 1.8 and 6.8 meV [139, 140]) and the considerable superconductive anisotropy as large as 6–9 [141] challenged a more thorough theoretical investigation which explained these findings in terms of two-band superconductivity [30] on the basis of the large anharmonicity of the involved phonon mode and a refined treatment of its coupling with the different sheets of the electronic conduction band [139, 142].

References

1. (a) Buckel, W. and Kleiner, R. (2013) *Supraleitung – Grundlagen und Anwendungen*, Wiley-VCH Verlag GmbH, Weinheim; (b) Buckel, W. and Kleiner, R. (2004) *Superconductivity – Fundamentals and Applications*, Wiley-VCH Verlag GmbH, Weinheim.
2. Goodstein, D. and Goodstein, J. (2000) *Phys. Perspect.*, **2**, 30.
3. Huebener, R. and Lübbig, H. (2011) *Die Physikalisch-Technische Reichsanstalt*, Vieweg+Teubner-Verlag, Wiesbaden.
4. (a) Fossheim, K. and Sudbo, A. (2004) *Superconductivity – Physics and Applications*, John Wiley & Sons, Ltd; (b) van Aubel, E., de Haas, W. J., and Voogd, J. (1928) *Comm. Leiden*, Nr 193c.
5. (a) Geballe, T.H. (2001) *Science*, **293**, 223; (b) Buzea, C. and Yamashita, T. (2001) *Supercond. Sci. Technol.*, **14**, R115.
6. Ekimov, E.A. *et al.* (2004) *Nature*, **428**, 542.
7. Mazin, I.I. (2010) *Nature*, **464**, 183.
8. Bardeen, J., Cooper, L.N., and Schrieffer, J.R. (1957) *Phys. Rev.*, **108**, 1175.

9. Cooper, L.N. and Feldman, D. (eds) (2011) *BCS: 50 Years*, World Scientific Press, Singapore.
10. Steglich, F. *et al.* (1979) *Phys. Rev. Lett.*, **43**, 1892.
11. Pfleiderer, C. (2009) *Rev. Mod. Phys.*, **81**, 1551.
12. Little, W.A. (1964) *Phys. Rev. A*, **134**, 1416.
13. Jérome, D., Mazaud, A., Ribault, M., and Bechgaard, K. (1980) *J. Phys. Lett. (Paris)*, **41**, L95.
14. Saito, G. *et al.* (1991) *Physica B*, **169**, 372.
15. Wosnitza, J. (2012) *Crystals*, **2**, 248.
16. Mermin, N.D. and Wagner, H. (1966) *Phys. Rev. Lett.*, **17**, 1133 and 1307.
17. Bednorz, J.G. and Müller, K.A. (1986) *Z. Phys. B*, **64**, 189.
18. Chu, C.W. (2011) in *BCS: 50 Years* (eds L.N. Cooper and D. Feldman), World Scientific Press, Singapore.
19. (a) Schrieffer, J.R., Scalapino, D.J., and Wilkins, J.W. (1963) *Phys. Rev. Lett.*, **10**, 336; (b) Eliashberg, G.M. (1960) *Sov. Phys. JETP*, **11**, 696.
20. Putilin, S.N. *et al.* (2001) *Physica C*, **338**, 52.
21. Gavaler, J.R. (1973) *Appl. Phys. Lett.*, **23**, 480.
22. McMillan, W.L. and Rowell, J.M. (1965) *Phys. Rev. Lett.*, **14**, 108.
23. Zeyer, R. and Zwicknagl, G. (1990) *Z. Phys. B*, **78**, 175.
24. Lee, P.A., Nagaosa, N., and Wen, X.-G. (2006) *Rev. Mod. Phys.*, **78**, 17.
25. Maier, T.A., Poilblanc, D., and Scalapino, D.J. (2008) *Phys. Rev. Lett.*, **100**, 237001.
26. Tanigaki, K. *et al.* (1991) *Nature*, **352**, 222.
27. Gunnarsson, O. (1997) *Rev. Mod. Phys.*, **69**, 575.
28. Canfield, P.C., Gammel, P.L., and Bishop, D.J. (1998) *Phys. Today*, **51**, 40.
29. Nagamatsu, J. *et al.* (2001) *Nature*, **410**, 63.
30. (a) Suhl, H., Matthias, B.T., and Walker, L.R. (1959) *Phys. Rev. Lett.*, **3**, 552; (b) Moskalenko, V. (1959) *Fiz. Met. Metalloved.*, **8**, 503; (c) Binnig, G., Baratoff, A., Hoenig, H.E., and Bednorz, J.G. (1980) *Phys. Rev. Lett.*, **45**, 1352.
31. Geerk, J. *et al.* (2005) *Phys. Rev. Lett.*, **94**, 227005.
32. Stewart, G.R. (2011) *Rev. Mod. Phys.*, **83**, 1589.
33. Hirschfeld, P., Korshunov, M.M., and Mazin, I.I. (2011) *Rep. Prog. Phys.*, **74**, 124508.
34. Kamihara, Y., Watanabe, T., Hirano, M., and Hosono, H. (2008) *J. Am. Chem. Soc.*, **130**, 3296.
35. Ren, Z.-A. *et al.* (2008) *Europhys. Lett.*, **83**, 17002.
36. R. Hott & T. Wolf, Cuprate high temperature superconductors. *Applied Superconductivity. Handbook on Devices and Applications* (ed. P. Seidel), Wiley-VCH Verlag GmbH, Weinheim (2015).
37. Yamauchi, H. and Karppinen, M. (2000) *Supercond. Sci. Technol.*, **13**, R33.
38. Wu, M.K. *et al.* (1987) *Phys. Rev. Lett.*, **58**, 908.
39. Harshman, D.R. and Mills, A.P. Jr., (1992) *Phys. Rev. B*, **45**, 10684.
40. Orenstein, J. and Millis, A.J. (2000) *Science*, **288**, 468.
41. Onose, Y., Taguchi, Y., Ishizaka, K., and Tokura, Y. (2001) *Phys. Rev. Lett.*, **87**, 217001.
42. Ando, Y. *et al.* (2001) *Phys. Rev. Lett.*, **87**, 017001.
43. (a) Tallon, J.L. and Loram, J.W. (2001) *Physica C*, **349**, 53; (b) Varma, C.M. (1997) *Phys. Rev. B*, **55**, 14554; (c) Alff, L. *et al.* (2003) *Nature*, **422**, 698.
44. Anderson, P.W. (1987) *Science*, **235**, 1196.
45. Brandt, E.H. (2001) *Phys. Rev. B*, **64**, 024505.
46. (a) Grasso, G. and Flükiger, R. (1997) *Supercond. Sci. Technol.*, **10**, 223; (b) Sato, J. *et al.* (2001) *Physica C*, **357-360**, 1111; (c) Okada, M. (2000) *Supercond. Sci. Technol.*, **13**, 29.
47. Saxena, A.K. (2010, 2012) *High-Temperature Superconductors*, Springer-Verlag, Berlin, Heidelberg.
48. Plakida, N.P. (1995) *High-Temperature Superconductivity*, Springer-Verlag, Berlin, Heidelberg.
49. Larbalestier, D., Gurevich, A., Feldmann, D.M., and Polyanskii, A. (2001) *Nature*, **414**, 368.
50. (a) Hilgenkamp, H. and Mannhart, J. (2002) *Rev. Mod. Phys.*, **74**, 485; (b)

Gross, R. *et al.* (1997) *IEEE Trans. Appl. Supercond.*, **7**, 2929.
51. Kleiner, R., Steinmeyer, F., Kunkel, G., and Müller, P. (1992) *Phys. Rev. Lett.*, **68**, 2394.
52. Brandt, E.H. (1995) *Rep. Prog. Phys.*, **58**, 1465.
53. (a) Tsuei, C.C. and Kirtley, J.R. (2000) *Rev. Mod. Phys.*, **72**, 969; (b) Tsuei, C.C. and Kirtley, J.R. (2002) *Physica C*, **367**, 1.
54. Graser, S. *et al.* (2010) *Nat. Phys.*, **6**, 609.
55. (a) Sleight, A.W., Gillson, J.L., and Bierstedt, P.E. (1975) *Solid State Commun.*, **17**, 27; (b) Merz, M. *et al.* (2005) *Europhys. Lett.*, **72**, 275.
56. Mattheiss, L.F., Gyorgy, E.M., and Johnson, D.W. Jr., (1988) *Phys. Rev. B*, **37**, 3745.
57. Hellman, E.S. and Hartford, E.H. Jr., (1995) *Phys. Rev. B*, **52**, 6822.
58. (a) Cava, R.J. *et al.* (1988) *Nature*, **332**, 814; (b) Pei, S. *et al.* (1990) *Phys. Rev. B*, **41**, 4126; (c) Klinkova, L.A. *et al.* (2003) *Phys. Rev. B*, **67**, 140501.
59. Maeno, Y., Rice, T.M., and Sigrist, M. (2001) *Phys. Today*, **54**, 42.
60. Bernhard, C. *et al.* (1999) *Phys. Rev. B*, **59**, 14099.
61. Nachtrab, T. *et al.* (2004) *Phys. Rev. Lett.*, **92**, 117001.
62. Takada, K. *et al.* (2003) *Nature*, **422**, 53.
63. Foo, M.L. *et al.* (2003) *Solid State Commun.*, **127**, 33.
64. (a) Yonezawa, S. *et al.* (2004) *J. Phys. Condens. Matter*, **16**, L9; (b) Yonezawa, S., Muraoka, Z., and Hiroi, Z. (2004) *J. Phys. Soc. Jpn.*, **73**, 1655; (c) Yonezawa, S., Muraoka, Y., Matsushita, Y., and Hiroi, Z. (2004) *J. Phys. Soc. Jpn.*, **73**, 819; (d) Hiroi, Z., Yonezawa, S., and Muraoka, Y. (2005) *J. Phys. Soc. Jpn.*, **74**, 3399.
65. Ong, N.P. and Cava, R.J. (2004) *Science*, **305**, 52.
66. Schuck, G. *et al.* (2006) *Phys. Rev. B*, **73**, 144506.
67. Kunes, J., Jeong, T., and Pickett, W.E. (2004) *Phys. Rev. B*, **70**, 174510.
68. Nagao, Y. *et al.* (2009) *J. Phys. Soc. Jpn.*, **78**, 064702.
69. Hattori, K. and Tsunetsugu, H. (2010) *Phys. Rev. B*, **81**, 134503.
70. Hiroi, Z., Yamaura, J., Yonezawa, S., and Harima, H. (2007) *Physica C*, **460-462**, 20.
71. Sainz, R. and Freeman, A.J. (2005) *Phys. Rev. B*, **72**, 024522.
72. Mansky, P.A., Danner, G., and Chaikin, P.M. (1995) *Phys. Rev. B*, **52**, 7554.
73. (a) Johnston, D.C. (2010) *Adv. Phys.*, **59**, 803; (b) Mandrus, D., Sefat, A.S., McGuire, M.A., and Sales, B.C. (2010) *Chem. Mater.*, **22**, 715.
74. Chmaissem, O. *et al.* (1999) *Nature*, **397**, 45.
75. Lee, C.-H. *et al.* (2008) *J. Phys. Soc. Jpn.*, **77**, 083704.
76. (a) Hardy, F. *et al.* (2010) *Europhys. Lett.*, **91**, 47008; (b) Sefat, A.S. *et al.* (2008) *Phys. Rev. Lett.*, **101**, 117004.
77. Lanata, N. *et al.* (2013) *Phys. Rev. B*, **87**, 045122.
78. Prozorov, R. and Kogan, V.G. (2011) *Rep. Prog. Phys.*, **74**, 124505.
79. Putti, M. *et al.* (2010) *Supercond. Sci. Technol.*, **23**, 034003.
80. Katase, T. *et al.* (2011) *Nat. Commun.*, **1419** (2), 409.
81. Lee, S. *et al.* (2009) *Appl. Phys. Lett.*, **95**, 212505.
82. Fulde, P., Keller, J., and Zwicknagl, G. (1988) *Solid State Physics, Advances in Research and Applications*, Vol. 41, Academic Press, p. 1.
83. Thalmeier, P. and Zwicknagl, G. (2004) *Handbook on the Physics and Chemistry of Rare Earths*, Vol. 34, Elsevier; cond-mat/0312540.
84. Sarrao, J.L. *et al.* (2002) *Nature*, **420**, 297.
85. Fulde, P., Thalmeier, P., and Zwicknagl, G. (2006) *Solid State Physics, Advances in Research and Applications*, Vol. 60, Academic Press, p. 1.
86. Zwicknagl, G. (1992) *Adv. Phys.*, **41**, 203.
87. Ernst, S. *et al.* (2011) *Nature*, **474**, 362.
88. (a) Zwicknagl, G., Yaresko, A.N., and Fulde, P. (2002) *Phys. Rev. B*, **63**, 081103; (b) Zwicknagl, G., Yaresko, A.N., and Fulde, P. (2003) *Phys. Rev. B*, **68**, 052508.
89. Zwicknagl, G., Thalmeier, P., and Fulde, P. (2009) *Phys. Rev. B*, **79**, 115132.

90. (a) Thompson, J.D. *et al.* (2001) *J. Magn. Magn. Mater.*, **226-230**, 5; (b) Petrovic, C. *et al.* (2001) *Europhys. Lett.*, **53**, 354.
91. Petrovic, C. *et al.* (2001) *J. Phys. Condens. Matter*, **13**, L337.
92. Bauer, E. *et al.* (2004) *Phys. Rev. Lett.*, **92**, 027003.
93. Kimura, N. and Bonalde, I. (2012) in *Non-Centrosymmetric Superconductors*, Lecture Notes in Physics, Vol. 84, Chapter 2 (eds E. Bauer and M. Sigrist), Springer, Heidelberg, pp. 35–79.
94. Nakatsuji, S. *et al.* (2008) *Nat. Phys.*, **4**, 603.
95. Shishido, H. *et al.* (2010) *Science*, **327**, 980.
96. Stewart, G.R., Fisk, Z., Willis, J.O., and Smith, J.L. (1984) *Phys. Rev. Lett.*, **52**, 679.
97. Geibel, C. *et al.* (1991) *Z. Phys. B*, **84**, 1.
98. Geibel, C. *et al.* (1991) *Z. Phys. B*, **83**, 305.
99. Palstra, T.T.M. *et al.* (1985) *Phys. Rev. Lett.*, **55**, 2727.
100. (a) Schmidt, A.R. *et al.* (2010) *Nature*, **465**, 570; (b) Aynajian, P. *et al.* (2010) *Proc. Natl. Acad. Sci. U.S.A.*, **107**, 10383; (c) Yuan, T., Figgins, J., and Morr, D.K. (2012) *Phys. Rev. B*, **86**, 035129; (d) Shibauchi, T. and Matsuda, Y. (2012) *Physica C*, **481**, 229; (e) Das, T. (2012) *Sci. Rep.*, **2**, 596; (f) Pourret, A. *et al.* (2013) *J. Phys. Soc. Jpn.*, **82**, 034706.
101. Ott, H.R., Rudigier, H., Fisk, Z., and Smith, J.L. (1983) *Phys. Rev. Lett.*, **80**, 1595.
102. Saxena, S.S. *et al.* (2000) *Nature*, **406**, 587.
103. Ginzburg, V. (1957) *JETP*, **4**, 153.
104. Wastin, F. *et al.* (2003) *J. Phys. Condens. Matter*, **15**, S2279.
105. Aoki, D. *et al.* (2007) *J. Phys. Soc. Jpn.*, **76**, 063701.
106. Bauer, E.D. *et al.* (2002) *Phys. Rev. B*, **65**, 100506.
107. Izawa, K. *et al.* (2003) *Phys. Rev. Lett.*, **90**, 117001.
108. Meissner, W. and Franz, H. (1930) *Z. Phys.*, **65**, 30.
109. Mourachkine, A. (2004) *Room-Temperature Superconductivity*, Cambridge International Science Publishing, Cambridge.
110. Matthias, B.T. and Hulm, J.K. (1952) *Phys. Rev.*, **87**, 799.
111. Bechgaard, K. *et al.* (1981) *Phys. Rev. Lett.*, **46**, 852.
112. Lee, I.J. *et al.* (2002) *Phys. Rev. Lett.*, **88**, 017004.
113. (a) Zwicknagl, G. and Wosnitza, J. (2011) in *BCS: 50 Years* (eds L.N. Cooper and D. Feldman), World Scientific Press, Singapore; (b) Casalbuoni, R. and Nardulli, G. (2004) *Rev. Mod. Phys.*, **76**, 263; (c) Beyer, R. and Wosnitza, J. (2013) *Low Temp. Phys.*, **39**, 225.
114. Lortz, R. *et al.* (2007) *Phys. Rev. Lett.*, **99**, 187002.
115. Beyer, R. *et al.* (2012) *Phys. Rev. Lett.*, **109**, 027003.
116. (a) Cava, R.J. *et al.* (1994) *Nature*, **367**, 252; (b) Cava, R.J. *et al.* (1994) *Nature*, **367**, 146.
117. Takano, Y. (2006) *Sci. Technol. Adv. Mater.*, **7**, S1.
118. (a) Amano, G. *et al.* (2004) *J. Phys. Soc. Jpn.*, **73**, 530; (b) Nakane, T. *et al.* (2004) *Appl. Phys. Lett.*, **84**, 2859; (c) Kim, J.S. *et al.* (2007) *Phys. Rev. B*, **76**, 014516.
119. Hannay, N.B. *et al.* (1965) *Phys. Rev. Lett.*, **14**, 225.
120. Koike, Y., Tanuma, S., Suematsu, H., and Higuchi, K. (1980) *J. Phys. Chem. Solids*, **41**, 1111.
121. Pendrys, L.A. *et al.* (1981) *Solid State Commun.*, **38**, 677.
122. Wachnik, R.A. *et al.* (1982) *Solid State Commun.*, **43**, 5.
123. Emery, N. *et al.* (2008) *Sci. Technol. Adv. Mater.*, **9**, 44102.
124. (a) Weller, T.E. *et al.* (2005) *Nat. Phys.*, **1**, 39; (b) Emery, N. *et al.* (2005) *Phys. Rev. Lett.*, **95**, 087003.
125. Emery, N. *et al.* (2006) *J. Solid State Chem.*, **179**, 1289.
126. (a) Hebard, A. *et al.* (1991) *Nature*, **350**, 600; (b) Fleming, R.M. *et al.* (1991) *Nature*, **352**, 787.
127. (a) Pennington, C.H. and Stenger, V.A. (1996) *Rev. Mod. Phys.*, **68**, 855; (b) Buntar, V. and Weber, H.W. (1996) *Supercond. Sci. Technol.*, **9**, 599.
128. Takabayashi, Y. *et al.* (2009) *Science*, **323**, 1585.

129. Mitsuhashi, R. *et al.* (2010) *Nature*, **464**, 76.

130. Xue, M. *et al.* (2012) *Sci. Rep.*, **2**, 389.

131. (a) Tang, Z.K. *et al.* (2001) *Science*, **292**, 2462; (b) Bockrath, M. (2006) *Nat. Phys.*, **2**, 155.

132. Shi, W. *et al.* (2012) *Sci. Rep.*, **2**, 625.

133. Izawa, K. *et al.* (2002) *Phys. Rev. Lett.*, **89**, 137006.

134. Nagarajan, R. *et al.* (1994) *Phys. Rev. Lett.*, **72**, 274.

135. Hilscher, G. and Michor, H. (1999) *Studies in High Temperature Superconductors*, Vol. 28, Nova Science Publishers, pp. 241–286.

136. Müller, K.-H. and Narozhnyi, V.N. (2001) *Rep. Prog. Phys.*, **64**, 943.

137. (a) Grant, P. (2001) *Nature*, **411**, 532; (b) Campbell, A.M. (2001) *Science*, **292**, 65.

138. (a) Kortus, J. *et al.* (2001) *Phys. Rev. Lett.*, **86**, 4656; (b) Bohnen, K.-P., Heid, R., and Renker, B. (2001) *Phys. Rev. Lett.*, **86**, 5771.

139. Choi, H.J., Roundy, D., Sun, H., Cohen, M.L., and Louie, S.G. (2002) *Nature*, **418**, 758.

140. Canfield, P.C. and Crabtree, G. (2003) *Phys. Today*, **56**, 34.

141. Bud'ko, S.L., Canfield, P.C., and Kogan, V.G. (2002) *Physica C*, **382**, 85.

142. (a) Kong, Y., Dolgov, O.V., Jepsen, O., and Andersen, O.K. (2001) *Phys. Rev. B*, **64**, 020501; (b) Mazin, I.I. *et al.* (2004) *Phys. Rev. B*, **69**, 056501; (c) Choi, H.J. *et al.* (2004) *Phys. Rev. B*, **69**, 056502.

1.2
Main Related Effects

1.2.1
Proximity Effect
Mikhail Belogolovskii

1.2.1.1 Introduction

The proximity effect (hereafter as PE) manifests itself as a mutual induction of physical properties from one material into an adjacent one across their interface. This definition means that the structure studied consists, at least, of three main elements: two materials with distinct characteristics and the interface whose transparency determines an effectiveness of the discussed phenomenon. In the most known N/S (normal/superconductor) example, due to the adjacent superconductor (S), electron pairs permeate into the neighboring normal (N) metal and, conversely, through the N/S interface, normal electrons leak into the superconductor partly destroying superconducting correlations in the S-side of the bilayer ([1]; Chapter 6).

Two prototypical examples of the N/S sandwich, namely, that with a low transparent interface (the so-called tunneling limit) as well as a direct NS contact, were studied, for the first time, in two seminal papers by McMillan published in 1968 [2, 3]. Taking into account incoherent single-particle scatterings from one layer to another treated within the tunnel-barrier approximation, he succeeded to explain such proximity-induced features as the enhancement of the Bardeen–Cooper–Schrieffer (BCS) potential in the N film, induced mini-gap Ω_N, qualitative changes of electronic densities of states in the adjacent metals, and so on [2]. The tunneling PE model was widely used to explain experimental data, for example, those for Nb/Pb sandwiches [4]. Note that the barrier in this model need not to be directly related to an insulating layer since reflection of quasiparticle states can be associated, for example, with different electronic structures of two metals in contact. In the second paper by McMillan [3], the analysis was based on a specific elastic phase-coherent transfer process across the NS interface by which normal current is converted into a super-current (in particular, at energies below the superconducting energy gap Δ_S, when direct single particle transmissions are forbidden). It is known as the *Andreev scattering*: an electron (hole) incident on the interface from the N side is elastically retroreflected into a hole (electron) from a spin-reversed band which is traveling in the opposite direction to the incoming charge. Starting from a step-like BCS pairing potential, McMillan [3] recalculated it and found that the new potential, which is nearly self-consistent, is roughly half Δ_S at the interface, very quickly (exponentially) approaches the bulk value of the energy gap Δ_S into the S-side, and drops rapidly into the N-side.

Generally, an advanced PE theory should be based on the microscopic Gor'kov equations and on a realistic treatment of the N/S interface. But even the oversimplified McMillan's models, which took into account two different aspects of the very complicated problem, are able to provide deep insight into the underlying

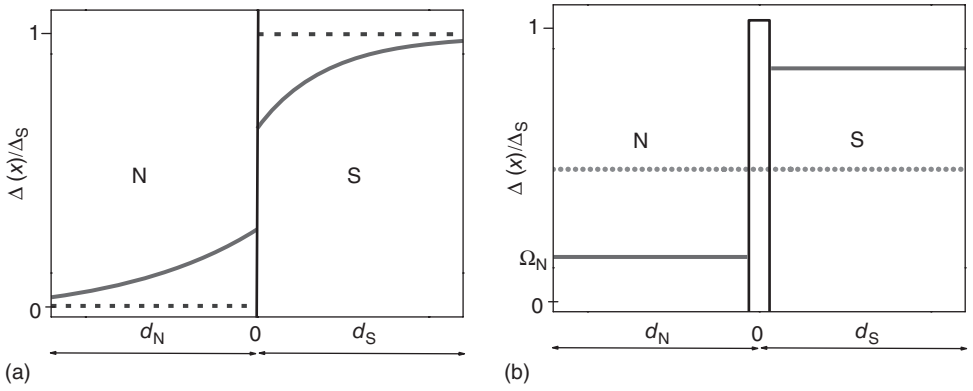

Figure 1.2.1.1 Sketch of the spatial dependence of the energy gap value (solid lines) in a proximity N/S sandwich with comparatively thick (a) and very thin (b) N (with a weak attractive electron–electron interaction) and S layers; Δ_S is the BCS potential in an isolated S metal, d_N and d_S are thicknesses of N and S layers, respectively. In (a), the dashed line demonstrates a step-like approximation for the BCS pairing potential. In (b), N and S films are separated by a potential barrier; if its height is comparatively low, we get a so-called Cooper limit shown with a dotted line.

physics and to explain, at least, qualitatively the main part of experimental data. According to them, principal spatial behavior of the order parameter $\Delta(x)$ in a planar N/S sandwich for extremely thick and extremely thin proximity-coupled S and N layers has the form shown in Figure 1.2.1.1a,b, respectively. The extent of superconducting correlations in the N part of the bilayer is determined by its structure and geometry: in a thin N layer, the proximity-induced mini-gap Ω_N is uniform, whereas in a thick N film the correlations extend over some distance determined by the energy of the electrons E relative to the Fermi level E_F. One of the signatures of the PE is the modification of local electronic densities of states $N(\varepsilon)$ in N and S parts, $\varepsilon = E - E_F$. The case of very thin N and S layers with one single gap Ω_N, two different peaks corresponding to Ω_N, and a new (corrected) value of the gap in a superconductor is shown in Figure 1.2.1.2.

Although the main conclusions of the McMillan's papers remain valid to date, see reviews by Gilabert [5], Pannetier and Courtois [6], and Klapwijk [7], a substantial body of novel results and new developments has contributed to the present level of PE understanding. One of the main advances of the last two decades has been a comprehension idea about the key role of the Andreev reflection in the PE. Other novel aspects of the problem relate new nonsuperconducting and superconducting materials which were unknown or unused in previous experiments with proximized bilayers, an effect of the interface between superconducting and nonsuperconducting films, which in some cases is not limited to the penetrability of superconducting correlations but can be a source of unexpected interfacial phenomena, and so on.

In the following, we attempt to present a simple introduction into the PE with the aim to explain fundamentals of the phenomenon and at the same time to

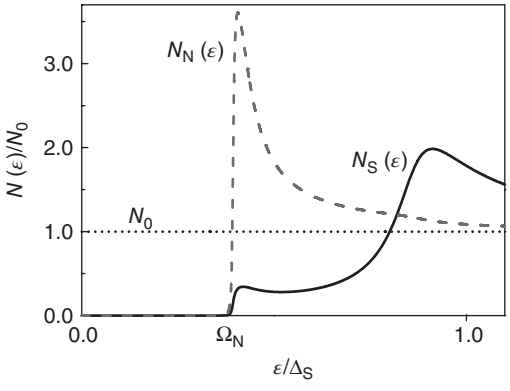

Figure 1.2.1.2 Sketch of normalized electronic densities of states versus energy on the normal $N_N(\varepsilon)$ and superconductor $N_S(\varepsilon)$ sides of an S/N sandwich; N_0 = const is the normal-state density of states of the sample, Δ_S is the BCS potential in an isolated S metal, and Ω_N is the minigap induced in the proximized N layer.

deliver current understanding of the general physical picture to a reader. In contrast to previous PE reviews, where the main attention was paid to basic effects in N/S sandwiches, we discuss all types of superconducting hybrid structures, composed from constituents of fundamentally different electronic structures, and present some novel devices and experiments in order to show PE perspectives for practical applications. The ideas underlying the two McMillan's papers will form a basis for our discussion.

The overview is structured as follows. In order to put the superconducting proximity phenomenon into a broader context, we commence with a simplest version of the PE by considering a relatively trivial case of a metal–insulator (MI) contact. In spite of diverse nature and very different values of superconducting and dielectric gaps, we demonstrate a few similar features exhibited by MI and NS sandwiches. A summary of the works on N/S bilayers, the most often studied PE samples, is presented in the next section. Then we deal with a specific PE arising between a ferromagnetic (F) metal and a superconductor in contact, explain the origin of the singlet-triplet conversion and the long-range PE in F/S hybrid bilayers. We finish the chapter by reviewing last ideas concerning the discussed phenomenon, in particular those relating contacts of superconductors with PE-affected topological insulators, a new class of quantum materials which, due to time-reversal symmetry, relativistic effects, and the inverted band structure, are insulating in bulk and completely metallic with a Dirac-like spectrum at their surface.

1.2.1.2 Metal–Insulator Contact

In order to be able to gain an insight into the main ideas of superconducting PEs, we start with a more simple system made of a metal and an insulator in contact. Owing to the wave nature of an electron, there is a finite probability to

find the charge in a classically forbidden region adjacent to a metal film. It is well known that the probability exponentially decays into the insulating film and, when the film thickness is nanoscale, an electron can be found at the outer side of the potential barrier. The quantum-mechanical tunneling phenomenon in solid-state systems realized by separating two conductors with a very thin insulator is known from 1950s and now constitutes a basis upon which such devices as Josephson junctions, scanning tunneling microscope, and others are operating.

Less known is that fits of the rectangular barrier model to experimental data often lead to unphysically small values of extracted parameters, especially, barrier heights [8]. The origin of the discrepancy can be, in particular, related to the presence of a high density of extra metal-induced states in the gap energy range [9]. What is important for superconductor–insulator interfaces is that, according to Choi *et al.* [10], these states are strongly localized at the MI interface by inevitably random fluctuations in the electronic potential and so can produce paramagnetic spins. It can explain the origin of magnetic flux noise in superconducting quantum interference devices (SQUIDs) with a power spectrum $\sim 1/f$ (f is the frequency) which limits the decoherence time of superconducting flux-sensitive qubits [10]. Spin-flip scattering of conduction electrons by local magnetic moments, possibly located at metal–oxide interfaces, was revealed in granular Al films in the vicinity of the metal-to-insulator transition [11]. The most surprising finding was the coexistence of enhanced superconducting properties in Al granules with surface magnetic moments which raises a question about the mechanism of superconductivity in such films.

Notice that electrons trapped into the localized states in the near-surface region in an insulator can tunnel into the adjacent metal when an electric field is applied to the interface (in a superconductor it occurs only when the energy gained by an electron is larger than the energy gap). Such a model was proposed by Halbritter [12] to explain loss mechanisms in superconducting niobium cavities. Usually, this effect is negligible but in the case of Nb it can be important due to the presence of conducting Nb oxides. When the radio frequency (RF) field in the cavities is raised, a longitudinal electric field penetrates the insulator and stimulates electrons to tunnel to the superconductor and to return back when the field is lowered. The losses due to interface tunnel exchange are an example of the interface-induced effect which should be more pronounced in the case of small grain sizes.

Let us now look at the NI proximity problem from a perspective of elastic scattering processes at the interface (see Figure 1.2.1.3a). An electron (hole) incident on the interface from the N side is retroreflected into an electron (hole) of the same energy E and the same absolute value of momentum but traveling in the opposite direction to the incoming charge. Let us consider an ideal three-dimensional planar structure with two normal metallic electrodes, two insulating layers I which are so thick that electrons can tunnel across them very rarely, and a normal-metal nanometer-thin N′ interlayer of the thickness d_N. In the NIN′IN structure, an electron is spatially confined in the direction x normal to the layers but remains free to move in the parallel direction. It results in the creation of a two-dimensional electron gas at quasi-bound quantized electron states.

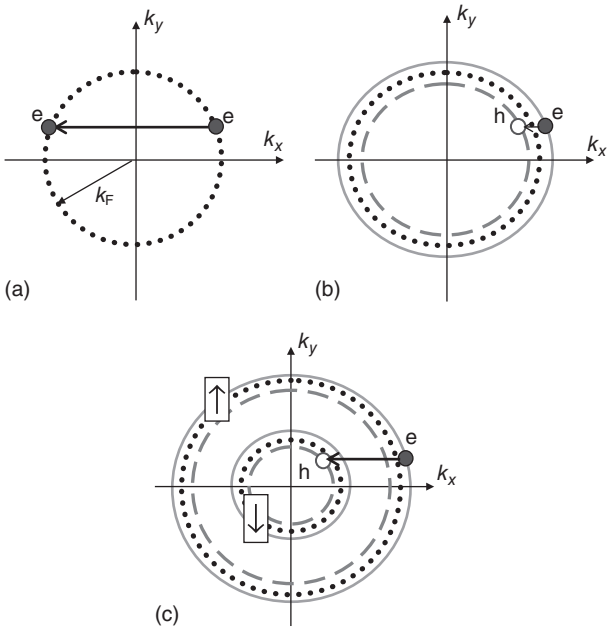

Figure 1.2.1.3 Scattering processes at NI (a), NS (b), and FS (c) interfaces. The filled and empty circles denote the quasielectron (e) and quasihole (h) states in the nonsuperconducting layer. The Fermi surface with the Fermi wave vector k_F, the constant-energy electron surface, and the constant-energy hole surface are shown with dotted, solid, and dashed lines, respectively; arrows in the (c) panel denote the spin direction of the corresponding energy band.

The electron transmission coefficient (transparency) D through the NIN′IN structure is sharply peaked about certain energies corresponding to virtual resonant levels in the quantum well of the thickness d_N. The energies can be easily found from the demand of coherent superposition of scattered electron waves. According to the Bohr–Sommerfeld quantization rule, the electron wave-function phase shift acquired during the electron "round-trip" inside the N′ interlayer (shown in Figure 1.2.1.4a) $2k_x d_N = 2\pi j$, where k_x is the x-component of the electron wave vector, j is integer. When two insulating I layers are atomically thin and identical, an electron with one of the resonant energies can cross the NIN′IN system without being reflected (the resonant tunneling effect). Although the latter phenomenon is well known from elementary quantum mechanics, we want to stress that the peaked structure appears just due to the presence of insulating layers adjacent to the N′ interlayer and that energy locations of strong maxima and minima in its spectrum can be obtained by very simple quantum-phase arguments which will be applied further to NS and FS cases. The second remark concerns a strong effect of barrier inhomogeneities on electron tunneling near resonance energies (see [13] and references therein).

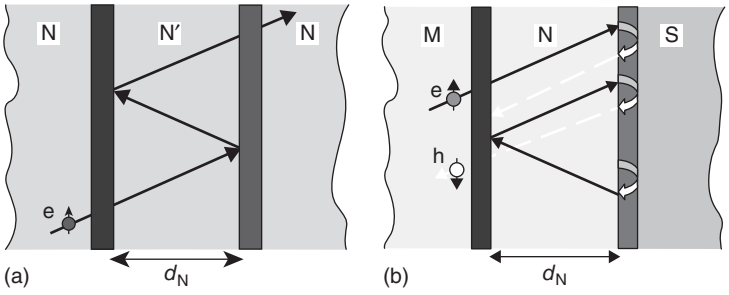

Figure 1.2.1.4 Backscattering processes within a normal interlayer are decomposed into a series of alternating reflections from tunneling barriers in a double-barrier NIN′IN structure (a) and those by the superconducting pair potential and a barrier potential in an MIN′IS junction (b).

Resuming this subsection, we would like to attract the attention to three different aspects of the NI PE which are common for the cases discussed below as well: (i) leakage of itinerant electrons from a metal into an insulator, (ii) existence of energy regions with a strongly suppressed density of states in the excitation spectrum of a spatially confined N′ interlayer due to backscattering of electron waves from the N′I interface, and (iii) specific properties of the MI interface which appears only when the surfaces of the two separated materials are brought into a contact. Generally, the three features are only different manifestations of the same phenomenon and, in principle, should be described self-consistently within a unified formalism for the inhomogeneous solid-state structures. Keeping in mind the analogy (and the difference as well) between I and S layers, we can now transfer to the superconducting PE.

1.2.1.3 Normal Metal–Superconductor Contact

Even the simplest hybrid NS heterostructure with an ideal interface reveals several interesting phenomena. The energy scale in the NS bilayer is characterized by a superconducting gap energy of the order of 1 meV, which is much less than a N-metal electron band width (∼1 eV and more). That is why the probability of the normal backscattering from a clean NS interface is extremely small and a quasiclassical approximation, see the review in [14], applied to the Green-function formalism serves usually as a starting point for theoretical works dealing with a quasi-ballistic NS problem when elastic quasielectron-into-quasihole transformations of Bogoliubov quasiparticles and inverse (with a missing charge of $2e$ absorbed into the superconducting ground state as a Cooper pair) occur at the NS interface – see Figure 1.2.1.3b. At voltage bias $V = 0$, the differential conductance $G(V) = dI(V)/dV$ of an ideal NS bilayer is determined only by pair transferring processes and is as large as twice normal-state conductance, whereas in the very low transparency limit $G(0)$ of the N/S contact is vanishing at $T = 0$. The current across the junction with N and S layers divided by an insulating barrier does not increase until the electron volt reaches the superconducting gap Δ_S [15]. At $\overline{V} = \Delta_S/e$, the differential conductance $G(V)$ of the trilayer exhibits a peak.

Proximity-induced changes in the electronic density of states $N_N(\varepsilon)$ of a normal metal are directly reflected in the $G(V)$ characteristic of a planar tunnel junction formed by a normal counter-electrode M, an isolator I, and the NS contact. Thus, the tunneling experiment (real or imagined) can serve as a probe of the local electronic density of states at the tunneling surface weighted by the angular distribution of tunneling electrons [3]. Considering MINS junction within the Bohr – Sommerfeld quantization condition, we can easily understand the origin of the coherent peak in the spectrum of a superconductor and its modification for the N layer of the thickness $d_{N'}$. The characteristic energy $\overline{E}$ of a bound state formed in the N interlayer corresponds to the coherent superposition of reflected quasiparticle waves. To find it, we suppose a planar geometry of the MINS structure (Figure 1.2.1.4b) where the trajectories of quasiparticles in the electron branch and those in the hole branch are denoted by solid and dashed lines, respectively. A charge velocity component perpendicular to the layers changes its sign in the normal reflection from the MI interface, whereas all velocity components change their signs in the Andreev backscattering from the NS interface. The reflection coefficients can be calculated from the boundary conditions of the wave functions using the fact that in the discussed geometry transverse components of the wave vectors are unchanged. In this case, each Andreev reflection within the energy gap contributes an additional phase shift $\chi^{eh(he)}(\boldsymbol{k}) = -\arccos(\varepsilon/|\Delta(\boldsymbol{k})|) \mp i\Phi(\boldsymbol{k})$, where $|\Delta(\boldsymbol{k})|$ and $\Phi(\boldsymbol{k})$ are absolute value and phase of the complex superconducting order parameter (see, e.g., [16]). Adding the phases accumulated along an electron "round-trip" in the N interlayer with two subsequent Andreev reflections (Figure 1.2.1.4b), for an s-wave superconducting electrode, we get the following expression for the phase shift: $k_x^e d_n + \chi^{eh} - k_x^h d_n + \pi - k_x^h d_n + \chi^{he} + k_x^e d_n + \pi = (4\varepsilon/\hbar v_F)(d_N/\cos\theta) - 2\arccos(\varepsilon/\Delta_S)$, where θ is the incident angle, the x-axis is normal to interfaces. The bound-state energies $\overline{\varepsilon} = \overline{E} - E_F$ can be found requiring the total phase shift to be an integer multiple of 2π. Hence, the lowest bound level follows from the relation $\overline{\varepsilon} = \hbar v_F \arccos(\overline{\varepsilon}/\Delta_S)\cos\theta/2d_N$. For a clean system which is translationally invariant in the y and z directions, contributions from long path lengths ($\theta \to \pi/2$) result in no gap in the excitation spectrum [3]. But this conclusion is valid for infinite samples. If the volume of the N part of a mesoscopic N/S bilayer is finite, we get a sharp gap in the excitation spectrum like that in the PE tunneling model [2] or in the dirty (diffusive) limit when electrons experience a huge number of elastic scatterings on impurities during the way from one surface to another. In the latter case, the size limiting the phase coherence length for electron-like and hole-like quasiparticles traversing a diffusive trajectory is the elastic mean free path $l_e = \sqrt{D\tau_e}$, here D is the diffusion constant in the normal metal, and τ_e is the elastic scattering time. If so, then in the previous formula for $\overline{\varepsilon}$, we should replace the average time $\sim d_N/v_F$ for the motion of a quasiparticle across a clean N film with $\tau_e \sim d_N^2/D$. When $\overline{\varepsilon} \ll \Delta_S$, the minigap in a dirty N layer is thus expected to be approximately $\overline{\varepsilon} \approx \pi\hbar D/4d_N^2$ (compare with the numerically exact expression $\overline{\varepsilon} \approx 0.78\hbar D/d_N^2$ obtained in [17]).

In d-wave superconductors like YBCO, dissimilar values of $\Phi(\boldsymbol{k})$ seen by a quasiparticle moving along different scattering trajectories (Figure 1.2.1.4b)

brings to the Bohr–Sommerfeld quantization rule an additional phase shift $\delta\Phi(\boldsymbol{k})$. The most dramatic effect of $\delta\Phi(\boldsymbol{k}) = \pi$ occurs for the tunneling direction [110], converting destructive interference at $\overline{\varepsilon} = 0$ in the s-wave case into constructing interference (see, e.g., [16]). Owing to the phase conjugation between electrons and holes at the Fermi level, it survives even in the presence of a normal interlayer when tunneling across the barrier in MINS devices is specular and a strong zero-bias peak in the $G(V)$ characteristic of a MINS junction is one of the main signatures of the d-wave symmetry of the order parameter in an S electrode.

Notice that the stepwise approximation for the pair potential used above and known as a *rigid-boundary condition* for superconducting bilayers is not self-consistent. According to Likharev [18], in real N/S junctions the deviation of the self-consistent solution from the step-like function strongly decreases when the interface resistivity is much bigger than that of metal electrodes. From the Andreev-scattering view, the penetration of superconducting correlations into a normal material is limited by dephasing between electron and hole wave functions $\delta\varphi = (k_x^{\mathrm{e}} - k_x^{\mathrm{h}})l$ which grows with increasing distance l from the N/S boundary into the N-side. The relevant length scale governing superconducting correlations in a clean N-metal is given by the temperature-dependent coherence length $\xi_{\mathrm{T}} = \hbar v_{\mathrm{F}}/(2\pi k_{\mathrm{B}} T)$.

Since practically used films are usually full of different imperfections, the charge scatterings inside them render the Green function to be isotropic in space. The quasi-classical Eilenberger equations can be further simplified to the form which is more appropriate for numerical calculations and is known as *Usadel equations*, see the review in [14]. Related boundary conditions for an interface between two superconductors were derived by Kupriyanov and Lukichev [19]. The validity of Usadel equations depends on the superconductor ($l_{\mathrm{e}} \ll \xi_0$) as well as on the normal metal ($l_{\mathrm{e}} \ll d_{\mathrm{N}}, \xi_{\mathrm{T}}$), where $\xi_{\mathrm{T}} = \sqrt{\hbar D/(2\pi k_{\mathrm{B}} T)}$ is the temperature-dependent decay length in the dirty N layer. Note that the validity of the clean-limit solution is restricted to $l_{\mathrm{e}}, \xi_{\mathrm{T}} \gg d_{\mathrm{N}}$ and to $l_{\mathrm{e}} \gg d_{\mathrm{N}} \exp(2d_{\mathrm{N}}/\xi_{\mathrm{T}})$ if $\xi_{\mathrm{T}} \ll d_{\mathrm{N}}$ [20].

Specific properties of proximity-coupled NS bilayers can be useful for practical purposes since they provide an additional internal degree of freedom which can offer new abilities to design and tune such characteristics as the critical temperature, the energy gap, and the shape of corresponding temperature dependencies. The most straightforward application consists in the control over T_{c}, which is determined by PEs and can, therefore, be tuned by varying individual layer thicknesses. As an example, we consider NS sandwiches where the thicknesses d_{S} and d_{N} are somewhat larger than corresponding coherence lengths [21]. Then the bilayer critical temperature as a function of d_{N} follows an exponential law $T_{\mathrm{c}} = \widetilde{T}_{\mathrm{c}} - \mathrm{const} \cdot \exp(-\alpha d_{\mathrm{N}})$ where the decay constant α increases with the decrease of the electron mean free path in the superconductor (see the related experimental data in Figure 1.2.1.5). The possibility to tune T_{c} with a PE was realized, in particular, in bolometers [22] and superconducting screening ground planes [23]. In the first case, the absorber and the thermistor were Ti–Al–Ti trilayers with thicknesses ~50 nm chosen to achieve T_{c} of 380 mK. In order to produce superconducting screening planes with tunable T_{c}'s between 4 and 7 K,

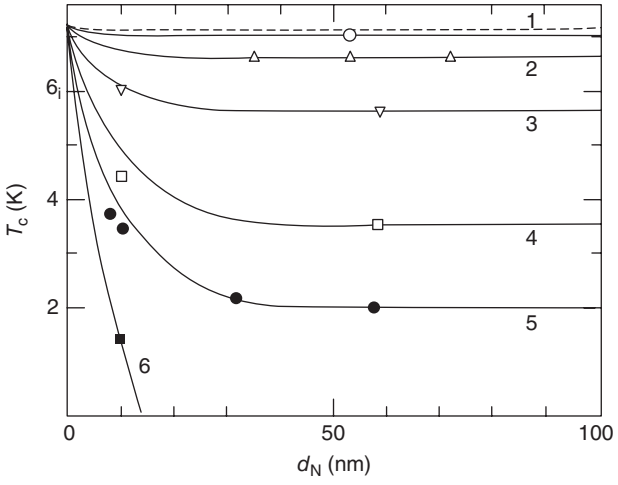

Figure 1.2.1.5 Transition temperature of Pb/Cu bilayers versus the Cu-film thickness d_N; the thickness of the Pb films was 100 nm (1), 50 nm (2), 30 nm (3), 15 nm (4), 10 nm (5), and 7 nm (6). (Adapted from [1], Figure 6.6. Reproduced with permission of John Wiley & Sons.)

Kain *et al.* [23] used Pb/Ag bilayers. In agreement with the theory, in samples with good electrical contact between two layers, the measured T_c values followed well the Cooper model of the PE when superconducting characteristics are averaged over the bilayer (see Figure 1.2.1.1b).

The main goal of the work by Lacquaniti *et al.* [24] was to design an intrinsically shunted Josephson device resistant to temperature fluctuations above 4.2 K and based on the niobium technology. A strong temperature dependence of critical current I_c in conventional Nb-based superconductor – insulator – superconductor (SIS) Josephson junctions appears when they are employed above 5 K. The problem comes from a steep-like behavior of the $I_c(T)$ curve above $T \approx 0.5T_{cs}$, where T_{cs} is the S-film critical temperature. In order to obtain more gentile curve, the authors replaced one of the superconducting electrodes with an N/S bilayer. It has been shown experimentally that with increasing temperature the superconducting order parameter in a normal layer of a thickness d_N comparable with that of the S film d_S first rapidly decreases and then at $T \approx T^*$ becomes flat up to a nearest vicinity of the bilayer T_c. Changing the ratio d_N/d_S, the authors modified the T^* value and were able to engineer thermal stability of the Josephson superconductor – normal conductor – isolator – superconductor (SNIS) devices.

1.2.1.4 Ferromagnetic Metal – Superconductor Contact

Coexistence of such antagonistic phenomena as superconductivity and ferromagnetism is a long-standing problem in solid-state physics. Originally, it was believed that they are mutually exclusive, but more recently it was found that they can coexist under certain circumstances giving rise to novel combined effects. One of the possibilities to observe the interplay between itinerant electron ferromagnetism (F) and superconductivity is to put the two metallic films into a contact. Besides a

fundamental physics interest, such bilayers hold important potential for applications in spintronics devices [25] as well as for recovery of a mechanism of the high-T_c phenomenon which typically occurs in the vicinity of a magnetic instability.

The main changes caused by replacing the N film in the MINS heterostructure with an F layer are related to the difference in their electronic structures. Since the charge reflected at the F/S interface in an MIFS sample is created in the electron density of states with a spin opposite to that of the incident quasiparticle, the scattering strength (and, as a result, the F/S bilayer resistance) strongly depends on the spin imbalance in the ferromagnet. Its theoretical analysis is usually based on the Stoner model of metallic ferromagnetism where charge carriers with opposite spins occupy rigidly shifted bands with the difference in energy equal to $2\varepsilon_{ex}$ (see Figure 1.2.1.3c). In this case, Fermi wave vectors for electron spin-up $k_F^{\uparrow}$ and spin-down $k_F^{\downarrow}$ bands are different: $\delta k^{(F)} = k_F^{\uparrow} - k_F^{\downarrow} = 2\varepsilon_{ex}/\hbar v_F =$ const (their energy dependence may be not taken into account for $\varepsilon \le \Delta \ll E_F$). For example, in Ni the averaged over Fermi surface s-subband values are $k_F^{\uparrow} = 5.1\ \text{nm}^{-1}$ and $k_F^{\downarrow} = 4.7\ \text{nm}^{-1}$ [26]. Thus, the semiclassical quantization condition for the Andreev bound state in an F interlayer looks as follows: $k_{Fx}^{\uparrow} d_F + \chi^{eh} - k_{Fx}^{\downarrow} d_F + \pi - k_{Fx}^{\downarrow} d_F + \chi^{he} + k_{Fx}^{\uparrow} d_F + \pi = 2\delta k_x^{(F)} d_F - 2\arccos(\overline{\varepsilon}/\Delta_S) = 2\pi j$, where d_F is the thickness of the F interlayer. As the distance from the F/S interface increases, the phase shift $\delta k_x^{(F)} d_F$ grows continuously and for $d_F \approx 2\pi\hbar v_F/4\varepsilon_{ex}$ is equal to π. This phase shift produces oscillations of the superconducting order parameter

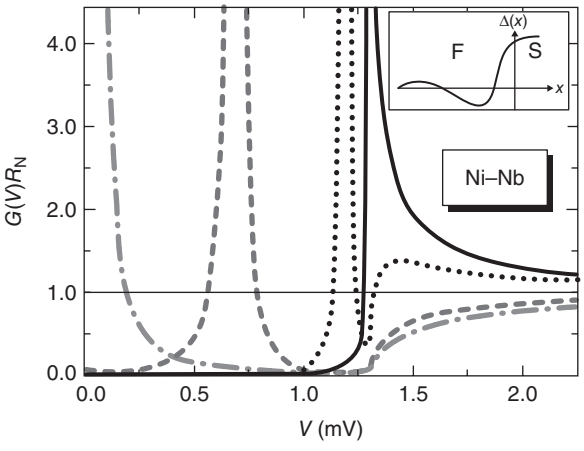

Figure 1.2.1.6 Calculated differential conductance-versus-voltage dependencies for a tunneling junction with a Ni/Nb bilayer; $d_F = 0$ nm (solid line), 1.0 nm (dotted line), 2.5 nm (dashed line), and 4.0 nm (dashed-dotted line), R_N is the resistance of the junction in a normal state; the Nb energy gap was set to 1.3 meV; temperature $T = 0$. The inset demonstrates schematic behavior of the superconducting order parameter in the F/S bilayer. The continuity of $\Delta(x)$ at the interface implies the absence of the potential barrier. In the general case, the jump of the order parameter occurs at $x = 0$ like in Figure 1.2.1.1. (Adapted from [26]. Reproduced with permission of World Scientific Publishing Company.)

on a length scale $\sim 1/\delta k^{(F)} = \hbar v_F/2\varepsilon_{ex}$ (see the inset in Figure 1.2.1.6). The states corresponding to a positive sign of the order-parameter real part are called *0-states* and those corresponding to the negative sign are known as *π-states*. In general, the overall character of the differential conductance for finite thicknesses of the F interlayer remains similar to that for MINS junctions, but now the measurable shift of the peak in $G(V)$ can be obtained for relatively small values of d_F. The effect of increasing d_{Ni} from 0 to 5 nm in transport characteristics of Al–I–Ni/Nb samples measured by SanGiorgio *et al.* [27] well agree with related numerical simulations by Belogolovskii *et al.* [26] including an anomalous double-peak structure for extremely thin Ni films (Figure 1.2.1.6).

In addition to the spatial oscillations of the pair wavefunction, spin-singlet Cooper pairs are fragile under the exchange potential which affects differently electrons with opposite spins. As in N metals, the penetration of superconducting correlations into a ferromagnetic metal is limited by dephasing between electron and hole wave functions but in the case of an F layer, it is much stronger. That is why for a direct FS bilayer, the penetration depth is atomically short (the only exception is the clean limit $l_e \gg \xi_0$ at $k_B T \ll \varepsilon_{ex}$ when it is limited only by elastic impurity scattering and typically exceeds the oscillation period). In general, the decay value depends on the presence of elastic scatterings as well as on the strength of the exchange field (see the review by Golubov *et al.* [14]). In the dirty limit at $T = 0$, the decay length exactly coincides with the oscillation period and for sufficiently strong diffusive ferromagnetic materials like Fe, Co, Ni even at finite temperatures $\xi_F = \sqrt{\hbar D/(2\varepsilon_{ex})}$. But in the general case, especially for weak ferromagnets, when the temperature and the exchange field are equally important, the period of the Cooper potential oscillations and their decay do not coincide. Moreover, when the temperature is going down, the decay length increases whereas the oscillations period decreases. Because of it, the temperature variation can be used as a good tool for engineering the phase shift of the superconducting order parameter along the F layer from 0 to π [28].

The new burst of interest to the F/S problem is associated with the so-called long-range equal spin-triplet pairing state, a new type of proximity-induced superconducting state in ferromagnets which can be realized in the presence of a magnetically inhomogeneous F/S interface [29]. Spin-dependent phase shifts which are acquired by electrons penetrating through the interface can induce spin-triplet s-wave Cooper pairs in ferromagnets. The latter ones should have the odd-frequency symmetry to satisfy the requirement from the Fermi–Dirac statistics of electrons and be not suppressed by the exchange potential. If so, they are able to deepen into the ferromagnet at distances of the order of the decay length ξ_T for a normal metal. The novel aspect of the PE consists in the fact that by introducing a low-transparent magnetic interface, we can enhance the penetration depth into the F layer from nanometers for singlet pairing to microns (at least, at very low temperatures) for triplet one. The relative fraction of odd-frequency pairs to even-frequency pairs depends sensitively on such junction parameters as its geometry, the interface transparency, and so on. Notice also that the inhomogeneous magnetization needed for the transformation does

not necessarily be intrinsic. For example, it can be introduced by two misaligned magnetic layers like in the experiment by Khare *et al.* [30].

Let us now discuss a few practically useful ideas from a long list of striking proposals relating the PE in systems with S and F layers. As was explained above, in FS contacts the PE manifests itself in the damped oscillatory behavior of superconducting correlations induced in a ferromagnet. As a result, for certain thicknesses of the F layer and temperatures, the order parameter in a superconductor–ferromagnet–superconductor (SFS) junction may become positive at one S electrode and negative at the other S electrode. In this situation, one gets a π Josephson junction with the spontaneous π-shift of the phase difference in its ground state. Its properties are indeed unusual. For example, when connecting the S electrodes with a superconducting wire, one may expect the spontaneous super-current circulating in the loop, passing clockwise or counterclockwise. It has been experimentally demonstrated that the π-junction improves the performance and simplifies the design of classical and quantum circuits. An idea to introduce π-junctions as passive phase shifters in rapid single flux quantum (RSFQ) circuits was proposed by Ustinov and Kaplunenko [31]. It permits (i) to use only conventional junctions to carry flux quanta, and thus to provide logical functionality, (ii) to substitute by π-junctions the relatively large geometrical inductance of storing a single-flux quantum RSFQ cells and, hence, to reduce greatly the size of RSFQ circuits, (iii) to operate in the passive mode which has some advantages over the active regime. In a φ-junction, a generalization of the π-junction with a doubly degenerate ground state, the Josephson phase takes the values $+\varphi$ or $-\varphi$ ($0 < \varphi < \pi$) [32]. This device is, in fact, a phase battery providing an arbitrary phase shift and being closed into a ring is able to self-generate a fractional flux $\varphi\Phi_0/(2\pi)$, where Φ_0 is the magnetic flux quantum.

Moreover, superconducting devices with a magnetic interlayer can be useful for the solution of other problems of superconducting electronics and so are able to realize its high performance potential. Let us provide some examples. The first problem relates the lack of high-capacity superconducting random access memory [33]. Magnetic Josephson junctions, that is, superconducting structures with incorporated magnetic layer(s), were suggested to perform both data storage and readout functions. By applying magnetic field pulses (e.g., by current pulses through a superconducting write line), the F-layer can be magnetized in two opposite directions. To discriminate these directions, a read current bias is applied through the junction inducing a reference magnetic field. Depending on F-layer magnetization, this field either adds to or subtracts from F-layer magnetic field effectively forming two possible magnetic states with high or low magnetizations corresponding to low ("1") and high ("0") critical currents, respectively [33]. Another problem relates a superconducting three-terminal device which could switch and amplify electric signals like a semiconducting transistor. One of the most promising designs is a double-barrier $S_1IS_2IS_3$ structure based on the tunneling injection of nonequilibrium quasiparticles through a thin insulating layer into the middle S_2 layer and detection of the

resultant energy gap suppression by the second junction. While possessing essential transistor-like characteristics, the "symmetric" $S_1IS_2IS_3$ device has a drawback detrimental for its implementation, namely, lack of isolation between the input and output terminals. Nevirkovets and Belogolovskii [34] proposed to block parasitic back-action of the acceptor junction by a few-nanometer thick inhomogeneous ferromagnetic film inserted between the barrier and the middle S_2 layer. At last, the long-range PEs in ferromagnets pave the way for the controlled creation of completely spin-polarized super-currents which would necessarily have to be triplet. Such superconducting spintronics devices are, in particular, ideal candidates for quantum computing.

1.2.1.5 New Perspectives and New Challenges

A new step in the development of the PE that started several years ago is related to the search of Majorana fermions (see the review by Beenakker [35]). These hypothetical elementary particles which are often described as "half fermions" since they are the only fermionic particles expected to be their own antiparticles, have not been identified in the nature yet but can exist as quasiparticle excitations in solid-state systems. A great variety of strategies has been put forward in recent years to engineer Majorana fermions in different condensed-matter platforms. One of the most promising proposals is to use proximity-induced superconductivity in the surface of topological insulators, a new phase of matter where conduction of electrons occurs only on the surfaces due to strong spin–orbit coupling, which inverts the order of conduction and valence bands. Three-dimensional topological insulators have surface electron states with massless Dirac cones in which the spin of an electron is locked perpendicular to its momentum in a chiral spin structure where electrons with opposite momenta have opposite spins. When such a material is brought in contact with a conventional spin-singlet, s-wave S layer, superconductivity is induced on its surface, with a nondegenerate state at the Fermi level ($\varepsilon = 0$), in the middle of the superconducting gap. This specific midgap state following from the electron–hole symmetry is just the Majorana fermion. A key probe to detect it experimentally is the tunneling differential conductance which should show a peak at zero-voltage bias. Several groups have already reported zero-bias anomalies in corresponding PE devices (see, in particular, [36]). Another interesting prediction is a 4π-periodic Josephson effect [35]. At the moment it is not clear whether or not the observed anomalous features reflect a Majorana bound state signature. But, if the presence of Majorana fermions is proved, it will provide a fundamentally new way to store and manipulate quantum information, with possible applications in a quantum computer [35].

The progress in the PE research and arising challenges are not limited by this exotic field. Whereas the main fundamental features of the N/S PE (at least, for traditional superconductors) are clear, less is known about such structures very far from equilibrium as well as about nonlocal correlations in a proximized N layer (see [37, 38]). The problem of the competition between electron–electron interactions and the superconducting PE remains largely unexplored. Recent

experiments [39] have shown that graphene provides a useful experimental platform to investigate it. Up to now, it is not clear why sometimes the T_c of a superconductor is increased upon attachment to a nonsuperconducting material. For example, in the work by Katzir *et al.* [40], it was shown that the T_c of thin Nb films increases by up to 10% when they are chemically linked to gold nanoparticles using ~3 nm long disilane linker molecules.

Even more questions are arising for contacts between superconducting and magnetic materials. While much of the work on F/S PE is focused on the penetration of the superconducting order parameter into the ferromagnet, very little was done to understand the penetration of the magnetization into the adjacent S metal which is often called *the inverse proximity effect*. The first theoretical interpretation of the problem arising in F/S bilayers was done by Krivoruchko and Koshina [41]. Direct experimental observation of the inverse PE in Ni/Pb and Co–Pd/Al bilayers was presented in the work by Xia *et al.* [42] where it was shown that the magnetization in a ferromagnetic film induces a magnetization in a superconducting film that is much smaller and opposite in sign.

Although singlet superconductivity and ferromagnetism are mutually exclusive in homogeneous bulk materials, magnetization noncollinearity is expected to enhance T_c. Zhu *et al.* [43] observed a nonmonotonic enhancement of superconductivity with the increase of magnetic noncollinearity in a related F/S sandwich. An interest in PE contacts formed by superconductors and antiferromagnets (AFs) has increased when it was found that at low temperatures iron-based superconductors can be intrinsically phase separated into antiferromagnetic and superconducting regions. Corresponding theoretical predictions [44] have not been yet checked experimentally.

1.2.1.6 Summary

The current understanding of the relationship between the PE in the old sense, as a leakage of superconductivity into a normal metal, and the Andreev backscattering at the NS interface is that they are only two sides of the same coin. Whereas this statement helped to understand the basic observations for N/S bilayers, it is not so in the case of F/S structures. From the experimental side, one of the most significant recent developments has been a striking phenomenon of generation of odd-frequency spin-triplet s-wave pairs in F/S devices by spin-mixing due to inhomogeneous magnetization or spin-dependent potential. New physics is yet to be captured in the theoretical treatments of F/S systems.

Discovery of topological superconductivity has paved the way for the novel states of quantum matter which are not only of a fundamental significance but have potential practical implications as well. The resemblance of the new exotic phase with strong spin–orbit coupling to the already studied spin-triplet superconductivity without it [45] permits to reveal the essential physics of the PE in the novel materials using the previous knowledge about spin-triplet superconductors. In our opinion, experimental and theoretical efforts aimed to create topological superconductors, gapped phases of fermionic quantum matter

whose zero-energy states can be associated with Majorana quasiparticles, will certainly be a major research theme in the PE field for the nearest future.

References

1. Buckel, W. and Kleiner, R. (2004) *Superconductivity. Fundamentals and Applications*, 2nd edn, John Wiley & Sons, Ltd, Chichester.
2. McMillan, W.L. (1968) Tunneling model of the superconducting proximity effect. *Phys. Rev.*, **175** (2), 537–542.
3. McMillan, W.L. (1968) Theory of superconducting–normal-metal interface. *Phys. Rev.*, **175** (2), 559–568.
4. Seidel, P. and Richter, J. (1980) Theoretical investigation of the current-voltage characteristics of superconducting niobium-lead tunnel junctions. *Phys. Status Solidi B*, **98** (1), 189–197.
5. Gilabert, A. (1977) Effet de proximité entre un metal normal et un supraconducteur. *Ann. Phys.*, **2** (4), 203–252.
6. Pannetier, B. and Courtois, H. (2000) Andreev reflection and proximity effect. *J. Low Temp. Phys.*, **118** (5-6), 599–615.
7. Klapwijk, T.M. (2004) Proximity effect from the Andreev perspective. *J. Supercond.*, **17** (5), 593–611.
8. Miller, C.W. and Belyea, D.D. (2009) The impact of barrier height distributions in tunnel junctions. *J. Appl. Phys.*, **105** (9), 094505-1–094505-5.
9. Louie, S.G. and Cohen, M.L. (1976) Electronic structure of a metal-semiconductor interface. *Phys. Rev. B*, **13** (6), 2461–2469.
10. Choi, S.K., Lee, D.-H., Louie, S.G., and Clarke, J. (2009) Localization of metal-induced gap states at the metal–insulator interface: origin of flux noise in SQUIDs and superconducting qubits. *Phys. Rev. Lett.*, **103** (19), 197001-1–197001-4.
11. Bachar, N., Lerer, S., Hacohen-Gourgy, S., Almog, B., and Deutscher, G. (2013) Kondo-like behavior near the metal-to-insulator transition of nanoscale granular aluminum. *Phys. Rev. B*, **87** (21), 214512-1–214512-4.
12. Halbritter, J. (2005) Transport in superconducting niobium films for radio frequency applications. *J. Appl. Phys.*, **97** (8), 083904-1–083904-12.
13. Knauer, H., Richter, J., and Seidel, P. (1977) A direct calculation of the resonance tunneling in metal–insulator–metal tunnel junctions. *Phys. Status Solidi A*, **44** (1), 303–312.
14. Golubov, A.A., Kupriyanov, M.Y., and Il'ichev, E. (2004) The current-phase relation in Josephson junctions. *Rev. Mod. Phys.*, **76** (2), 411–469.
15. Blonder, G.E., Tinkham, M., and Klapwijk, T.M. (1982) Transition from metallic to tunneling regimes in superconducting microconstrictions: excess current, charge imbalance, and supercurrent conversion. *Phys. Rev. B*, **25** (7), 4515–4532.
16. Belogolovskii, M., Grajcar, M., Kúš, P., Plecenik, A., Beňačka, Š., and Seidel, P. (1999) Phase-coherent charge transport in superconducting heterocontacts. *Phys. Rev. B*, **59** (14), 9617–9626.
17. Pilgram, S., Belzig, W., and Bruder, C. (2000) Excitation spectrum of mesoscopic proximity structures. *Phys. Rev. B*, **62** (18), 12462–12467.
18. Likharev, K.K. (1979) Superconducting weak links. *Rev. Mod. Phys.*, **51** (1), 101–159.
19. Kupriyanov, M.Y. and Lukichev, V.F. (1988) Influence of boundary transparency on the critical current of "dirty" SS'S structures. *Zh. Eksp. Teor. Fiz.*, **94** (6), 139–149 (*Sov. Phys. JETP*, **67**(6), 1163–1168).
20. Belzig, W., Bruder, C., and Fauchère, A.L. (1998) Diamagnetic response of a normal-metal–superconductor proximity system of arbitrary impurity concentration. *Phys. Rev. B*, **58** (21), 14531–14540.
21. De Gennes, P.G. (1964) Boundary effects in superconductors. *Rev. Mod. Phys.*, **36** (1), 225–237.
22. Gildemeister, J.M., Lee, A.T., and Richards, P.L. (1999) A fully lithographed

voltage-biased superconducting spider-web bolometer. *Appl. Phys. Lett.*, **74** (6), 868–870.

23. Kain, B., Khan, S.R., and Barber, R.P. Jr., (2002) Tuning the transition temperature of superconducting Ag/Pb films via the proximity effect. *Physica C*, **382** (4), 411–414.
24. Lacquaniti, V., De Leo, N., Fretto, M., Sosso, A., Boilo, I., and Belogolovskii, M. (2012) Advanced four-layered Josephson junctions for digital applications. *Physics Procedia*, **36**, 100–104.
25. Žutić, I., Fabian, J., and Das Sarma, S. (2004) Spintronics: fundamentals and applications. *Rev. Mod. Phys.*, **76** (2), 323–410.
26. Belogolovskii, M., De Leo, N., Fretto, M., and Lacquaniti, V. (2011) Quantum size effects in superconducting junctions with a ferromagnetic interlayer. *Int. J. Quantum Inf.*, **9** (Suppl. 01), 301–308.
27. SanGiorgio, P., Reymond, S., Beasley, M.R., Kwon, J.H., and Char, K. (2008) Anomalous double peak structure in superconductor/ferromagnet tunneling density of states. *Phys. Rev. Lett.*, **100** (23), 237002-1–237002-4.
28. Ryazanov, V.V., Oboznov, V.A., Rusanov, A.Y., Veretennikov, A.V., Golubov, A.A., and Aarts, J. (2001) Coupling of two superconductors through a ferromagnet: evidence for a π junction. *Phys. Rev. Lett.*, **86** (11), 2427–2430.
29. Bergeret, F.S., Volkov, A.F., and Efetov, K.B. (2005) Odd triplet superconductivity and related phenomena in superconductor–ferromagnet structures. *Rev. Mod. Phys.*, **77** (4), 1321–1373.
30. Khare, T.S., Khasawneh, M.A., Pratt, W.P. Jr.,, and Birge, N.O. (2010) Observation of spin-triplet superconductivity in Co-based Josephson junctions. *Phys. Rev. Lett.*, **104** (13), 137002-1–137002-4.
31. Ustinov, A.V. and Kaplunenko, V.K. (2003) Rapid single-flux quantum logic using π- shifters. *J. Appl. Phys.*, **94** (8), 5405–5407.
32. Sickinger, H., Lipman, A., Weides, M., Mints, R.G., Kohlstedt, H., Koelle, D., Kleiner, R., and Goldobin, E. (2012) Experimental evidence of a φ Josephson junction. *Phys. Rev. Lett.*, **109** (10), 107002-1–107002-5.
33. Larkin, T.I., Bol'ginov, V.V., Stolyarov, V.S., Ryazanov, V.V., Vernik, I.V., Tolpygo, S.K., and Mukhanov, O.A. (2012) Ferromagnetic Josephson switching device with high characteristic voltage. *Appl. Phys. Lett.*, **100** (22), 222601-1–222601-4.
34. Nevirkovets, I.P. and Belogolovskii, M.A. (2011) Hybrid superconductor–ferromagnet transistor-like device. *Supercond. Sci. Technol.*, **24** (2), 024009-1–024009-8.
35. Beenakker, C.W.J. (2013) Search for Majorana fermions in superconductors. *Annu. Rev. Condens. Matter Phys.*, **4**, 113–136.
36. Mourik, V., Zuo, K., Frolov, S.M., Plissard, S.R., Bakkers, E.P.A.M., and Kouwenhoven, L.P. (2012) Signatures of Majorana fermions in hybrid superconductor–semiconductor nanowire devices. *Science*, **336** (6084), 1003–1007.
37. Kauppila, V.J., Nguyen, H.Q., and Heikkilä, T.T. (2013) Nonequilibrium and proximity effects in superconductor–normal metal junctions. *Phys. Rev. B*, **88** (7), 075428-1–075428-7.
38. Noh, T., Davis, S., and Chandrasekhar, V. (2013) Nonlocal correlations in a proximity-coupled normal metal. *Phys. Rev. B*, **88** (2), 024502-1–024502-7.
39. Deon, F., Sopic, S., and Morpurgo, A.F. (2014) Tuning the influence of microscopic decoherence on the superconducting proximity effect in a graphene Andreev interferometer. *Phys. Rev. Lett.*, **112** (12), 126803-1–126803-5.
40. Katzir, E., Yochelis, S., Zeides, F., Katz, N., Kalcheim, Y., Millo, O., Leitus, G., Myasodeyov, Y., Shapiro, B.Y., Naaman, R., and Paltiel, Y. (2012) Increased superconducting transition temperature of a niobium thin film proximity coupled to gold nanoparticles using linking organic molecules. *Phys. Rev. Lett.*, **108** (10), 107004-1–107004-5.
41. Krivoruchko, V.N. and Koshina, E.A. (2002) Inhomogeneous magnetism induced in a superconductor at a superconductor–ferromagnet interface. *Phys. Rev. B*, **66** (1), 014521-1–014521-6.
42. Xia, J., Shelukhin, V., Karpovski, M., Kapitulnik, A., and Palevski, A.

(2009) Inverse proximity effect in superconductor–ferromagnet bilayer structures. *Phys. Rev. Lett.*, **102** (8), 087004-1–087004-4.

43. Zhu, L.Y., Liu, Y., Bergeret, F.S., Pearson, J.E., te Velthuis, S.G.E., Bader, S.D., and Jiang, J.S. (2013) Unanticipated proximity behavior in ferromagnet-superconductor heterostructures with controlled magnetic noncollinearity. *Phys. Rev. Lett.*, **110** (17), 177001-1–177001-5.
44. Krivoruchko, V.N. and Belogolovskii, M.A. (1995) Proximity-induced superconductivity in an antiferromagnetic exchange field. *Phys. Rev. B*, **52** (13), 9709–9713.
45. Nagai, Y., Nakamura, H., and Machida, M. (2013) Quasiclassical treatment and odd-parity/triplet correspondence in topological superconductors. *J. Phys. Soc. Jpn.*, **83** (5), 053705-1–053705-4.

1.2.2

Tunneling and Superconductivity

Steven T. Ruggiero

1.2.2.1 Introduction

Superconducting and related tunneling is a rich and broad field involving investigations of the basic nature of superconductivity and other phenomena, and includes a wide variety of unique electronic devices. Tunneling is a powerful tool for uncovering the properties of the metals and insulators comprising tunnel systems, and can reveal the excitation spectra of various types of species incorporated into tunnel systems. Since electrons are injected from one conductor into another through an insulating barrier, we are performing spectroscopy [1]. And because of the physical nature of tunnel junctions, it is straightforward to accurately measure the energy of the tunneling electrons.

1.2.2.2 Normal/Insulator/Normal Tunnel Junctions

Consider a simple tunnel junction comprising two normal metals separated by a thin (~1–2 nm) insulating barrier, a normal-metal/insulator/normal-metal (NIN) junction as shown in Figure 1.2.2.1. Depicted is the semiconductor model (Figure 1.2.2.1a) for a system comprising two normal metals with states filled to the Fermi level, offset by the energy eV, where V is the externally applied bias voltage. In this case, the current–voltage (I–V) characteristic, Figure 1.2.2.1b, is linear for small voltages compared to the tunnel barrier height of the insulator, $\phi \sim 1$ eV, and rises rapidly as the applied voltage approaches ϕ as:

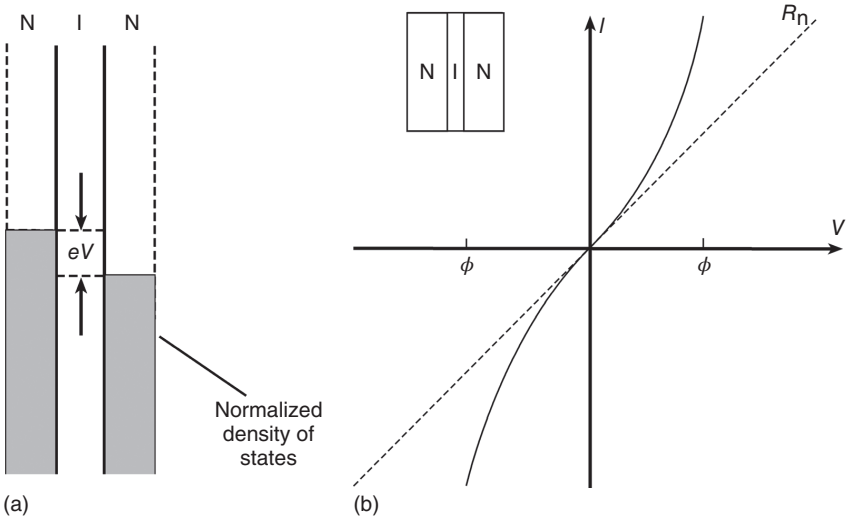

Figure 1.2.2.1 (a) Density of states for normal-metal/insulator/normal-metal (NIN) tunnel junction. (b) Current–voltage characteristics for a NIN tunnel junction.

$$I = \left(\frac{1}{R_n}\right)(V + aV^3) \tag{1.2.2.1}$$

where a is a barrier-dependent scaling parameter. Otherwise, the tunneling characteristics are featureless.

1.2.2.3 Normal/Insulator/Superconducting Tunnel Junctions

If we make one of the materials in a tunnel system superconducting, we have a normal-metal/insulator/superconductor (NIS) junction, with $I-V$ characteristics markedly changed at low voltage compared to the featureless NIN systems. At applied bias voltages typically on the order of ~1–10 mV, the energy gap in the superconducting density of states will be strongly manifest in the tunnel characteristics. We can see this effect by again viewing tunneling in the so-called semiconductor model (Figure 1.2.2.2a). Here, the tunneling process is depicted as the convolution of the tunneling densities of state a superconductor, with an energy gap Δ, and a normal metal, where the zero-temperature superconducting energy gap is given by

$$\begin{aligned}\Delta(0) &= \pi e^{-\gamma} k_B T_c \\ &= 1.764\ k_B T_c\end{aligned} \tag{1.2.2.2}$$

and $\gamma = 0.5772\ldots$ is the Euler–Mascheroni constant.

In this case, the tunnel current is given by

$$I_{NS} = \frac{1}{eR_n}\int_{-\infty}^{\infty} \frac{|E|}{[E^2 - \Delta^2]^{\frac{1}{2}}}[f(E) - f(E+eV)]dE \tag{1.2.2.3}$$

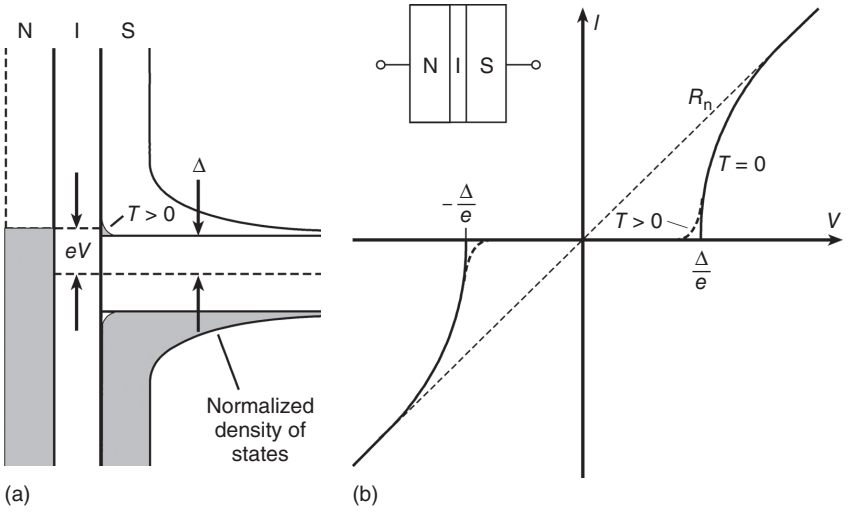

Figure 1.2.2.2 (a) Density of states for a normal-metal/insulator/superconductor (NIS) tunnel junction. For $T > 0$, some electrons are thermally excited across (twice) the superconducting energy gap Δ. (b) Current–voltage characteristics for NIS tunnel junction.

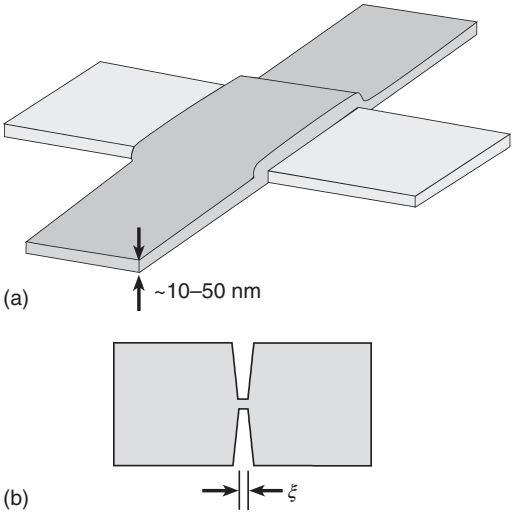

Figure 1.2.2.3 Shown on (a) is a tunnel junction, in its simplest form comprising a "sandwich" of a thin-film base electrode, a thin insulating barrier, and a top electrode and (b) is a weak-link Josephson system. Here, macroscopic superconducting elements are coupled by a small bridge or point contact, on the order of or smaller than the superconducting coherence length ξ.

where $f(E)$ is the Fermi function. The resultant $I-V$ characteristics are shown in Figure 1.2.2.2b. Giaever [2] observed the superconducting energy gap by creating NIS junctions of the form $Al/Al_2O_3/Pb$. This was done by vapor depositing a thin film of Al, allowing it to oxidize to create a $\sim 1-2$ nm thick insulating tunnel barrier, and finally depositing a cross stripe of Pb (and in a separate experiment In). These so-called "sandwich" junctions (see Figure 1.2.2.3) were measured at temperatures above the critical temperature of the Al stripe. Countless experiments on a variety of superconducting materials followed from this seminal work. Barriers can also be formed "artificially" by the direct deposition of insulating or semiconducting materials [3].

1.2.2.4 Superconductor/Insulator/Superconducting Tunnel Junctions

In the case where both materials are superconducting, the tunneling behavior becomes yet more interesting (Figure 1.2.2.4). For superconductor/insulator/superconductor (SIS) systems, the tunnel current is given by the expression:

$$I_{SS} = \frac{1}{eR_n}\int_{-\infty}^{\infty} \frac{|E|}{[E^2-\Delta_1^2]^{\frac{1}{2}}} \frac{|E+eV|}{[(E+eV)^2-\Delta_2^2]^{\frac{1}{2}}} [f(E)-f(E+eV)]dE \quad (1.2.2.4)$$

where the integral is assumed to exclude values of E, where $|E| < \Delta_1$ and $|E+eV| < \Delta_2$. If we follow the characteristics along the voltage axis, for quasiparticle tunneling, we see a current rise to V/R_n when we reach a bias potential $V = (\Delta_1 + \Delta_2)/e$, where R_n is the normal tunnel resistance in the absence of

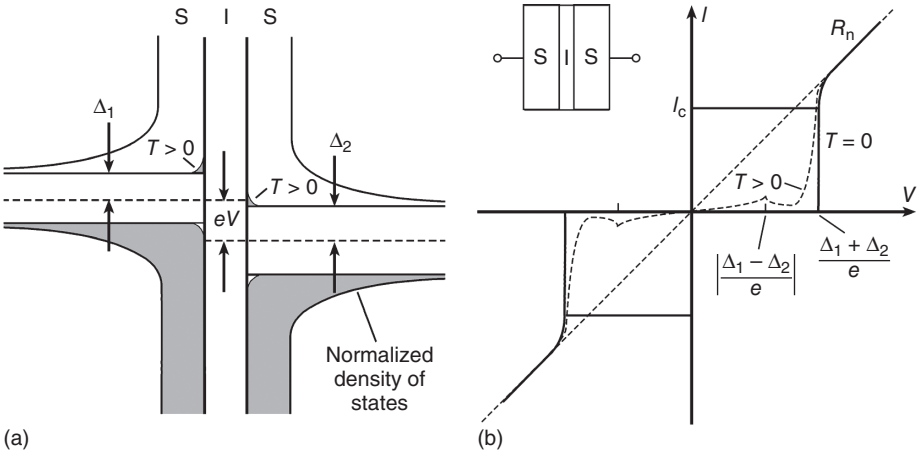

Figure 1.2.2.4 (a) Density of states for a superconductor/insulator/superconductor (SIS) tunnel junction. (b) Current–voltage characteristics for an SIS tunnel junction.

superconductivity. At finite temperature, an increase in current will also be observed at a bias voltage of $V = |\Delta_1 - \Delta_2|/e$.

There is also a rich set of phenomenology associated with the second, zero-voltage Josephson branch of the I–V characteristics. Here, the current rises – at zero voltage identically – until a maximum sustainable or critical current, I_c, is reached. This is a manifestation of the DC Josephson effect [4], where Cooper pairs tunnel through the barrier. This phenomenon was observed by Anderson and Rowell [5] using Sb/Sb-oxide/Pb tunnel junctions prepared using the technique of Giaever as noted earlier.

Josephson effects can also be observed in so-called weak-link systems (Figure 1.2.2.3), where a nanoscale-size superconducting element connects macroscopic-scale superconductors, as with a so-called point contact. The critical current is given in general by Ambegaokar and Baratoff [6]

$$I_c R_n = \frac{\pi[\Delta_1(T) + \Delta_2(T)]}{4e} \tanh \frac{\Delta_1(T) + \Delta_2(T)}{4k_B T} \tag{1.2.2.5}$$

At $T = 0$, then, both tunnel junctions and – in the dirty limit [7] – weak links will have a critical value given by:

$$I_c R_n = \frac{\pi[\Delta_1(0) + \Delta_2(0)]}{4e} \tag{1.2.2.6}$$

For temperatures in the vicinity of T_c, we have:

$$\begin{aligned} I_c R_n &= \left(\frac{2.34\pi k_B}{e}\right)(T_c - T) \\ &\approx (T_c - T)\ \ 635\,\mu\mathrm{V\,K^{-1}} \end{aligned} \tag{1.2.2.7}$$

We note that this temperature dependence is strictly applicable in the case of tunnel junctions (the topic of this chapter). Other Josephson devices – such

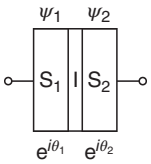

Figure 1.2.2.5 Two superconductors separated by an insulating tunnel barrier.

as weak links and superconductor/constriction/superconductor (ScS), superconductor/normal-metal/superconductor (SNS), superconductor/insulator/normal-metal/superconductor (SINS), superconductor/insulator/normal-metal/insulator/superconductor (SINIS), superconductor/ferromagnet/superconductor (SFS), and so on systems – will have a temperature dependence of $I_c R_n$ that can differ considerably from this classic Ambegaokar–Baratoff result.

To better understand the origin of Josephson behavior in tunnel junctions, let us consider two superconductors separated by an insulating barrier, as sketched in Figure 1.2.2.5. Each superconducting condensate can be described by a single wavefunction as $\psi_i = \sqrt{n_i} e^{i\theta_i}$, where n is the density of superconducting electrons and θ is a phase factor. If a potential energy $U_2 - U_1 = 2eV$ exists between the superconductors, then the applicable coupled Schroedinger equations can be written as:

$$i\hbar \frac{\partial \psi_1}{dt} = U_1 \psi_1 + K\psi_2$$
$$i\hbar \frac{\partial \psi_2}{dt} = U_2 \psi_2 + K\psi_1 \qquad (1.2.2.8)$$

where K is a coupling constant. Defining $\Delta\theta = \theta_1 - \theta_2$, this leads to a current flow of:

$$I = I_c \sin \Delta\theta \qquad (1.2.2.9)$$

where $I_c = 2K(n_1 n_2)^{1/2}/\hbar$. We also have

$$\frac{\partial(\Delta\theta)}{\partial t} = \frac{2eV}{\hbar} \qquad (1.2.2.10)$$

Equations (1.2.2.9) and (1.2.2.10) represent the DC and AC Josephson effects. Thus, for a fixed applied voltage difference, V, there is a steadily increasing phase difference

$$\Delta\theta(t) = \Delta\theta(0) + \frac{2eV}{\hbar} t \qquad (1.2.2.11)$$

Therefore, the Josephson current will oscillate at a frequency

$$f = \frac{2eV}{h} \qquad (1.2.2.12)$$

This result is remarkable in that it is true exactly, and that the appropriate charge is indeed $2e$, the charge of a Cooper pair. The Josephson frequency $2e/h = 483.6\,\text{GHz mV}^{-1}$. When a Josephson junction is irradiated with radio-frequency waves of frequency f, a series of steps will appear in the DC I–V

characteristics at voltages

$$V_n = \frac{nhf}{2e} \tag{1.2.2.13}$$

These Shapiro steps [8] are the basis of Josephson-junction-based voltage standards because the frequency of microwaves can be very accurately determined, see Chapter 7. $N \times M$ arrays of microwave-irradiated Josephson junctions can produce so-called "giant" Shapiro steps of voltage

$$V_n = N\frac{nhf}{2e} \tag{1.2.2.14}$$

for arrays N junctions long in the direction of the current flow. This situation can also be reversed to produce voltage-tunable microwave radiation sources [9]. While typically producing very low rf power, such arrays are suitable for applications such as local oscillators for low-noise superconductor-based mixers.

We note finally that for the high-temperature superconductors, a separate class of internal, so-called intrinsic Josephson effects has been discussed in the literature, related to interlayer coupling [10].

1.2.2.5 Superconducting Quantum Interference Devices (SQUIDs)

We can also create a very interesting device by placing two Josephson junctions in a ring as shown in Figure 1.2.2.6a. Here, we have two critical currents of I_{c1} and I_{c2}, so the total current is

$$I = I_{c1}\sin(\Delta\theta_1) + I_{c2}\sin(\Delta\theta_2) \tag{1.2.2.15}$$

If we apply a magnetic field, then the flux in the ring will then be given as

$$\begin{aligned}\Phi &= \int \boldsymbol{B}\cdot d\boldsymbol{S} \\ &= \oint \boldsymbol{A}\cdot d\ell \\ &= \frac{\Phi_0}{2\pi}\oint(\nabla\theta)\cdot d\ell\end{aligned} \tag{1.2.2.16}$$

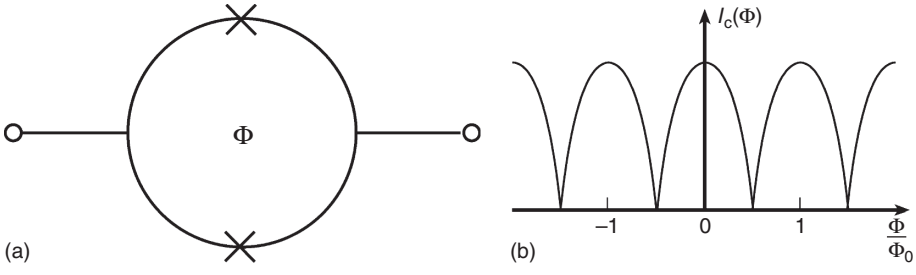

Figure 1.2.2.6 (a) A superconducting quantum interference device (SQUID) comprising two Josephson junctions in a loop. (b) Critical current as a function of applied flux for a SQUID.

where $\Phi_0 = h/2e = 2.068 \times 10^{-15}$ T m^2 is the magnetic flux quantum. Assuming we have chosen a specific loop contour, we can then say

$$\Delta\theta = 2\pi \frac{\Phi}{\Phi_0} (\text{mod } 2\pi) \tag{1.2.2.17}$$

For a system with identical junctions, we can write

$$\begin{aligned} I &= I_c \sin(\Delta\theta_1) + I_c \sin(\Delta\theta_2) \\ &= I_c \sin\left[\Delta\theta + \frac{\pi\Phi}{\Phi_0}\right] + I_c \sin\left[\Delta\theta - \frac{\pi\Phi}{\Phi_0}\right] \\ &= 2I_c \sin(\Delta\theta) \cos\frac{\pi\Phi}{\Phi_0} \end{aligned} \tag{1.2.2.18}$$

So the critical current will be modulated by the applied flux as

$$I_c(\Phi) = I_0 \left|\cos\frac{\pi\Phi}{\Phi_0}\right| \tag{1.2.2.19}$$

as depicted in Figure 1.2.2.6b. Because the flux quantum is so small, this means that superconducting quantum interference devices (SQUIDs) represent the most sensitive systems for the detection of magnetic flux, permitting measurements of absolute magnetic fields as small as $\sim 10^{-15}$ T.

Note that for a single junction, the application of a magnetic field leads to a Fraunhofer dependence of the critical current for the case of homogeneous current density. This behavior is analogous to single-slit optical diffraction. For further discussion and examples, see Chapter 9. Other references to Josephson effects can be found in texts on the subject [11].

1.2.2.6 **Phonon Structure**

Basic information can be obtained about the superconducting electrodes of tunnel junctions by studying the details of their $I-V$ characteristics. Of course the tunneling characteristics immediately supply the superconducting energy gap (or gaps) of the materials involved. In addition, we can learn about the phonon structure of phonon-mediated superconductors. The superconducting density of states, embodied earlier in our tunneling equations, can be expressed as:

$$N_S(E) = N(0)\text{Re}\left[\frac{E^2}{E^2 - \Delta^2(E)}\right]^{\frac{1}{2}} \tag{1.2.2.20}$$

Here, we allow for the fact that the energy gap is not a structureless constant but has both real and imaginary parts, the latter of which correspond to damping by the creation of phonons, especially in the vicinity of energies $E = h\nu_{\text{phonon}}$ [12]. This effect can be readily observed as small deviations in the tunnel conductance as noted by Giaever *et al.* [13]. More detailed analysis can provide $\alpha^2 F(\omega)$, the electron–phonon coupling strength times the phonon density of states [14].

Obtaining the phonon density of states from tunneling falls into a larger category of inelastic electron tunneling spectroscopies (IETS), another important example of which is the examination of the vibrational spectra of molecular

absorbates. This is done by introducing molecular species into tunnel structures to create metal/insulator/absorbate/metal (MIAM) systems. This process can be as simple as first depositing an aluminum film, allowing it to oxidize to form a tunnel barrier, exposing the barrier to molecules in vapor form, and completing the junction with a compatible counter-electrode metal. As discussed by Hipps and Mazur [15], MIAMs can be employed to explore the vibrational and electron spectroscopic information of the metal electrodes (magnons and phonons, the latter as noted above), insulator, and absorbate. MIAMs have been applied to the study of surface chemistry and catalysis, adhesion and corrosion, molecular vibrational spectroscopy, and orbital-mediated tunneling.

1.2.2.7 Geometrical Resonances

Phenomena related to electron interference effects can also be explored. These effects have been observed as oscillations in the tunnel characteristics in systems of the type SIN′S and/or SIS′, where N′ and S′ vary in thickness. The observation of these effects may require especially clean films. For sub-gap energies, multiple Andreev reflections [16] and de Gennes–Saint-James bound states [17] can give rise to oscillations in the tunnel conductance which are nonperiodic in energy. For energies above the superconducting gap, geometric resonances can involve Tomasch oscillations [18] in superconducting electrodes and McMillan–Rowell oscillations [19] in normal electrodes. The bias-voltage spacings for Tomasch and McMillan–Rowell oscillations generally scale as $\Delta V = h\nu_{FS}/2ed_S$ ($\Delta_S \ll e\Delta V$) and $\Delta V = h\nu_{FN}/4ed_N$. Thus, the Fermi velocity and thicknesses of the superconducting and normal layers govern the period of the conductance oscillations.

1.2.2.8 Scanning Tunneling Microscopy

Scanning tunneling microscopy (STM) is a technique of vast importance and applicability. Both superconducting and normal-metal tips with atomic-level sharpness can be positioned within tunneling distance above surfaces. As the tip is rastered over a surface, a two-dimensional picture of its tunneling density of states can be created. As noted by De Lozanne [20], this information can be coupled with other powerful surface-scanning techniques such as atomic force microscopy (AFM), magnetic force microscopy (MFM), Hall effect (SHPM, scanning Hall probe microscopy), SQUID, microwave, near-field optical, or magneto-optic microscopies. These techniques have been notably useful in exploring the properties of the high-temperature superconductors.

1.2.2.9 Charging Effects

Charging effects can be observed in tunneling if either one or more of the tunnel electrodes has an ultra-small capacitance [21, 22] or else nano-size elements [23] are otherwise incorporated into the tunnel structure. To observe charging effects, it must also be generally true that $E_c = e^2/2C > k_B T$ and that the charging energy exceed the thermal energy, where C is the capacitance of the nano-element(s). It

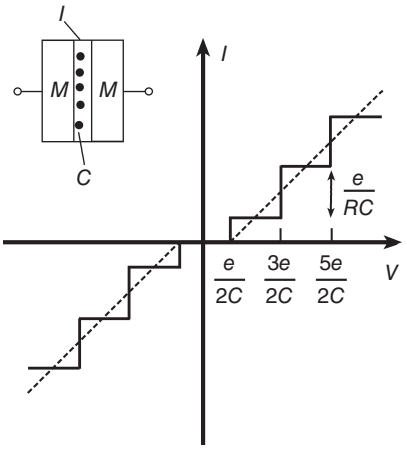

Figure 1.2.2.7 Shown is the coulomb staircase for tunneling into nano-droplets of metal incorporated into the insulating barrier structure of a metal/insulator/metal (M/I/M) tunnel system.

must also be true that $R > h/4e^2$ and that the effective resistance of the measured system exceed the quantum resistance.

In the case of nano-sized elements, tunnel junctions can be formed which incorporate metal particles ~1–10 nm in size into the tunnel barrier, which have charging energies in the vicinity of ~10 meV, as shown in Figure 1.2.2.7 [23]. Such junctions can exhibit both the "Coulomb blockade," a gap-like overall offset in the $I-V$ characteristics of voltage $e/2C$, and a series of steps of width e/C and height e/RC, which is the "Coulomb staircase."

References

1. Wolf, E.L. (1985) *Principles of Electron Tunneling Spectroscopy*, Oxford University Press, Inc., New York.
2. Giaever, I. (1960) Energy gap in superconductors measured by electron tunneling. *Phys. Rev. Lett.*, **5**, 147–148.
3. Ruggiero, S.T. (1988) Artificial tunnel barriers, in *Superconducting Devices* (eds S.T. Ruggiero and D.A. Rudman), Academic Press, New York.
4. Josephson, B.D. (1962) Possible new effects in superconductive tunneling. *Phys. Lett.*, **1**, 251–253; *Adv. Phys.*, (1965), **14**, 4191.
5. Anderson, P.W. and Rowell, J.M. (1963) Probable observation of the Josephson superconducting tunneling effect. *Phys. Rev. Lett.*, **10**, 230–232.
6. Ambegaokar, V. and Baratoff, A. (1963) Tunneling between superconductors. *Phys. Rev. Lett.*, **10**, 486–489; erratum (1963) **11**, 104.
7. Tinkham, M. (1996) *Introduction to Superconductivity*, McGraw-Hill, New York.
8. Shapiro, S. (1963) Josephson currents in superconducting tunneling: the effect of microwaves and other observations. *Phys. Rev. Lett.*, **11**, 80–82.
9. Benz, S.P. and Burroughs, C.J. (1991) Coherent emission from two-dimensional Josephson junction arrays. *Appl. Phys. Lett.*, **58**, 2162–2164.

10. Kleiner, R., Steinmeyer, F., Kunkel, G., and Müller, P. (1992) Intrinsic Josephson effects in $Bi_2Sr_2CaCuO_8$ single crystals. *Phys. Rev. Lett.*, **68**, 2394–2397.
11. (a) Barone, A. and Paterno, G. (1982) *Physics and Applications of the Josephson Effect*, John Wiley & Sons, Inc., New York; (b) Likharev, K.K. (1986) *Dynamics of Josephson Junctions and Circuits*, Gordon and Breach, Philadelphia, PA; (c) van Duzer, T. and Turner, C.W. (1999) *Principles of Superconductive Devices and Circuits*, 2nd edn, Prentice Hall, Upper Saddle River, NJ; (d) Orlando, T.P. and Delin, K.A. (1991) *Foundations of Applied Superconductivity*, Addison-Wesley, Reading, MA.
12. (a) Schrieffer, J.R., Scalapino, D.J., and Wilkins, J.W. (1963) Effective tunneling density of states in superconductors. *Phys. Rev. Lett.*, **10**, 336–339; (b) Scalapino, D.J., Schrieffer, J.R., and Wilkins, J.W. (1966) Strong-coupling superconductivity. I. *Phys. Rev.*, **148**, 263–279.
13. Giaever, I., Hart, H.R. Jr., and Megerle, K. (1962) Tunneling into superconductors at temperatures below 1°K. *Phys. Rev.*, **126**, 941–948.
14. McMillan, W.L. and Rowell, J.M. (1969) Tunneling and strong-coupling superconductivity, in *Superconductivity* (ed. R.D. Parks), Marcel Dekker, New York.
15. Hipps, K.W. and Mazur, U. (2002) Inelastic electron tunneling spectroscopy, in *Handbook of Vibrational Spectroscopy* (eds J.M. Chalmers and P.R. Griffiths), John Wiley & Sons, Ltd, Chichester.
16. Andreev, A.F. (1964) The thermal conductivity of the intermediate state in superconductors. *Zh. Eksp. Theor. Fiz.*, **46**, 1823–1836; *Sov. JETP*, (1964), **19**, 1228-1231.
17. de Gennes, P.D. and Saint-James, D. (1963) Elementary excitations in the vicinity of a normal metal-superconducting metal contact. *Phys. Lett.*, **4**, 151–152.
18. Tomasch, W.J. (1965) Geometrical resonance in the tunneling characteristics of superconducting Pb. *Phys. Rev. Lett.*, **15**, 672–675.
19. Rowell, J.M. and McMillan, W.L. (1966) Electron interference in a normal metal induced by superconducting contacts. *Phys. Rev. Lett.*, **16**, 453–456.
20. De Lozanne, A. (1999) Scanning probe microscopy of high-temperature superconductors. *Supercond. Sci. Technol.*, **12**, R43–R56.
21. Fulton, T.A. and Dolan, G.J. (1987) Observation of single-electron charging effects in small tunnel junctions. *Phys. Rev. Lett.*, **59**, 109–112.
22. Averin, D.V. and Likharev, K.K. (1991) Single electronics: correlated transfer of single electrons and cooper pairs in systems of small tunnel junctions, in *Mesoscopic Phenomena in Solids* (eds B.L. Altshulter, P.A. Lee, and R.A. Web), Elsevier, Amsterdam.
23. Barner, J.B. and Ruggiero, S.T. (1987) Observation of the incremental charging of Ag particles by single electrons. *Phys. Rev. Lett.*, **59**, 807–810.

1.2.3 Flux Pinning

Stuart C. Wimbush

1.2.3.1 Introduction

The amount of DC electrical current able to be transported without loss (or, in practice, below some small but measurable voltage drop, typically quoted as 1 V over 10 km) by a superconducting wire under a given set of operating conditions (temperature, magnetic field) is the parameter that ultimately determines its technological applicability, and this critical current in turn is determined by the immobilization, or pinning, of magnetic flux lines within the superconductor. The origin of the magnetic flux may be either an applied magnetic field, as exists in motors or generators, or the field generated by the transport current itself (termed the *self-field*) as is the case, for example, in power transmission cables or transformers. Consequently, the existence of a pinning-limited critical current is unavoidable. Likewise, in superconducting electronic devices and in bulk superconductors used as permanent magnets, the prevention of flux motion through pinning is critical in order to reduce noise or to effectively trap an applied magnetic field. This section examines the mechanisms by which magnetic flux lines can be pinned, the different types of pinning centers that have been employed to engineer high critical current superconductors, the measurements able to provide experimental information on flux pinning, and the state-of-the-art flux pinning presently achievable in second generation coated conductors.

1.2.3.2 Flux Lines, Flux Motion, and Dissipation

Flux lines form within a type II superconductor because it is energetically favorable for the material to allow a magnetic field to locally penetrate the bulk to form a mixed state comprising quantized threads of magnetic flux encircled by regions of superconducting material through which spontaneous supercurrents flow so as to screen the field from the bulk of the material, thereby forming a vortex (Figure 1.2.3.1). This enables the superconductivity as a whole to persist to a much higher field than would be possible if the Meissner state of complete flux expulsion were to be maintained (cf. Section 1.1.1), and is the case precisely because the spatial extent of the magnetic penetration in the type II materials exceeds the extent of the disruption to the superconducting state $\kappa = \lambda/\xi > 1/\sqrt{2}$. Thus, by allowing a small volume of material to revert to the normal state, the resulting penetrating magnetic field can be screened over a large volume of superconducting material. The upper critical field $B_{c2} = \Phi_0/2n\xi^2$ at which superconductivity ceases can be expressed intuitively as the field at which the non-superconducting regions overlap, resulting in an entirely normal state material. However, from a technological point of view, both this limiting field and the depairing current that provides an absolute upper limit to the current-carrying capacity of the material are supplanted by stricter limits governed not by the thermodynamic phase transition

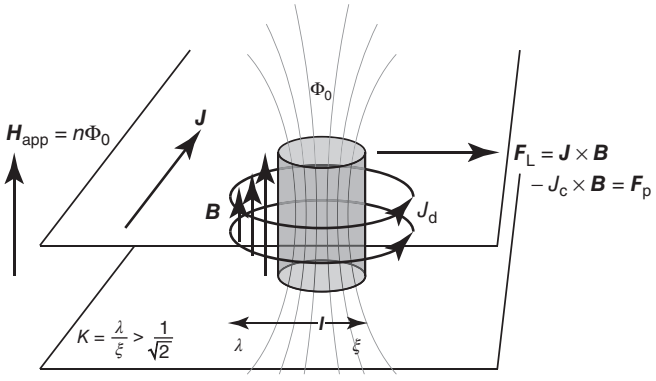

Figure 1.2.3.1 A quantized line of magnetic flux penetrates a type II superconducting slab subjected to an applied magnetic field exceeding its lower critical field. Spontaneous circulating supercurrents form a vortex that screens the field from the bulk of the superconductor. Under the influence of an imposed transport current, the unpinned flux line experiences a force analogous to the Lorentz force that causes it to move, dissipating energy. For this to be prevented, the flux line must be pinned by a countering force that inhibits dissipative motion up to some critical value of the transport current.

from the superconducting to the normal state but rather by energy dissipation within the superconductor caused by motion of the flux lines.

Flux motion occurs as a result of a force analogous to the Lorentz force $\boldsymbol{F}_L = \boldsymbol{J} \times \boldsymbol{B}$ being exerted on the flux lines under the influence of an imposed transport current $\boldsymbol{J}$. The moving flux lines are accelerated until the retarding force due to viscous flow, proportionally opposed to their velocity $\boldsymbol{v}$, matches the Lorentz force. The spatially varying magnetic field of the moving flux lines induces an electric field $\boldsymbol{E} = -\boldsymbol{v} \times \boldsymbol{B}$ in the direction of the transport current. This electric field acts on the normal electrons within the superconductor, dissipating energy through ohmic losses. Since the magnitude of the electric field is likewise proportional to the velocity of the moving flux lines, it will also be proportional to the transport current ($\boldsymbol{E} = \rho_f \boldsymbol{J}$), and the response is therefore indistinguishable from an ohmic resistance. Macroscopically, while remaining in the superconducting state and conducting current through the transport of Cooper pairs, the superconductor will nonetheless exhibit a resistance, termed the *flux flow resistance*. It is therefore the DC supercurrent that can be maintained in the absence of this resistance that dictates the range of practical operation of the superconductor, and this is termed the *critical current*, J_c.

Such a zero-resistance DC transport current can only be established if some means of preventing flux motion is available. Otherwise, the smallest transport current will generate a self-field of some degree, which will penetrate the superconductor in the form of flux lines as soon as it exceeds the lower critical field. Those flux lines will flow unimpeded through the superconductor under the influence of the Lorentz force, generating a flux flow resistance and dissipating energy. Such a situation arises in high-quality single crystals, which have extremely low

J_c values. To overcome this, a force termed the *pinning force* must counter the Lorentz force that is acting to excite the flux lines into motion. The opposition to vortex motion from pinning forces provides a mechanism for the enhancement of J_c, and also introduces our second limiting parameter in the form of the irreversibility field B_{irr} beyond which the number of flux lines present within the superconductor exceeds its capability to effectively pin them all, with the result that the magnetization becomes reversible (flux flowing freely into and out of the superconductor) and J_c drops to zero. Increasing flux pinning in technological materials is an essential endeavor in order to increase the achievable current and field ranges and thus the performance of superconducting machines and devices. The amount of pinning can be increased either by promoting naturally occurring sources of pinning or by introducing new sources, so-called artificial pinning centers.

1.2.3.3 Sources of Flux Pinning

Flux pinning may best be described as the effect of spatial inhomogeneities within the superconductor upon the flux line lattice that forms when mutually repulsive vortex–vortex interactions (resulting from the Lorentz force between the circulating supercurrent J_d of one vortex and the magnetic flux Φ_0 of another) are taken into account. Such inhomogeneities may arise naturally, for example, through local variations in material density, elasticity or electron–phonon coupling strength and the existence of crystalline defects, or they may be introduced artificially through doping, microstructural modification, or the incorporation of foreign bodies. A change in the material density is equivalent to a change in the (chemical) pressure, and will give rise to a local change in the superconducting transition temperature, T_c, as may strain fields and variations in the electron–phonon coupling. Genuine material doping may act to combine several of these effects. The pinning that results is termed δT_c *pinning* [1]. A similar effect occurs upon the inclusion of non-superconducting material, which provides a region of suppressed T_c that may be highly localized or rather extended, depending on the nature of the inclusion; however, such an inclusion also constitutes a material defect that will have a scattering effect on the charge carriers, acting to vary the electronic mean free path, l (δl pinning, formerly termed $\delta\kappa$ *pinning* [2]). In all cases, the result is the same: the creation of a lower energy (preferred) site for vortex occupation.

For maximum effect, the spatial variations must occur on the length scale of either ξ or λ, depending on the nature of the interaction; any larger and the inhomogeneity will not be seen by the superconductor as an inhomogeneity but rather as a distinct phase, any smaller and the effectiveness will be reduced due to the proximity effect. That said, small-scale modifications such as atomic substitutions can create larger-scale inhomogeneities through alterations of the electronic structure or the creation of strain fields, and so on. It is the extent of the inhomogeneity, not the extent of the modification, that matters.

A useful distinction can be drawn between pinning forces operating over the length scale of ξ, termed (vortex) *core pinning*, and those operating over a

length scale of λ, termed *magnetic pinning*. To the former category belong the majority of artificial pinning centers successfully employed to date as well as all common growth defects, while the latter category comprises such natural sources as extended surfaces and pores where the flux entirely enters or exits the superconductor as well as pinning due to vortex–vortex interactions. While vortex–vortex interactions do act to pin vortices, it is important to note that this can only occur if at least some of the vortices are pinned by another source; otherwise, the entire lattice will simply slip through the material. Where some vortices are strongly pinned and others are not, shearing as well as melting of the flux line lattice becomes an effective depinning mechanism. Inherently, magnetic artificial pinning centers will combine both of these types, exerting a core pinning influence through their localized suppression of superconductivity as well as a magnetic pinning effect resulting from their magnetization (see Section 1.2.3.8).

By definition, all of these spatial inhomogeneities constitute defects in the crystal lattice of the superconductor, and so flux pinning is inextricably linked to the defect structure (often termed the *defect landscape*) of the material. As a consequence, defect engineering of technologically relevant materials forms an extensive field of endeavor. It has become common to catalog the available types of pinning defects, which is nothing more than a list of possible crystal defects, and a useful classification is to enumerate them in terms of their dimensionality, as illustrated in Figure 1.2.3.2.

Zero-dimensional (point) defects include foreign (impurity) atoms, atomic substitutions, and vacancies (particularly when referred to the non-stoichiometric oxygen content of the cuprates). These are effective in high temperature superconductors (HTS) due to the short coherence length of the materials, meaning that a variation in stoichiometry over even a single atomic site can have a sufficiently wide sphere of influence to locally suppress the superconducting order parameter.

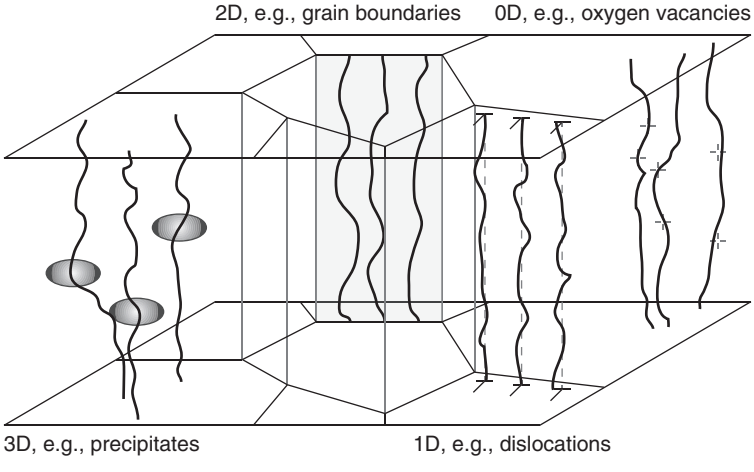

Figure 1.2.3.2 Schematic illustration of the pinning of flux lines by crystalline defects of varying dimensionality.

One-dimensional (line or columnar) defects include dislocations and artificial defects such as the damage tracks resulting from heavy ion, neutron, or proton irradiation. They are a particularly interesting class from the point of view of flux pinning due to their congruence with the form of the flux line itself. Correlation between the defects and the flux lines can lead to extremely strong pinning, with the flux line being pinned along its entire length. As an example, screw dislocations arise naturally during the growth of yttrium barium copper oxide (YBCO) thin films, forming part of the growth mode of the material and contributing strongly to its high J_c even before microstructural modification. A heavy focus is applied to engineering artificial pinning centers of this type in an attempt to smooth out the naturally occurring J_c anisotropy of the HTS materials. Since high-energy irradiation techniques are impractical for industrial production, the emphasis is on self-assembly processes of second-phase inclusions, although low-energy ion implantation methods have been employed with some success in introducing clusters of atoms to act as volume pinning centers [3].

Two-dimensional (planar) defects include grain boundaries, twin planes, stacking faults, and antiphase boundaries. Grain boundaries are important pinning centers in low temperature superconductors (LTS) and MgB_2, while twin planes and stacking faults are particularly prevalent in second generation coated conductors due to the orthorhombic structure of the YBCO crystal promoting twinning and the close proximity of the equilibrium phase formation conditions of Y123 and Y124 encouraging stacking fault formation to accommodate compositional variations. The low angle grain boundaries in HTS are better viewed as "dislocation fences" of one-dimensional defects than as continuous planar defects, due to the short coherence lengths. Antiphase boundaries tend to be of limited effectiveness due to their restricted spatial extent, tendency to heal out during growth by combination with stacking faults, and the fact that superconductivity is only somewhat suppressed by them. Planar defects can also provide correlated pinning, although with the risk of channeling of the flux lines along the planes [4].

Three-dimensional (volume) defects generally constitute secondary (impurity) phases, precipitates, or inclusions as well as voids (porosity). The similarity to point defects is apparent, although volume defects can also be effective in high coherence length materials such as LTS or at temperatures close to T_c. The majority of work on artificial pinning centers focuses on the intentional introduction of non-superconducting secondary phases intended to promote pinning. The requirements on these are that they should remain segregated from the superconducting matrix, and that they should be of a size appropriate to provide effective pinning while not consuming too great a volume fraction of the material (which then becomes unavailable for supercurrent transport). The most effective pinning arises from inclusions the size of ξ, and in HTS materials, this implies nano-engineering.

1.2.3.4 Flux Pinning in Technological Superconductors

Having enumerated the available sources of pinning in general terms, we now look, by way of example, at the specifics of flux pinning in the technological superconductors. Only a small subset of the many known superconductors has been developed for commercial application: Nb – Ti and Nb_3Sn of the LTS materials and Bi-2223 and YBCO of the HTS materials, with MgB_2 now also fighting to enter the fold. Each of these has decidedly different flux pinning characteristics.

The ductile alloy Nb – Ti is formed into a wire by repeated bundling, drawing, and annealing of rods of the material embedded within a stabilizing Cu matrix to form a filamentary conductor. In this material, pinning occurs when flux lines interact with dislocation tangles created during the drawing process. These regions of dense dislocations decrease the electronic mean free path, resulting in δl pinning. The microstructure of the filaments comprises elongated Nb – Ti grains with non-superconducting Ti precipitates lying along the filaments. The radial Lorentz force therefore drives flux lines across the grain boundaries and through the non-superconducting precipitates.

The A15-structure compound Nb_3Sn is initially prepared in a similar way, this time using rods of pure Nb placed within a bronze (Cu – Sn) matrix. This is drawn to again produce a filamentary conductor which is then heated to allow the Nb to post-react with Sn leached from the bronze. Production in this sequence is necessary due to the brittleness of the resulting intermetallic phase limiting subsequent processing. The post-reaction process results in columnar grains of superconductor oriented perpendicular to the filament. Consequently, the Lorentz force drives some of the flux lines along, rather than across, the grain boundaries, causing the flux line lattice to shear and thereby reducing the effectiveness of the pinning.

In the high temperature superconductors, the critical current is limited by two effects. The first, due to the small coherence length, results in any large angle grain boundary forming a weak link, severely limiting current flow [5]. However, careful materials processing has today virtually eliminated this type of grain boundary from technological materials, and since this effect is not pinning related, it shall not be considered further here. Once weak links have been eliminated, the critical current is again determined by flux pinning.

The "first generation" HTS material, Bi-2223, is fabricated by a powder-in-tube technique, whereby the precursor powder is packed into Ag tubes which are bundled and drawn before reaction to form the superconducting phase. A filamentary conductor again results, with a final rolling deformation into a tape serving to induce the texture required to eliminate weak links. In contrast, the "second generation" HTS material based on YBCO must be fabricated as a thin film "coated" conductor in order to achieve the required texturing, due to its less anisotropic crystal structure preventing mechanical texturing. In both of these layered, textured materials, a form of pinning termed *intrinsic* pinning arises due to the intrinsic inhomogeneity of the material in passing through the crystal planes commonly considered to be insulating that separate the superconducting CuO_2 planes. This form of pinning is only effective for flux lines (and therefore applied fields) lying in the plane of the material, leading to a sharp increase in the critical current for high

fields (where only the most prevalent pinning centers are still effective) applied in-plane at low temperatures (where the coherence length is small, comparable to the planar spacing, and the flux lines are rigid).

In seeking to improve the performance of the second generation YBCO conductors, so-called "artificial" pinning centers have been introduced. In contrast to the microstructural modifications applied to the formation of the other classes of superconducting wire to maximize performance, these are non-superconducting secondary (impurity) phases intentionally introduced with the aim of providing an enhancement in J_c through pinning that outweighs their detriment through the reduction in the superconducting cross-section of the wire. The most successful, effective, and widely studied artificial pinning center for second generation coated conductors identified to date is the perovskite dielectric $BaZrO_3$. Its structural similarity to YBCO as well as its oxidic nature and the fact that it adds only a single, benign, element into the mix are all points in its favor. Zr was already known not to substitute into the YBCO lattice, while the material as a whole was well known to be compatible with YBCO since it was commonly used as a crucible for single crystal growth. It was also expected that its high melting point would correspond to slow growth kinetics, resulting in the desirably small size of inclusions critical for effective pinning in HTS. The initial report [6] of $BaZrO_3$ incorporation in an YBCO thin film in the form of nanoparticles of size ~10 nm provided an immediate J_c enhancement of up to a factor 5 in samples grown on both single crystal and technical substrates across the entire field range. Furthermore, in the case of *in situ* film growth techniques such as pulsed laser deposition and chemical vapor deposition, the strain created by the epitaxial

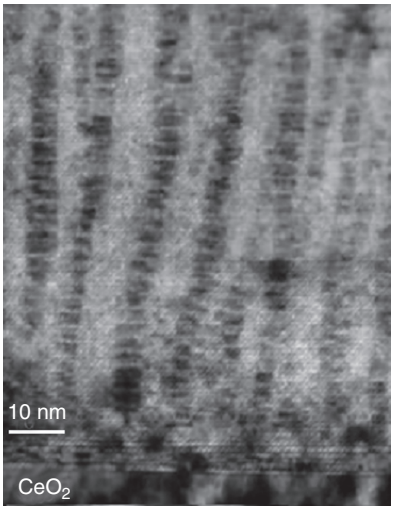

Figure 1.2.3.3 Epitaxial strain-induced self-assembly of individual $BaZrO_3$ nanoparticles in YBCO to form chains aligned with the film growth direction (the so-called "bamboo" microstructure), acting as one-dimensional correlated artificial pinning centers. (Adapted from Ref. [7]. Reproduced with permission of AIP Publishing LLC.)

growth of the lattice-mismatched nanoparticles within the YBCO matrix leads to a self-assembly of chains of nanoparticles into nanocolumns aligned with the growth direction (Figure 1.2.3.3), resulting in a much coveted enhancement in pinning correlated with that direction acting to balance out the anisotropic pinning due to the planar structure of the superconductor. In contrast, where *ex situ* film growth occurs, as is the case for chemical solution deposition, this epitaxial strain-induced self-assembly cannot occur, and instead a general reduction in J_c anisotropy associated with dispersed nanoparticle pinning is obtained. Thus, even for the same sample composition, ultimately, it is the microstructure of the particular sample that determines the pinning response.

Little further progress has been made in terms of the discovery of improved pinning species since this earliest attempt at artificial pinning center creation. However, an additional contender has emerged in the form of $BaHfO_3$ [8]. The need for further improvement arises in the move to thicker films, where it is observed that the nanocolumns of $BaZrO_3$ bend or "splay" as growth proceeds, reducing the effectiveness of their correlated pinning. $BaHfO_3$ nanocolumns, in contrast, maintain their orientation throughout the film thickness as well as being smaller in size due to a further increased melting point. Hf is similarly inert to Zr in YBCO. Some also suggest that the enhancements due to $BaHfO_3$ pinning are maintained to lower temperatures (see Section 1.2.3.7), although this is disputed with some questioning whether $BaHfO_3$ will prove truly superior to $BaZrO_3$, or whether they are in fact just very similar.

MgB_2 wires are also prepared by a powder-in-tube method with both pre-reaction (*ex situ*) and post-reaction (*in situ*) methods presently being employed. Multiband superconductivity in MgB_2 allows for a large enhancement in the upper critical field to be achieved through carbon doping in place of boron, commonly achieved through the addition of malic acid [9], enabling improved in-field performance through flux pinning. The primary pinning mechanism in MgB_2 is through the dense three-dimensional network of grain boundaries resulting from the solid state processing. The grain size, and thereby the effectiveness and density of this pinning, is tailored through modifications to the processing parameters. Pinning by nanoparticle artificial pinning centers is also commonly employed, with the most effective addition to date being SiC [10], which acts to combine the benefits of nanoparticle addition in the form of Mg_2Si with carbon doping during the reaction process.

1.2.3.5 Experimental Determination of Pinning Forces

It is a relatively straightforward matter to determine experimentally the magnitude of the pinning force $|\boldsymbol{F}_p(T, B)| = J_c(T, B)B$ in a given sample under a range of operating conditions. Fietz and Webb [11] were the first to show that the pinning force values so obtained scale rather simply with both temperature and field for a variety of Nb–Ti alloys of widely varying κ. Kramer [12] extended this analysis to other superconductors, most notably Nb_3Sn, and ultimately Dew-Hughes [13]

generalized the function to the form commonly employed today for all superconductor materials:

$$F_p = J_c B \propto B_{irr}^{p+q} b^p (1-b)^q \quad \text{with} \quad b = \frac{B}{B_{irr}} \tag{1.2.3.1}$$

where the temperature dependence is entirely contained within the temperature dependence of the irreversibility field B_{irr}. The increasing b^p part of the curve describes the increase in total pinning force as the density of pinned flux lines increases with the applied field until at the peak a "matching field" is reached where all available strong pinning sites are occupied. Beyond this, the further increasing applied field results in the $(1-b)^q$ diminishment in the pinning force as the superfluid density decreases. The details of the distinct scaling laws thus derived (different values of p and q) have been linked to specific mechanisms of flux pinning thought to be operating, and explained through the similar scaling of materials properties related to those mechanisms. The pinning force curves of different technological materials are found to take on characteristically different forms (Figure 1.2.3.4), and it is therefore considered likely that the curves contain definitive information regarding the contribution of the particular material microstructure to flux pinning. For example, the $b(1-b)$ form observed for Nb–Ti is associated with transverse depinning of flux lines from the interface of superconducting and non-superconducting regions, while the $b^{1/2}(1-b)^2$ form common to Nb_3Sn is identified with longitudinal shearing of the flux line lattice. In HTS materials, more extreme forms of the behavior are observed, peaking at much lower reduced field values and diminishing more rapidly in field.

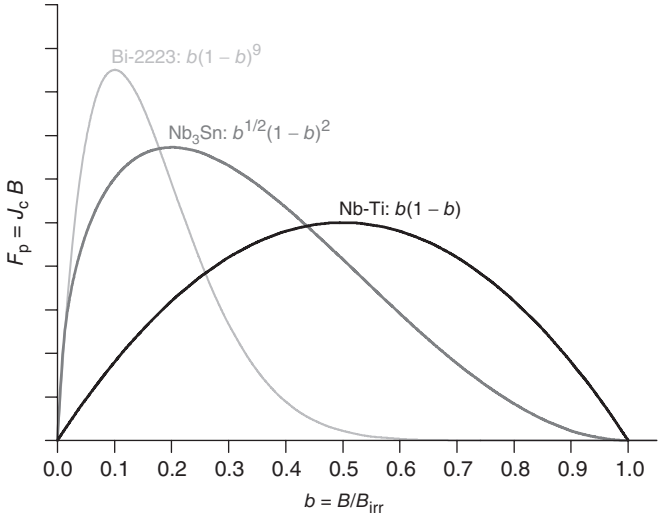

Figure 1.2.3.4 Schematic pinning force plots (as a function of the reduced applied field) representative of the pinning commonly observed in different technological superconductors. The characteristically different functional form of the curves for the different materials is expressed in terms of the generalized Kramer formula, Eq. (1.2.3.1).

1.2.3.6 Regimes of Flux Motion

We have already described the low-pinning limiting case of flux flow, where the Lorentz force fully overcomes the pinning force and the only resistance to flux motion is the viscous drag on the flux lines. This is the inevitable consequence of a sufficiently high current or a sufficiently high field, and is also the regime that most commonly arises in close to perfect single crystals. At the other extreme, we may consider the idealized case of extremely strong flux pinning or a close to negligible transport current. In this regime, the pinning forces dominate, although even here, thermal activation, particularly at the typical operating temperatures of the HTS materials, will lead to so-called "thermally activated flux flow" in which individual flux lines will hop statistically from one pinning site to the next. (It is important to note that the persistent current experiments of S. C. Collins at MIT, in which supercurrents were shown to remain undiminished over a period of years, were performed on *type I* superconductors, where flux penetration does not occur.)

In an intermediate regime, the combination of a significant transport current and thermal activation leads to a directed flux creep of particular significance in the HTS materials. Here, not only the higher operation temperatures but also the reduced core energy (related to ξ^3) stemming from the small coherence length mean that even at temperatures as low as 10 K, flux motion, and consequent dissipation due to creep can be significant. In LTS, in contrast, flux creep can be held to a manageably low level, allowing the operation, for example, of highly stable gigahertz class NMR magnets formed from type II LTS materials, a possibility that does not exist for HTS.

These three regimes of flux motion are illustrated schematically in Figure 1.2.3.5.

1.2.3.7 Limitations on Core Pinning Efficacy

We have seen how the depairing current is supplanted by the depinning current as the limiting factor governing the operation of technological superconductors. Nonetheless, the depairing current (at which the kinetic energy of the charge carriers constituting the current exceeds the binding energy of the Cooper pairs), as the more fundamental limit, is still held up as a goal for efforts aimed at increasing flux pinning. However, since the two are determined by entirely different mechanisms, there is no reason to suppose that their values should coincide. Indeed, it could have been the case that depairing was the limiting mechanism for performance, with depinning only occurring at higher transport currents than could ever be achieved. However, it has been recognized for some time [14, 15] that this is not the case, although sight of this fact appears to have been lost in regard to the HTS materials [16].

If the depairing current were to flow, it would produce a Lorentz force per unit length of flux line given by:

$$f_d = J_d \Phi_0 = \frac{4 B_c \Phi_0}{3\sqrt{6}\mu_0 \lambda} \tag{1.2.3.2}$$

In the case of core (ξ) pinning, the maximum pinning force is obtained when each vortex is pinned along its entire length. This requires an idealized microstructure

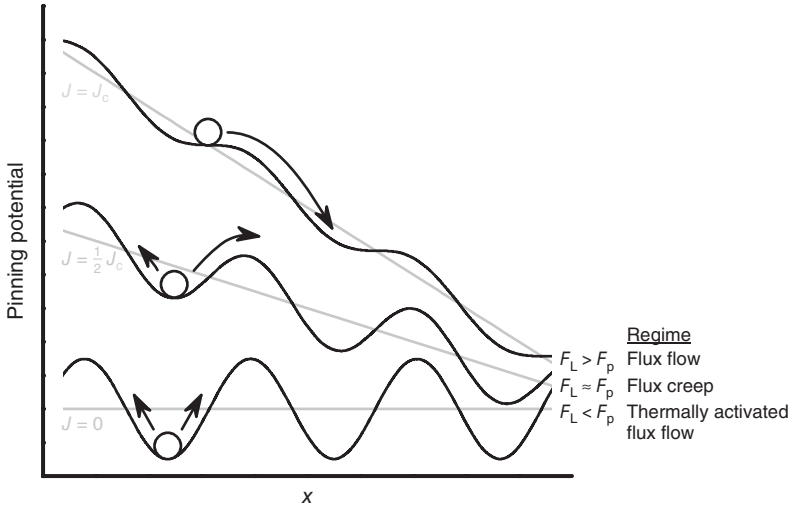

Figure 1.2.3.5 Schematic pinning potentials for different regimes of flux motion. A generic pinning site is represented as a parabolic potential well, superimposed upon a series of which is a linear potential gradient due to the Lorentz force arising from the transport current. When the Lorentz force overcomes the pinning force, the flux lines flow freely. Below this, thermally activated regimes of flux creep and flux flow occur.

comprising cylindrical non-superconducting regions of radius $\sim\xi$ oriented parallel to the applied field in an arrangement corresponding to that of the flux line lattice. If this were achieved, the saving in condensation energy per unit length of flux line would be

$$\varepsilon_{\text{core}} = -\frac{1}{2}\frac{B_c^2}{\mu_0}\pi\xi^2 \tag{1.2.3.3}$$

producing a potential well over a length scale $\sim\xi$ that would result in a pinning force per unit length of flux line of

$$f_p^{\text{core}} = -\nabla\varepsilon_{\text{core}} \approx \frac{1}{2}\frac{B_c^2}{\mu_0}\pi\xi \tag{1.2.3.4}$$

Using $B_c = \Phi_0/2\sqrt{2}\pi\lambda\xi$, the ratio of the optimal core pinning force to the depairing Lorentz force is thus

$$\frac{f_p^{\text{core}}}{f_d} = \frac{1}{2}\frac{B_c^2}{\mu_0}\pi\xi\frac{3\sqrt{6}\mu_0\lambda}{4B_c\Phi_0} = \frac{3\sqrt{3}}{16} \approx 0.32 \tag{1.2.3.5}$$

A more detailed calculation by Matsushita [17] taking into account the precise geometry of the flux line brings this down slightly to a value of 0.28, confirming that the maximum critical current achievable through core pinning is around 30% of the depairing current. In practice, such an idealized microstructure is impossible to achieve, would occupy a significant fraction of the sample volume with

non-superconducting material (reducing the effective J_c), and in any case would be ideal for only a single value of magnetic field applied in a particular direction. Consequently, actual critical currents in the commercial LTS materials lie around one-tenth of the optimal value, or one-thirtieth of the depairing current.

HTS materials are surprisingly similar in their performance, and it is perhaps not surprising then that performance gains through pinning modification have stalled. For YBCO at 77 K, 0 T, $J_d \approx 30\,\mathrm{MA\,cm^{-2}}$ [16]. Therefore, core pinning alone cannot be expected to achieve a J_c higher than about $9\,\mathrm{MA\,cm^{-2}}$, which is close to what has been observed (and never exceeded) experimentally [18]. At low fields, J_c lies within an order of magnitude of the depairing current, better than has been achieved in LTS. In-field, there remains room for improvement ($J_c(B)$ decays more rapidly than $J_d(B)$), but the challenge is one of obtaining an extremely high density of correctly spaced near-perfect pinning centers, and any further gains to be had must lie in increasing the irreversibility field through improved pinning at high fields (>3 T). At low temperatures, the requirement for perfection becomes more stringent as the flux lines become more rigid, possibly explaining the seeming ineffectiveness of presently engineered core pins at the temperatures (20–30 K) of interest for high-performance in-field applications. Hard-won performance gains at 77 K vanish completely when the same sample is cooled to 20 K. Indeed, a pinning-engineered sample that performs better at 77 K than its counterpart may in fact be found to perform *worse* at 20 K [19]. Presently, there is no known species of artificial pinning center that can reliably be said to improve low temperature performance, and this is unquestionably the next great challenge for defect engineering of HTS materials. Performance tweaks are still being achieved, but generally performance lies around where we can expect it to reach, between one-tenth and one-hundredth of the depairing current. Any further substantial pinning gain must be based on an alternative pinning mechanism.

1.2.3.8 Magnetic Pinning of Flux Lines

Magnetic (λ) pinning offers a hitherto untapped opportunity to raise the depinning critical current beyond what can be achieved through core pinning alone, and to attain values closer to the depairing current. The simplest example of magnetic pinning arises when a high density of flux lines is introduced, and they form themselves into a lattice, the so-called vortex glass phase. Vortex–vortex interactions typically encourage this to be hexagonal in shape, and if the lattice is sufficiently rigid, it suffices to pin a single vortex by core pinning and others nearby will be held in place by those interactions. However, it is equally possible to conceive of artificial magnetic pinning in which the magnetic interaction of an appropriate artificial pinning center is utilized to provide a magnetic pinning contribution *in addition to* its core pinning effect. The slow take-up of magnetic pinning lies in the challenge of incorporating ferromagnetic material into the microstructure of the superconductor without detriment to the superconductivity through pair breaking interactions.

The claim is often made that magnetic pinning offers an advantage over core pinning through the greatly increased strength of the magnetic Zeeman energy

term compared to the condensation energy:

$$\varepsilon_{\text{mag}} = -\frac{1}{2}\int_A \boldsymbol{M}\cdot\boldsymbol{B}\ dA = \frac{1}{2}M\Phi_0 \tag{1.2.3.6}$$

which is limited only by the magnetization of the pinning center, and might be expected to reach a value several orders of magnitude greater than the core pinning energy for a strong ferromagnet. However, it must be remembered that due to the magnetic interaction occurring over the length scale of λ instead of ξ, the pinning *force* may in fact not be much greater, or may even be less than the core pinning force. The magnetic pinning force depends on the ratio of the magnetization of the pinning site to the thermodynamic critical field, which is of the order of 1 T in the technological materials, very similar to that of available strong ferromagnets:

$$f_{\text{p}}^{\text{mag}} = -\nabla\varepsilon_{\text{mag}} \approx \frac{M\Phi_0}{2\lambda} = 2\sqrt{2}\frac{\mu_0 M}{B_{\text{c}}}f_{\text{p}}^{\text{core}} \tag{1.2.3.7}$$

where we have again made use of the relation $B_{\text{c}} = \Phi_0/2\sqrt{2}\pi\lambda\xi$.

Nonetheless, the possibility of magnetic pinning remains attractive not only because its effects are *additive* to those of core pinning, but also due to the potential existence of more exotic interaction mechanisms such as field compensation effects [20] or a reduction in the Lorentz force experienced by the pinned flux line [21] that may serve to lift the depinning limit to J_{c} altogether.

1.2.3.9 Flux Pinning Anisotropy

In general, the macroscopic pinning force resulting from a given sample microstructure depends not only on the applied field, but also on the field angle with respect to the sample, and attempts have been made to provide similar scaling rules for the angle dependence of the pinning as for the field dependence. The most popular of these was introduced by Blatter *et al.* [22] who proposed the field angle scaling law:

$$\widetilde{B} = \varepsilon_\theta B \quad \text{with} \quad \varepsilon_\theta^2 = \cos^2\theta + \varepsilon^2\sin^2\theta \tag{1.2.3.8}$$

for a field applied at an angle θ to the c-axis, where $\varepsilon^2 = m_{ab}/m_c$ is the electronic mass anisotropy of the superconductor. By scaling the applied field values in this way, dependent on their angle, and choosing an appropriate value of ε, the pinning force curves for different field angles can be made to coincide (Figure 1.2.3.6). In the usual interpretation, the pinning force variation described by the universal curve is ascribed to electronic mass anisotropy effects, while the deviations are explained by microstructure-related pinning, in this case a significant additional in-plane component resulting from intrinsic pinning due to the layered structure [23]. Under this interpretation, the ε value that provides the most consistent scaling of the data is directly associated with the electronic mass anisotropy of the superconductor [24]; however, where unfeasibly low ε values have been obtained from such an analysis, the concept of an *effective* electronic mass anisotropy has been introduced where the reduction in anisotropy is attributed to

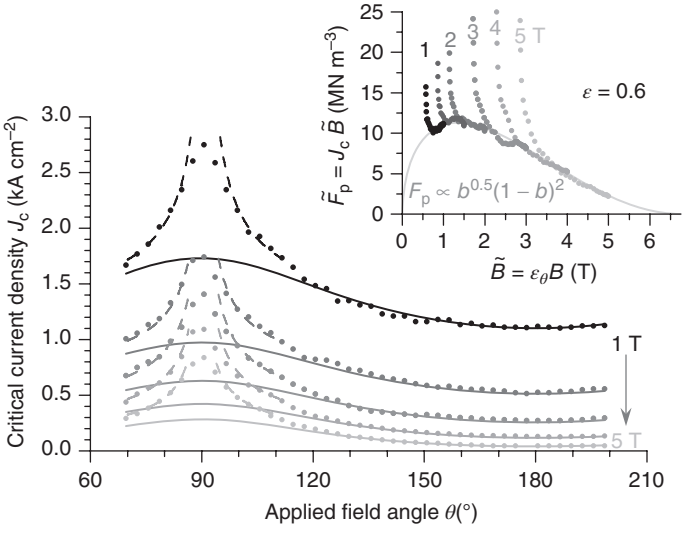

Figure 1.2.3.6 Blatter scaling of $J_c(\theta)$ for a clean $Ba(Fe_{1-x}Co_x)_2As_2$ film at 15 K under various applied fields, showing the experimental data and the angular J_c variation ascribed to electronic anisotropy (solid lines) and intrinsic pinning (broken lines). The inset shows the combined pinning force plot of the scaled datasets. Deviations from the scaled universal curve are due to correlated pinning. (Data from Ref. [23].)

a quasi-isotropic pinning force resulting from nanoscale inhomogeneous strain fields that act to inhibit Cooper pair formation [25].

1.2.3.10 Maximum Entropy Treatment of Flux Pinning

To date, the most comprehensive framework proposed for modeling the general experimental results of flux pinning studies is a method based around a maximum entropy derivation of the effects of statistical populations of pinning defects [26]. A consistent mathematical approach is able to provide formal derivations of the commonly used empirical relations:

$$J_c(t) \propto (1-t)^p \quad \text{with} \quad t = \frac{T}{T_c} \tag{1.2.3.9}$$

$$F_p(b) \propto b^\alpha (1-b)^{\beta-1} \quad \text{with} \quad b = \frac{B}{B_{irr}} \tag{1.2.3.10}$$

arising from the Ginzburg–Landau theory [27] and initially proposed by Kramer [12], respectively. In particular, it provides the generalization of the fixed exponents $p = 3/2$, $\alpha = 1/2$, and $\beta = 3$ occurring in those theories that is commonly applied empirically without justification. For the geometrical dependence of J_c on the applied field angle, it provides three fundamental components that are summed to represent different statistically significant combinations of pinning defect populations within the sample:

$$\text{Uniform } J_c(\psi) = \frac{J_0}{\pi} \tag{1.2.3.11a}$$

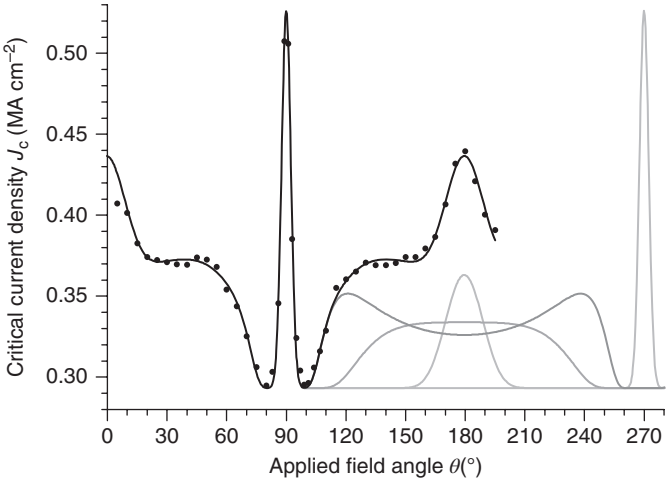

Figure 1.2.3.7 Maximum entropy modeling of $J_c(\theta)$ for a YBCO coated conductor at 65 K, 6 T, showing the experimental data and the resulting fit on the left, and the individual pinning components on the right. In addition to a uniform component, this dataset features a distinct *ab*-centered angular Gaussian describing the intrinsic pinning and three statistically distinguishable *c*-axis angular Gaussian contributions to the out-of-plane pinning.

$$\text{Angular Gaussian } J_c(\psi) = \frac{J_0}{\sqrt{2\pi}\sigma\sin^2\psi}\exp\left(-\frac{1}{2\sigma^2\tan^2\psi}\right) \qquad (1.2.3.11b)$$

$$\text{Angular Lorentzian } J_c(\psi) = \frac{J_0}{\pi}\frac{\gamma}{\cos^2\psi + \gamma^2\sin^2\psi} \qquad (1.2.3.11c)$$

An example of the application of this modeling to typical results obtained on pinning-optimized YBCO coated conductors is shown in Figure 1.2.3.7. It must be noted that the method of the previous section would fail to provide any meaningful interpretation of this dataset, where microstructure-based pinning completely dominates the response.

The same maximum entropy functions have been shown equally capable of describing the in-plane (variable Lorentz force) $J_c(\phi)$ variation as the out-of-plane $J_c(\theta)$ variation, and are also able to accurately model the effects of oblique defect structures such as those obtained on inclined substrates or through heavy ion irradiation. A further development of the same mathematical framework has been shown to have physical significance in describing vortex channeling along planar pinning defects.

References

1. Blatter, G., Feigel'man, M.V., Geshkenbein, V.B., Larkin, A.I., and Vinokur, V.M. (1994) Vortices in high-temperature superconductors. *Rev. Mod. Phys.*, **66**, 1125–1388.
2. Hampshire, R.G. and Taylor, M.T. (1972) Critical supercurrents and the pinning of

vortices in commercial Nb–60 at% Ti. *J. Phys. F: Met. Phys.*, **2**, 89–106.
3. Matsui, H., Ogiso, H., Yamasaki, H., Kumagai, T., Sohma, M., Yamaguchi, I., and Manabe, T. (2012) 4-fold enhancement in the critical current density of $YBa_2Cu_3O_7$ films by practical ion irradiation. *Appl. Phys. Lett.*, **101**, 232601.
4. Palau, A., Durrell, J.H., MacManus-Driscoll, J.L., Harrington, S., Puig, T., Sandiumenge, F., Obradors, X., and Blamire, M.G. (2006) Crossover between channeling and pinning at twin boundaries in $YBa_2Cu_3O_7$ thin films. *Phys. Rev. Lett.*, **97**, 257002.
5. Dimos, D., Chaudhari, P., and Mannhart, J. (1990) Superconducting transport properties of grain boundaries in $YBa_2Cu_3O_7$ bicrystals. *Phys. Rev. B*, **41**, 4038–4049.
6. MacManus-Driscoll, J.L., Foltyn, S.R., Jia, Q.X., Wang, H., Serquis, A., Civale, L., Maiorov, B., Hawley, M.E., Maley, M.P., and Peterson, D.E. (2004) Strongly enhanced current densities in superconducting coated conductors of $YBa_2Cu_3O_{7-x}$ + $BaZrO_3$. *Nat. Mater.*, **3**, 439.
7. Yamada, Y., Takahashi, K., Kobayashi, H., Konishi, M., Watanabe, T., Ibi, A., Muroga, T., Miyata, S., Kato, T., Hirayama, T., and Shiohara, Y. (2005) Epitaxial nanostructure and defects effective for pinning in $Y(RE)Ba_2Cu_3O_{7-x}$ coated conductors. *Appl. Phys. Lett.*, **87**, 132502.
8. Hänisch, J., Cai, C., Stehr, V., Hühne, R., Lyubina, J., Nenkov, K., Fuchs, G., Schultz, L., and Holzapfel, B. (2006) Formation and pinning properties of growth-controlled nanoscale precipitates in $YBa_2Cu_3O_{7-d}$/transition metal quasi-multilayers. *Supercond. Sci. Technol.*, **19**, 534.
9. Kim, J.H., Zhou, S., Hossain, M.S.A., Pan, A.V., and Dou, S.X. (2006) Carbohydrate doping to enhance electromagnetic properties of MgB_2 superconductors. *Appl. Phys. Lett.*, **89**, 142505.
10. Dou, S.X., Soltanian, S., Horvat, J., Wanga, X.L., Zhou, S.H., Ionescu, M., Liu, H.K., Munroe, P., and Tomsic, M. (2002) Enhancement of the critical current density and flux pinning of MgB_2 superconductor by nanoparticle SiC doping. *Appl. Phys. Lett.*, **81**, 3419–3421.
11. Fietz, W.A. and Webb, W.W. (1969) Hysteresis in superconducting alloys—temperature and field dependence of dislocation pinning in niobium alloys. *Phys. Rev.*, **178**, 657–667.
12. Kramer, E.J. (1973) Scaling laws for flux pinning in hard superconductors. *J. Appl. Phys.*, **44**, 1360–1370.
13. Dew-Hughes, D. (1974) Flux pinning mechanisms in type II superconductors. *Philos. Mag.*, **30**, 293.
14. Hampshire, D.P. (1998) A barrier to increasing the critical current density of bulk untextured polycrystalline superconductors in high magnetic fields. *Physica C*, **296**, 153–166.
15. Dew-Hughes, D. (2001) The critical current of superconductors: an historical review. *Low Temp. Phys.*, **27**, 713–722.
16. Sarrao, J. (ed) (2006) *Basic Research Needs for Superconductivity*, US Department of Energy Office of Science.
17. Matsushita, T. (2007) *Flux Pinning in Superconductors*, Springer.
18. Foltyn, S.R., Civale, L., MacManus-Driscoll, J.L., Jia, Q.X., Maiorov, B., Wang, H., and Maley, M. (2007) Materials science challenges for high-temperature superconducting wire. *Nat. Mater.*, **6**, 631–642.
19. Selvamanickam, V., Yao, Y., Chen, Y., Shi, T., Liu, Y., Khatri, N.D., Liu, J., Lei, C., Galstyan, E., and Majkic, G. (2012) The low-temperature, high-magnetic-field critical current characteristics of Zr-added $(Gd,Y)Ba_2Cu_3Ox$ superconducting tapes. *Supercond. Sci. Technol.*, **25**, 125013.
20. Moshchalkov, V.V., Golubovic, D.S., and Morelle, M. (2006) Nucleation of superconductivity and vortex matter in hybrid superconductor/ferromagnet nanostructures. *C. R. Phys.*, **7**, 86–98.
21. Blamire, M.G., Dinner, R.B., Wimbush, S.C., and MacManus-Driscoll, J.L. (2009) Critical current enhancement by Lorentz force reduction in superconductor–ferromagnet nanocomposites. *Supercond. Sci. Technol.*, **22**, 025017.

22. Blatter, G., Geshkenbein, V.B., and Larkin, A.I. (1992) From isotropic to anisotropic superconductors: a scaling approach. *Phys. Rev. Lett.*, **68**, 875–878.
23. Hänisch, J., Iida, K., Haindl, S., Kurth, F., Kauffmann, A., Kidszun, M., Thersleff, T., Freudenberger, J., Schultz, L., and Holzapfel, B. (2011) J_c scaling and anisotropies in Co-doped Ba-122 thin films. *IEEE Trans. Appl. Supercond.*, **21**, 2887–2890.
24. Civale, L., Maiorov, B., Serquis, A., Willis, J.O., Coulter, J.Y., Wang, H., Jia, Q.X., Arendt, P.N., MacManus-Driscoll, J.L., Maley, M.P., and Foltyn, S.R. (2004) Angular-dependent vortex pinning mechanisms in $YBa_2Cu_3O_7$ coated conductors and thin films. *Appl. Phys. Lett.*, **84**, 2121–2123.
25. Llordés, A., Palau, A., Gázquez, J., Coll, M., Vlad, R., Pomar, A., Arbiol, J., Guzmán, R., Ye, S., Rouco, V., Sandiumenge, F., Ricart, S., Puig, T., Varela, M., Chateigner, D., Vanacken, J., Gutiérrez, J., Moshchalkov, V., Deutscher, G., Magen, C., and Obradors, X. (2012) Nanoscale strain-induced pair suppression as a vortex-pinning mechanism in high-temperature superconductors. *Nat. Mater.*, **11**, 329–336.
26. Long, N.J. (2013) Maximum entropy distributions describing critical currents in superconductors. *Entropy*, **15**, 2585–2605.
27. Ginzburg, V.L. and Landau, L.D. (1950) On the theory of superconductivity. *Zh. Eksp. Teor. Fiz.*, **20**, 1064; In English in Landau, L.D. (1965) *Collected Papers*, Pergamon Press, Oxford, p. 546.

1.2.4
AC Losses and Numerical Modeling of Superconductors

Francesco Grilli and Frederic Sirois

1.2.4.1 Introduction

Type-II superconductors can carry DC current without dissipation, but they do exhibit energy dissipation when they carry AC current or when they are subjected to AC magnetic field. This is because the magnetic field penetrates in the form of discrete flux lines (or vortices) that get pinned to the superconductor material; when there is a change of magnetic field (as in an AC cycle), the flux distribution inside the superconductor material has to rearrange: the movement of magnetic flux induces an electric field, which in turn creates dissipation because this electric field induces currents in the normal conducting regions associated with the core of each vortex. Dissipation occurs whenever there is a variation of the magnetic flux, so the term *AC losses* is generally used for all the situations where the magnetic field changes over time, for example, during the current ramp of a magnet. This kind of energy dissipation is referred to as *hysteresis loss*.[1)]

Technical superconductors are composed of several materials, including metallic and sometimes magnetic parts: as a consequence, they are affected by additional loss contributions (such as eddy current, resistive, coupling, and magnetic losses), which can become important and in some cases largely exceed the hysteretic losses. In multifilamentary superconductors, coupling losses are caused by the current induced by external magnetic fields and flowing from one filament to the other via the normal metal in between; effective ways to reduce them include filament twisting and resistive barriers around the filaments. Eddy current losses can be reduced by increasing the stabilizer's resistivity.

1.2.4.2 General Features of AC Loss Characteristics

Throughout this chapter, we maintain the distinction between *transport* and *magnetization* losses to identify the dissipation caused by transport current and external magnetic field, respectively. This distinction is merely of practical nature because the mechanism responsible for the hysteresis losses inside superconductors (i.e., the movement of magnetic flux) is the same in both cases.

Hysteresis losses strongly depend on the amplitude of the current or the applied field. The transport losses typically increase with the third or fourth power of the applied current (depending on the superconductor's shape) for currents below I_c, then they increase even more rapidly due to flux-flow dissipation. At sufficiently high currents, some of the current starts flowing in the metallic parts of the conductor, giving rise to a resistive contribution. The magnetization losses too increase rapidly with the amplitude of the field (third or fourth power), then when the field fully penetrates the superconductor, they increase less rapidly, typically

1) Other loss mechanisms occur in superconductors, such as the response of normal electrons and the losses associated to the Meissner state. However, they are important only at very high frequencies and at extremely low fields, and they will not be addressed here.

with the first power of the field. More details on the dependence of the hysteresis losses on the current and field amplitude are given in Section 1.2.4.4 for different geometries.

Generally, the hysteresis losses (per cycle) have a feeble dependence on frequency, and the observed frequency dependence of measured losses is usually due to the eddy current or resistive losses occurring in the metal parts. A model for loss dissociation was proposed in Ref. [1], where the dissipated power is split into resistive, hysteretic, and eddy current contributions, each with a different dependence on the frequency:

$$P_{\text{tot}} = \underbrace{P_{\text{res}}}_{RI_{\text{rms}}^2} + \underbrace{P_{\text{hyst}}}_{fQ_{\text{hyst}}} + \underbrace{P_{\text{eddy}}}_{\propto f^2} \tag{1.2.4.1}$$

An example of the identification of the three components on measured data is shown in Figure 1.2.4.1a. In general, the dominance of one component on the others depends on several factors, related to the properties of the materials and on the operating conditions (frequency and amplitude of the field and current). Sometimes other loss components become important: for example, coupling losses or losses in magnetic parts. Figure 1.2.4.1b shows an example where the losses in the ferromagnetic substrate of a coated conductor are the major loss components in a significant current interval.

The variation of the critical current density J_c inside the superconductor affects the AC losses. Owing to the pinning mechanisms in type-II superconductors, J_c depends on the local magnetic flux density and on its orientation, sometimes in a very complicated fashion. This local reduction of J_c can influence the shape of the

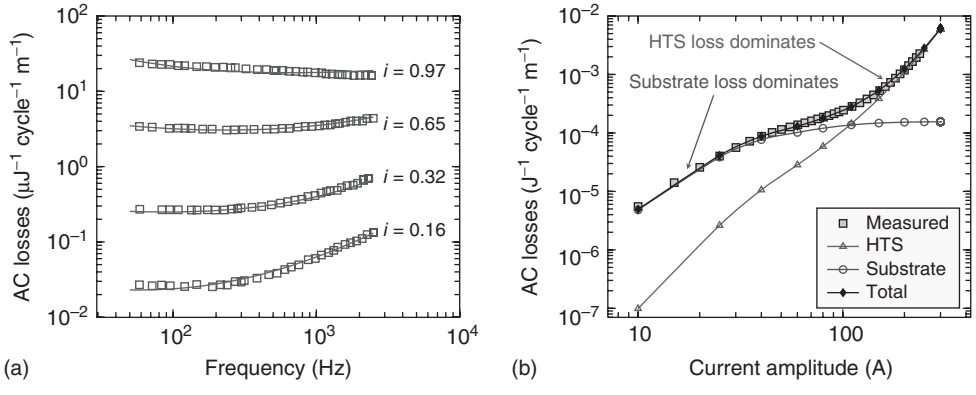

Figure 1.2.4.1 (a) Loss dissociation for a multifilamentary Bi-2223 tape: according to Eq. (1.2.4.1), the dissipated power is separated into resistive, hysteretic, and eddy current contributions with a least-square fitting of the form $p_2 f^2 + p_1 f + p_0$. Different current amplitudes $i = I_a/I_c$ are represented. (Reprinted from Ref. [2] Reproduced with permission of Ecole Polytechnique Fédérale de Lausanne.) (b) Transport losses of a yttriumbarium copper oxide (YBCO) coated conductor with ferromagnetic substrate: the losses in the substrate are the dominating components for currents <100 A. The different components are calculated by finite-element simulations.

AC loss characteristics of the whole tape, as do local nonuniformities of J_c caused by the manufacturing process.

1.2.4.3 **Measuring AC Losses**

This section describes the main methods used to measure AC losses in various circumstances (transport, magnetization, and their combination) and for different types of samples (short pieces of tape and large assemblies). Before proceeding, a brief comment on the terminology used here: in the following, *calorimetric* method indicates a method based on measuring the local increase of temperature caused by AC loss dissipation; this must be distinguished from the *boil-off* method (sometimes called *calorimetric* as well in the literature), which consists in measuring the amount of evaporated coolant.

1.2.4.3.1 **Transport Losses**

The goal is to measure the variation of magnetic flux caused by the AC transport current. The standard technique for measuring transport losses in straight tapes consists in soldering a pair of voltage taps on the tape, shaping them in the form of a loop, and measuring the voltage (see Figure 1.2.4.2a). It can be easily shown that, for the case of a sinusoidal transport current, only the voltage component in phase with the current generates dissipation [3]. The measurements are therefore developed to extract such component: this can be done, for example, by means of a lock-in amplifier. The voltage taps measure the sum of the voltage drop between the contact points and the voltage corresponding to the rate of variation of the magnetic flux in the loop. In practice, one is usually interested in measuring losses for currents smaller than the critical current I_c, and for such subcritical currents the voltage drop is zero. The question is therefore to determine what flux variation one measures.

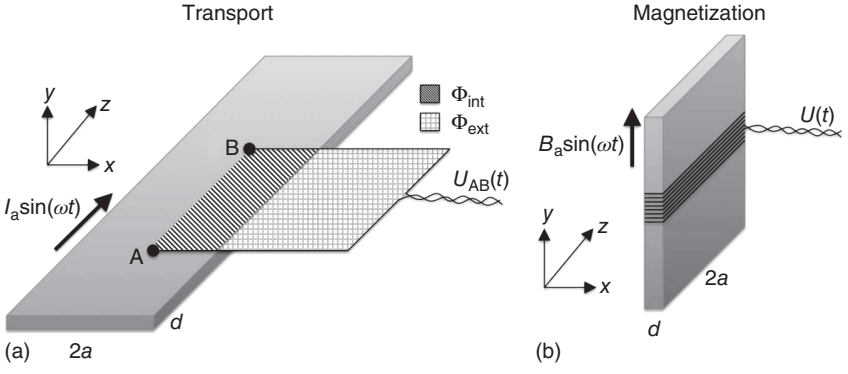

Figure 1.2.4.2 (a) Setup for measuring transport AC losses by electrical technique: for a tape with noncircular cross-section, the measuring loop needs to extend outside the tape. (b) Setup for measuring magnetization losses of a rectangular tape in parallel external field: in perpendicular field, the recorded loss value needs to be multiplied by a factor accounting for the demagnetizing effect.

In general, the voltage loop catches two types of fluxes, inside and outside the superconductor, which we can name Φ_{int} and Φ_{ext}, respectively (see Figure 1.2.4.2a). The ideal case is represented by a wire with circular cross-section because the flux lines are circular and concentric and do not cross the wire's surface: one could therefore think of placing the voltage loop on the surface of the wire, in this way catching all the relevant flux variations because the voltage associated with Φ_{ext} would be purely inductive (i.e., in quadrature with the transport current). Real tapes have elliptical or rectangular cross-section, and in those cases, things are more complicated because both Φ_{int} and Φ_{ext} have in-phase components. One must therefore extend the measuring loop outside the tape [4]. In principle, a loop extending far away from the sample would make sure that all the flux is caught; at the same time, however, a larger loop is also more prone to catch spurious signals and noise, which could affect the measured loss value. Clem calculated that a distance of three times the sample's half-width is a good compromise: the loop is sufficiently close to the sample and it provides loss values within 5–10% of the expected value [5]. More details on the influence of the position of the voltage taps and of the measured voltage signal on AC losses can be found in Refs. [6] and [7].

A completely different approach to measure transport AC losses is represented by the boil-off method, which consists in measuring the amount of coolant that evaporates as a consequence of the energy dissipation in the superconductor [8]. The main advantage is that it can be used with differently shaped and sized samples and it does not present the problem (typical of the electrical method) of recording the correct electric signal. This is particularly useful in the case of complex tape assemblies, such as cables and coils: tapes are closely packed together and soldering voltage taps and extracting the true loss signal can be quite problematic. The boil-off method is the standard measuring technique for low-temperature superconductors, especially for coils and cables. Its application to high-temperature superconductors cooled with liquid nitrogen is generally more difficult because of the very small volume of generated gas compared to the case of helium [9, 10].

1.2.4.3.2 Magnetization Losses

The standard technique for measuring the magnetization losses of a superconducting sample consists in placing the sample in a varying uniform magnetic field and measuring its magnetization by means of a pickup coil wound around the sample (see Figure 1.2.4.2b). The signal measured by the pickup coil is proportional to the energy dissipation in the sample. The ideal case is represented by an infinite slab in parallel field, where the field on the superconductor's surface is known and is equal to the applied field. A tape with rectangular cross-section with the field parallel to its longitudinal direction (as the one schematically shown in Figure 1.2.4.2b) is a good approximation of the slab configuration. In this case, the loss value is simply given by $Q = (\mu_0 N d 2a)^{-1} \int_0^{1/f} B_a(t) U(t) dt$, where N is the number of turns of the pickup coil, d and $2a$ are the thickness and width of the tape, respectively, and f is the frequency of the field. If the infinite slab

approximation is not valid, for example, in the case of magnetic field applied perpendicular to the tape's face, a calibration constant c taking into account the distortion of the field lines (which depends on the tape's shape and on the pickup coil's position) must be added in the expression for Q.

The calibration constant can be determined by a calorimetric method, and in general, it depends on field amplitude and frequency. A detailed description of the calibration process, including a discussion on the influence of the pickup coil position, can be found in [11].

In fact, the calorimetric method itself constitutes an alternative method for measuring the magnetization losses [12, 13] and it can be used for measuring the transport losses as well. It provides a direct measurement of the AC losses because it measures the dissipation in terms of temperature increase of the sample; compared to the electromagnetic method, it is not prone to electromagnetic disturbances, since the measured signal simply records a temperature increase; however, it requires a more complicated hardware setup (thermometers, insulations); in addition, the acquisition of data points is much slower, especially at liquid nitrogen temperatures, when one has to detect small temperature increases in a thermally noisy environment, which makes measurement repetition and data averaging necessary. As a rule of thumb, at the liquid nitrogen temperature, the calorimetric method is around 10 times slower than the electromagnetic method.

The calorimetric method can however be used to calibrate the AC loss values measured with the electromagnetic method, in particular to calculate the calibration factor c by which the measured signal needs to be multiplied in order to take into account the differences from the ideal case of a slab in parallel field. One does not need to wind the pickup coil literally around the sample, but can wind it on a fixed frame built to accommodate different samples with the same size. However, differently shaped or sized samples still require different pickup coils.

An alternative measuring approach that overcomes all the problems mentioned above is the so-called calibration-free method [14]. The method is based on the observation that the losses in the sample constitute a fraction of the power supplied to the whole system by the AC source; this fraction is generally small, but can be detected by building a symmetric system consisting of two pickup coils, subjected to the same external uniform magnetic field, connected in series, but wound in opposite directions (see Figure 1.2.4.3a,b). In the absence of a sample, the system is perfectly balanced and the measured voltage $U(t)$ is zero. When the sample is inserted inside one of the measuring coils, the symmetry is broken, the total voltage induced in the two coils by the external field cancels out because of their opposite winding directions, and the measured signal gives directly the loss of the sample, irrespective of its shape and dimensions. This method has the big advantage that the same experimental setup can be used to measure samples of different shapes and sizes, without the need of building *ad hoc* pickup coils. An alternative setup to measure the magnetization AC losses is presented in [15].

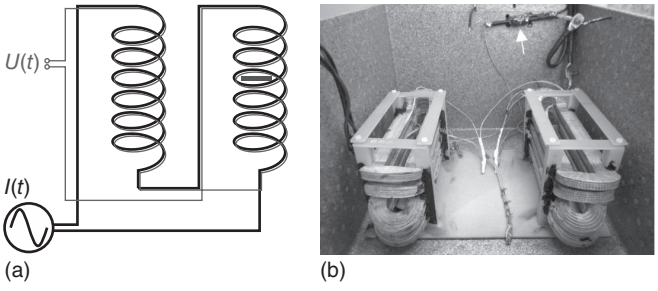

Figure 1.2.4.3 Conceptual design (a) and practical realization (b) of the calibration-free method. In the circuit, the rectangle represents the sample; in the picture, the arrow indicates the Rogowski coil used to extract the reference phase signal.

1.2.4.3.3 Combination of Transport and Magnetization AC Losses

In real applications, superconductors carry current while being also subjected to external magnetic fields, for example, produced by the adjacent turns in a coil. In this case, due to the complex interaction of the self-field and of the external field inside the superconductor, the AC losses are different from the simple sum of the losses occurring in the current-only and field-only cases.

Ashworth and Suenaga [16, 17] performed pioneering calorimetric measurements on Bi-2223 tapes. The calorimetric method, measuring the temperature increase associated with the AC losses, is not affected by the complex interaction of the electromagnetic fields. Its main limitation is the low speed of data acquisition and low accuracy for small currents and fields. Methods based on measuring the sample's magnetization by electromagnetic methods have also been developed [18, 19], even for the case when current and field are not in phase [20, 21].

1.2.4.4 Computing AC Losses

1.2.4.4.1 Analytical Computation

In the framework of the critical state model originally proposed by Bean [22], the loss density of a superconducting slab of width $2a$ in a parallel magnetic field of amplitude H_a can be easily calculated as [8][2]:

$$Q_M = \begin{cases} \frac{2}{3}\mu_0 H_a^2 \left(\frac{H_a}{H_p}\right) & H_a \le H_p \\ 2\mu_0 H_a^2 \left[\frac{H_p}{H_a} - \frac{2}{3}\left(\frac{H_p}{H_a}\right)^2\right] & H_a \ge H_p \end{cases} \quad (\mathrm{J\,cycle^{-1}\,m^{-3}}) \qquad (1.2.4.2)$$

where $H_p = J_c a$ is the field for which the slab is fully penetrated. The loss density increases rapidly (proportionally to H_a^3) for $H_a < H_p$ and more slowly (proportionally to H_a) for $H_a > H_p$. Norris [23] derived the formulas for the transport AC losses of superconductors with elliptical and infinitely thin cross-sections carrying

2) Here and in the following expressions for AC losses, *amplitude* is intended as the peak value of a sinusoidal oscillation; this explains the slight difference between formulas (1.2.4.2) and the formulas given in Ref. [8], which are written in terms of the peak-to-peak amplitude.

current $i = I/I_c$:

$$Q_T = \frac{I_c^2 \mu_0}{\pi} \begin{cases} (1-i)\ln(1-i) + (2-i)\frac{i}{2} & \text{ellipse} \\ (1-i)\ln(1-i) + (1+i)\ln(1+i) - i^2 & \text{thin strip} \end{cases} \quad (\mathrm{J\,cycle^{-1}\,m^{-1}}) \tag{1.2.4.3}$$

Formulas for magnetization losses of a thin strip of width $2a$ and *sheet* current density j_c in a field of amplitude H_a perpendicular to the strip's surface were independently derived by Brandt and Indenbom [24] and Zeldov *et al.* [25][3]:

$$Q_M = 4\mu_0 a^2 j_c H_a g\left(\frac{H_a}{H_c}\right) \quad (\mathrm{J\,cycle^{-1}\,m^{-1}}) \tag{1.2.4.4}$$

with $g(x) = (2/x)\ln\cosh x - \tanh x$ and $H_c = j_c/\pi$. The losses are proportional to the square of the width, which means that a practical way of reducing them is by making narrower conductors: a strip cut into N filaments has losses N times lower, provided that the filaments are electromagnetically uncoupled, for example, by means of twisting or transposition. In addition, similarly to the case of an infinite slab, the curve of the magnetization losses of a thin strip presents a change of slope: from $Q_M \sim H_a^4$ at low fields to $Q_M \sim H_a$ at high fields. A similar change of slope, related to the full penetration of the field in the superconductor, is observed in other geometries too.

Owing to their simplicity and applicability to conductor geometries found in practice, formulas (1.2.4.2)–(1.2.4.4) are very often used to estimate the losses of superconducting tapes and wires. Other analytical expressions have been derived for certain tape arrangements, like tape arrays and stacks. An exhaustive review of the analytical models for superconductors can be found in [26].

While useful for a quick estimation of AC losses, analytical models suffer from a number of limitations that affect their accuracy and applicability. For example, most analytical models are based on the critical state approach and as a consequence they cannot take into account the intrinsic frequency dependence of hysteresis losses nor current densities exceeding J_c, see for example, the expression of Eq. (1.2.4.3), which diverges for $I = I_c$. Also taking into account nonuniform fields and currents with arbitrary temporal evolution is a very difficult task to perform analytically. These and other limitations can be overcome by numerical methods, which can account for virtually any arbitrary geometry and excitation.

1.2.4.4.2 Numerical Computation

Many approaches exist for computing AC losses numerically, most of them summarized in the open-access review article [27]. We can divide them in two broad categories: *differential methods*, based on partial differential equations (PDEs), such as the finite-element method (FEM), and *integral methods*, based on the use of Green's function to transform the PDEs into integral equations. Each approach

3) Owing to the different utilized notation and approach, the expression for the losses has a different form in the two original papers, but they are in fact equivalent. Here, we utilize the one from [24].

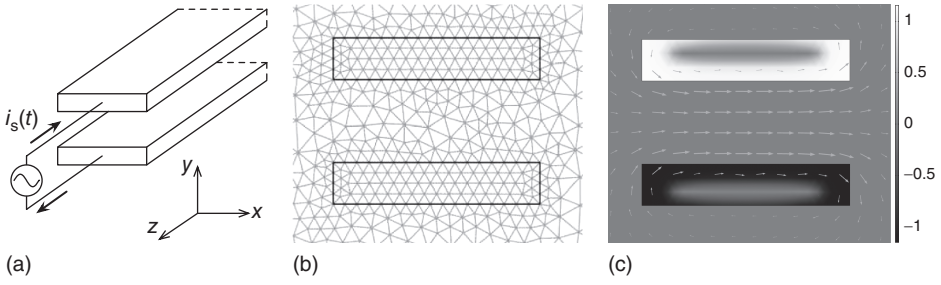

Figure 1.2.4.4 (a) Model of a two-conductor arrangement carrying antiparallel transport currents; (b) discretization in triangular mesh of a 2D cross-section of the geometric model; (c) plot of a typical solution (gray scale: J_z/J_c; arrows: H_x and H_y).

has advantages and drawbacks. In what follows, only the principles common to most numerical techniques are presented.

The first step for numerically computing AC losses consists in building a geometric model that represents the device under consideration, and then in discretizing it in a mesh of *elements* (i.e., domains of simple geometrical shape, typically triangles or quadrilaterals) that are compatible with the numerical method to be used (see, for example, Figure 1.2.4.4a,b). By using an integral method, the meshing of nonconducting regions can be avoided, although at the expense of a computational cost that grows approximately with the cube of the number of elements, as opposed to a roughly linear increase with differential methods [28].

Once geometry and mesh are created, one must choose a numerical method and a formulation, the latter being based on the variable one wants to solve for. There are many possible choices for electromagnetic variables: H, E, $A-V$, $T-\Omega$, J, and variants or combinations of these. Campbell reviewed many of the possible formulations in [29].

Regardless of the choice, the formulation must satisfy Maxwell's equations $\nabla \cdot B = 0$, $\nabla \times E = -\partial B/\partial t$, and $\nabla \times H = J$ (displacement current term $-\partial D/\partial t$ neglected), with the constitutive relationships $E = \overline{\rho}(J)J$ and $B = \overline{\mu}(H)H$, where $\overline{\rho}(J)$ and $\overline{\mu}(H)$ are, in the general case, nonlinear tensors, but very often they can be taken as scalars, especially in 2D problems where the H and J components are perpendicular.

Note that by neglecting the displacement current term, we obtain a diffusion-like equation, which is in principle simpler to solve than the classical "wave equation," characterized by the presence of a second-order time derivative. This approximation is well justified in most practical cases, especially near power frequencies. It also explains why we can ignore the $\nabla \cdot D$ Maxwell equation. However, the resulting diffusion problem is highly nonlinear because of the $\overline{\rho}(J)$ and $\overline{\mu}(H)$ terms. The former represents the nonlinearity of the superconductor (for which one usually takes $\mu = \mu_0$ even near H_{c_1}, which is usually lower than the fields of practical interest), and the latter generally accounts for the nonlinear behavior of ferromagnetic parts, ρ being generally taken as constant in this case.

In the simplified 2D case with J_z perpendicular to H_x and H_y (see Figure 1.2.4.4a for axis definition), one can use an empirical power-law model to describe the $E-J$ constitutive relationship near the critical current density, that is,

$$E = \rho(J)J = E_0\left(\frac{|J|}{J_c}\right)^n \text{sign}(J) \Rightarrow \rho = \frac{E_0}{J_c}\left(\frac{|J|}{J_c}\right)^{n-1} \tag{1.2.4.5}$$

where n is the power law exponent and J_c is the critical current density of the material. Both J_c and n depend in general on the local field B, the temperature T, and possibly also on the position. Whether to consider these model refinements depends on the operating conditions of the considered problem. In addition, other $E-J$ constitutive equations can be used.

Once the problem is fully defined, it has to be discretized according to the chosen numerical method. In all cases, this operation results in a generally large system of equations to be solved numerically. The numerical solution obtained is a piecewise approximation of the continuous problem, and this approximation converges toward the exact solution as the discretization is refined. Figure 1.2.4.4c shows an example of a solution obtained with the FEM.

The numerical solution of the problem is not straightforward though. Since the problem is systematically nonlinear, static or time harmonic solutions are not possible, and a time transient simulation must be performed, which is usually delicate and may result in divergence of the solver if the time-stepping algorithm is not robust enough. An adaptive time solver able to handle differential algebraic equation systems is typically preferred over simple basic methods, although it is possible to succeed with any methods if one is willing to use small time steps and thus wait long times. One can avoid these problems by using methods based on the critical state model instead of the smooth current–voltage characteristics shown in Eq. (1.2.4.5) [30, 31]; these methods are computationally faster and can be preferable when flux creep is not a concern.

The final step for numerically computing AC losses simply consists in performing post-processing operations on the obtained numerical solution. The fundamental quantity to retrieve is J (see Figure 1.2.4.4c for instance), from which one can compute the electric field E and the local power density $p(t) = \int_\Omega E \cdot J \; d\Omega$, where Ω is the cross-section (2D) or volume (3D) of the superconducting domain in which one wants to compute AC losses. For example, in a 2D case like that illustrated in Figure 1.2.4.4, one has $J = J_z(x, y, t)$, and using Eq. (1.2.4.5) to express E in terms of J, one obtains:

$$Q = \int_{t_0}^{t_0+T_p} dt \int_\Omega \rho(J)J^2 d\Omega \quad (\text{J cycle}^{-1}) \tag{1.2.4.6}$$

where T_p is the period of the AC signal ($T_p = 1/f$), and t_0 is an initial time for starting the integration, chosen in a region where the $\rho(J)J^2$ waveform has reached a steady state. Additional post-processing computations might be required if J_c or n is a function of B or any other parameter.

Expression (1.2.4.6) is very general and includes all losses in the domain Ω. However, other approaches are possible for computing the AC losses, namely using

global quantities such as the current and voltage in each conductor, or using magnetic quantities (see Ref. [27] for details).

References

1. Stavrev, S., Dutoit, B., Nibbio, N., and Le Lay, L. (1998) Eddy current self-field loss in Bi-2223 tapes with a.c. transport current. *Physica C*, **307**, 105–116.
2. Stavrev, S. (2002) Modelling of high temperature superconductors for ac power applications. PhD thesis. Ecole Polytechnique Fédérale de Lausanne.
3. Rabbers, J.J. (2001) AC loss in superconducting tapes and coils. PhD thesis, University of Twente.
4. Campbell, A.M. (1995) AC losses in high Tc superconductors. *IEEE Trans. Appl. Supercond.*, **5** (2), 682–687.
5. Clem, J.R., Benkraouda, M., and McDonald, J. (1996) Penetration of magnetic flux and electrical current density into superconducting strips and disks. *Chin. J. Phys.*, **34** (2-11), 284–290.
6. Yang, Y., Hughes, T., Beduz, C., Spiller, D., Scurlock, R., and Norris, W. (1996) The influence of geometry on self-field AC losses of Ag sheathed PbBi2223 tapes. *Physica C*, **256**, 378–386.
7. Klinčok, B., Gömöry, F., and Pardo, E. (2005) The voltage signal on a superconducting wire in AC transport. *Supercond. Sci. Technol.*, **18**, 694–700.
8. Wilson, M.N. (1983) *Superconducting Magnets*, Clarendon Press, Oxford.
9. Okamoto, H., Sumiyoshi, F., Miyoshi, K., and Suzuki, Y. (2006) The nitrogen boil-off method for measuring AC losses in HTS coils. *IEEE Trans. Appl. Supercond.*, **16** (2), 105–108.
10. Murphy, J.P., Mullins, M.J., Barnes, P.N., Haugan, T.J., Levin, G.A., Majoros, M., Sumption, M.D., Collings, E.W., Polak, M., and Mozola, P. (2013) Experiment setup for calorimetric measurements of losses in HTS coils due to AC current and external magnetic fields. *IEEE Trans. Appl. Supercond.*, **23** (3), 4701505.
11. Schmidt, C. (2008) Ac-loss measurement of coated conductors: the influence of the pick-up coil position. *Physica C*, **468** (13), 978–984.
12. Schmidt, C. (2000) Calorimetric ac-loss measurement of high *Tc*-tapes at 77 K, a new measuring technique. *Cryogenics*, **40**, 137–143.
13. Ashworth, S. and Suenaga, M. (2001) Local calorimetry to measure ac losses in HTS conductors. *Cryogenics*, **41** (2), 77–89.
14. Šouc, J., Gömöry, F., and Vojenčiak, M. (2005) Calibration free method for measurement of the AC magnetization loss. *Supercond. Sci. Technol.*, **18**, 592–595.
15. Grilli, F., Ashworth, S.P., and Stavrev, S. (2006) AC loss characteristics of stacks of YBCO coated conductors. *Mater. Res. Soc. Symp. Proc.*, **946**, 0946-HH10-06.
16. Ashworth, S.P. and Suenaga, M. (1999) Measurement of ac losses in superconductors due to ac transport currents in applied ac magnetic fields. *Physica C*, **313**, 175–187.
17. Ashworth, S.P. and Suenaga, M. (1999) The calorimetric measurement of losses in HTS tapes due to ac magnetic fields and transport currents. *Physica C*, **315**, 79–84.
18. Rabbers, J., ten Haken, B., Gömöry, F., and ten Kate, H.H.J. (1998) Self-field loss of BSCCO/Ag tape in external AC magnetic field. *Physica C*, **300**, 1–5.
19. Jiang, Z. and Amemiya, N. (2004) An experimental method for total AC loss measurement of high Tc superconductors. *Supercond. Sci. Technol.*, **17** (3), 371–379.
20. Nguyen, D.N., Sastry, P., Zhang, G.M., Knoll, D.C., and Schwartz, J. (2005) AC loss measurement with a phase difference between current and applied magnetic field. *IEEE Trans. Appl. Supercond.*, **15** (2), 2831–2834.
21. Vojenčiak, M., Šouc, J., Ceballos, J., Gömöry, F., Pardo, E., and Grilli, F. (2006) Losses in Bi-2223/Ag tape at simultaneous action of AC transport and AC magnetic field shifted in phase. *J. Phys.: Conf. Ser.*, **43**, 63–66.

22. Bean, C.P. (1962) Magnetization of hard superconductors. *Phys. Rev. Lett.*, **8** (6), 250–252.
23. Norris, W. (1970) Calculation of hysteresis losses in hard superconductors carrying ac: isolated conductors and edges of thin sheets. *J. Phys. D Appl. Phys.*, **3**, 489–507.
24. Brandt, E.H. and Indenbom, M. (1993) Type-II-superconductor strip with current in a perpendicular magnetic field. *Phys. Rev. B*, **48** (17), 12893–12906.
25. Zeldov, E., Clem, J., McElfresh, M., and Darwin, M. (1994) Magnetization and transport currents in thin superconducting films. *Phys. Rev. B*, **49** (14), 9802–9822.
26. Mikitik, G., Mawatari, Y., Wan, A., and Sirois, F. (2013) Analytical methods and formulas for modeling high temperature superconductors. *IEEE Trans. Appl. Supercond.*, **23** (2), 8001920.
27. Grilli, F., Pardo, E., Stenvall, A., Nguyen, D.N., Yuan, W., and Gömöry, F. (2013) Computation of losses in HTS under the action of varying magnetic fields and currents. *IEEE Trans. Appl. Supercond.*, **20**, 1379–1382.
28. Sirois, F., Roy, F., and Dutoit, B. (2009) Assessment of the computational performances of the semi-analytical method (SAM) for computing 2-D current distributions in superconductors. *IEEE Trans. Appl. Supercond.*, **19** (3), 3600–3604.
29. Campbell, A.M. (2011) An introduction to numerical methods in superconductors. *J. Supercond. Novel Magn.*, **24**, 27–33.
30. Pardo, E., Gömöry, F., Šouc, J., and Ceballos, J.M. (2007) Current distribution and ac loss for a superconducting rectangular strip with in-phase alternating current and applied field. *Supercond. Sci. Technol.*, **20** (4), 351–364.
31. Campbell, A.M. (2007) A new method of determining the critical state in superconductors. *Supercond. Sci. Technol.*, **20**, 292–295.